

1

[ATLAS Semivisible Jets]

2

[Elena Laura Busch]

3

Submitted in partial fulfillment of the  
requirements for the degree of  
Doctor of Philosophy  
under the Executive Committee  
of the Graduate School of Arts and Sciences

4

5

6

7

8

COLUMBIA UNIVERSITY

9

2024

10

© 2024

11

[Elena Laura Busch]

12

All Rights Reserved

13

## **Abstract**

14

[ATLAS Semivisible Jets]

15

[Elena Laura Busch]

16

Abstract of dissertation (place-holder).

## Table of Contents

18	Acknowledgments . . . . .	xvi
19	Dedication . . . . .	xvii
20	Introduction or Preface . . . . .	1
21	<b>I Theory</b>	<b>2</b>
22	Chapter 1: The Standard Model . . . . .	3
23	1.1 Phenomenology: Particles and Forces . . . . .	3
24	1.1.1 Particles . . . . .	3
25	1.1.2 Forces . . . . .	5
26	1.2 QCD and Jets . . . . .	7
27	1.3 Symmetries . . . . .	8
28	1.3.1 Spontaneous Symmetry Breaking and The Higgs Mechanism . . . . .	9
29	1.4 Experimental Validation of the Standard Model . . . . .	10
30	1.5 Limitations of the Standard Model . . . . .	11
31	Chapter 2: Physics Beyond the Standard Model . . . . .	13
32	2.1 Hidden Valley Models . . . . .	13
33	2.2 Dark QCD . . . . .	14

34	2.3 Semi-visible Jets . . . . .	15
35	<b>II Experiment</b>	<b>17</b>
36	Chapter 3: The Large Hadron Collider . . . . .	18
37	3.1 Accelerator Physics . . . . .	19
38	3.1.1 The Journey of a Proton . . . . .	19
39	3.1.2 Magnets . . . . .	20
40	3.2 Luminosity . . . . .	21
41	3.3 LHC Timeline . . . . .	24
42	Chapter 4: The ATLAS Detector . . . . .	26
43	4.1 Coordinate System and Geometry . . . . .	27
44	4.2 Inner Detector . . . . .	28
45	4.2.1 Pixel Detector . . . . .	29
46	4.2.2 Semiconductor Tracker . . . . .	31
47	4.2.3 Transition Radiation Tracker . . . . .	31
48	4.3 Calorimeters . . . . .	31
49	4.3.1 Liquid Argon Calorimeter . . . . .	32
50	4.3.2 Tile Calorimeter . . . . .	35
51	4.4 Muon Spectrometer . . . . .	36
52	4.5 Magnet System . . . . .	38
53	4.6 Forward Detectors . . . . .	39
54	4.7 Trigger and Data Acquisition . . . . .	40

55	Chapter 5: Particle Reconstruction and Identification . . . . .	44
56	5.1 Inner Detector Tracks . . . . .	44
57	5.2 Photons and Electrons . . . . .	46
58	5.3 Muons . . . . .	48
59	5.4 Jets . . . . .	50
60	5.4.1 Calorimeter Clusters . . . . .	51
61	5.4.2 Particle Flow Algorithm . . . . .	52
62	5.4.3 Jet Clustering . . . . .	53
63	5.4.4 Ghost Track Association . . . . .	56
64	5.5 Missing Transverse Energy . . . . .	57
65	<b>III Search</b>	<b>59</b>
66	Chapter 6: Monte Carlo and Data . . . . .	60
67	6.1 Data . . . . .	60
68	6.2 Simulation . . . . .	62
69	6.2.1 Simulated Backgrounds . . . . .	62
70	6.2.2 Signal Simulation . . . . .	63
71	Chapter 7: Machine Learning Tools . . . . .	66
72	7.1 Introduction . . . . .	66
73	7.1.1 Machine Learning Fundamentals . . . . .	67
74	7.2 Particle Flow Network (Supervised) . . . . .	70
75	7.2.1 Architecture Fundamentals . . . . .	70
76	7.2.2 Input Modeling, Scaling, and Rotation . . . . .	71

77	7.2.3 Training . . . . .	80
78	7.2.4 Performance . . . . .	81
79	7.3 ANTELOPE (Semi-supervised) . . . . .	85
80	7.3.1 Architecture Fundamentals . . . . .	85
81	7.3.2 Training . . . . .	88
82	7.3.3 Performance . . . . .	89
83	Chapter 8: Analysis Strategy . . . . .	92
84	8.1 Preselection . . . . .	92
85	8.2 SVJ Fit and Discovery Analysis Strategies . . . . .	94
86	8.3 Analysis Regions . . . . .	98
87	8.3.1 Control and Validation Regions . . . . .	98
88	8.3.2 Signal Region . . . . .	100
89	8.4 Background Estimation . . . . .	102
90	8.5 Fit Strategy and Validation . . . . .	103
91	8.5.1 SVJ Fit Strategy . . . . .	103
92	8.5.2 Discovery Strategy . . . . .	111
93	Chapter 9: Results . . . . .	117
94	9.1 SVJ Fit Result . . . . .	117
95	9.1.1 Systematics . . . . .	118
96	9.1.2 Interpretation . . . . .	123
97	9.2 Discovery Result . . . . .	123

98	Conclusion or Epilogue . . . . .	126
99	References . . . . .	130
100	Appendix A: Trigger Studies . . . . .	138
101	Appendix B: Machine Learning Approaches . . . . .	142
102	B.1 Unsupervised: AE vs. ANTELOPE . . . . .	142
103	B.1.1 Signal Contamination . . . . .	143
104	B.2 PFN Optimality Checks . . . . .	143
105	B.3 Single Jet vs Jet System ML Approach . . . . .	144
106	B.4 PFN Training Composition . . . . .	146
107	B.5 $E_T^{\text{miss}}$ and $E_T^{\text{miss}}\phi$ Shapes . . . . .	148
108	B.5.1 NCB Preselection . . . . .	148
109	B.5.2 TileCal Correction . . . . .	150
110	Appendix C: Truth Studies . . . . .	153
111	C.1 Jet dR Matching . . . . .	153
112	Appendix D: BumpHunter . . . . .	155
113	D.1 Signal Mass Resolution $m_T$ Binning . . . . .	155

## List of Figures

115	1.1	Diagram of the 17 particles comprising the Standard Model . . . . .	4
116	1.2	Fundamental particle interactions of the three fundamental forces described by the	
117		Standard Model [2]. . . . .	6
118	1.3	An example Feynmann diagram of jet production . . . . .	7
119	1.4	An illustration of the “hat shaped” potential of the Higgs field, resulting in a non-	
120		zero vacuum expectation value. . . . .	9
121	2.1	Illustration of the hidden valley potential. . . . .	14
122	2.2	The massive mediator particle $Z'$ of the s-channel realization of a HV model . . .	14
123	3.1	The LHC accelerator complex at CERN [29] . . . . .	20
124	3.2	The octants of the LHC and location of various beam activities [28]. Stars indicate	
125		the locations of beam collisions, and the associated detectors recording the	
126		outcome of those collisions. . . . .	21
127	3.3	(Left) Total integrated luminosity over the course of Run 2. (Right) Average num-	
128		ber of $pp$ interactions per bunch crossing in Run 2. Each curve is weighted by the	
129		integrated luminosity for the year. . . . .	23
130	3.4	Timeline of LHC and HL-LHC activities [31]. Integrated luminosity estimates are	
131		approximate, and not reflective of the exact amount delivered to each experiment. .	25
132	4.1	The ATLAS detector [34]. . . . .	26
133	4.2	ATLAS coordinate system and geometry . . . . .	29
134	4.3	A 3D visualization of the structure of the ID in the barrel region [35] . . . . .	30

135	4.4 A 3D visualization of the structure of the ID end-caps [34]. The paths of two charged particles ( $\eta = 1.4$ and 2.2) are illustrated. . . . .	30
136		
137	4.5 ATLAS calorimetry system [36] . . . . .	32
138		
139	4.6 Diagram of a segment of the EMB, demonstrating the accordion plate arrangement and the cell segmentation pattern [37]. Three layers are illustrated, and the variation in the cell granularity between the front layer (Sampling Layer 1) and the back layer (Sampling Layer 3) is shown. . . . .	33
140		
141		
142	4.7 A LAr pulse as produced in the detector (triangle) and after shaping (curve) [37] . .	34
143		
144	4.8 Readout gap structure in HEC [37] . . . . .	35
145		
146	4.9 TileCal wedge module [40] . . . . .	36
147		
148	4.10 Cross section view of the muon spectrometer system [41] . . . . .	37
149		
150	4.11 Layout of the barrel and end-cap toroid magnets [34] . . . . .	39
151		
152	4.12 Block diagram of the L1 trigger process [34]. The overall L1 trigger decision is made by the CTP. . . . .	41
153		
154		
155		
156		
157	4.13 Block diagram of the trigger and data acquisition processes, including L1 and HLT processes [45]. . . . .	42
158		
159	5.1 This graphic illustrates a slice of ATLAS detector barrel [46]. A photon, electron, and two jets (associated to the proton and neutron) are shown, illustrating each object's interaction with various ATLAS subsystems. The path of the charged particles is curved on account of the strong magnetic field produced by the solenoid and toroid magnets. A neutrino, generally representing the reconstruction of missing transverse energy, is also illustrated. . . . .	45
160		
161		
162		
163	5.2 Track reconstruction seeding, finding and fitting illustration [47] . . . . .	46
164		
165	5.3 Three types of EM object candidates [49]. . . . .	47
166		
167	5.4 The four types of muon track candidates [51]. The red bands indicate where detector measurements for each muon track candidate are made. The dashed lines indicate the path of the muon through detectors where no measurement is made. Standalone muon is another term for an extrapolated muon. . . . .	50
168		
169	5.5 The fragmentation and hadronization processes undergone by a quark produced in a proton-proton collision [53]. . . . .	51
170		

165	5.6 A flow chart illustrating the particle flow algorithm progression [56]. The solid	54
166	lines indicate the progression of tracks through the algorithm, while the dotted	
167	lines indicate the progression of clusters. The process begins with track selection	
168	and continues until the energy associated with the tracks has been removed from	
169	the calorimeter. At the end charged particle tracks, unmodified topo-clusters, and	
170	the remnants of topo-clusters which have had part of their energy removed remain.	
171	5.7 A comparison of jet clustering with four different jet algorithms. The anti- $k_t$ al-	55
172	gorithm is observed to create the most conical jets, where the shape of the jet is	
173	immune to the presence of soft radiation [57]. . . . .	
174	5.8 A comparison of MC simulation and data for $Z \rightarrow \mu\mu$ events where real $E_T^{\text{miss}} =$	58
175	0 [65]. The resolution of the missing energy in the transverse ( $x - y$ ) plane is	
176	observed to increase with increasing total $\sum E_T$ . . . . .	
177	6.1 Integrated luminosity for the ATLAS experiment as a function of time during Run	61
178	2 [66] . . . . .	
179	6.2 The transverse momentum slices of the QCD MC simulation, overlayed to show	63
180	how they come together to create a smooth distribution (left) once weighted prop-	
181	erely. The original unweighted distribution is shown on the right, illustrating the	
182	enhanced statistics for the high $p_T$ range. . . . .	
183	6.3 Background processes relevant to the SVJ signal. . . . .	64
184	7.1 A diagram of a deep neural network architecture [76]. . . . .	67
185	7.2 An example score distribution for a binary classifier. A higher score indicates a	68
186	greater probability of being signal. Most signal events (orange) receive a high	
187	score while most background events (blue) receive a low score, indicating good	
188	classification. . . . .	
189	7.3 Several example ROC curves. The AUC is also illustrated [77]. . . . .	69
190	7.4 A diagram of auto-encoder architecture. The loss is computed as a difference (often	70
191	the <i>mean squared error</i> or MSE) between the input $x$ and the output $y$ [79]. . . . .	
192	7.5 The Energy/Particle Flow Network concept, from Ref. [80]. The physics input in-	72
193	formation is represented as arrows on the left, for an arbitrary number of particles.	
194	The $\Phi$ transformation converts these arrows to 3 graphs, indicating the $\Phi$ basis	
195	dimension $l$ is 3 in this example. The graphs are then summed for all particles to	
196	create $O$ , or the event representation. . . . .	

197	7.6 An annotated diagram of the PFN architecture. $y$ and $\phi$ represent geometric information for the input particles, $z$ represents energy information, and PID encompasses any other particle ID information in the input. PID is presented in the diagram as a 1-dimensional input, but could represent multiple input dimensions. . . . .	73
201	7.7 An illustration of the expected dijet behavior of semi-visible jets, where one jet is closely aligned with $E_T^{\text{miss}}(\text{MET})$ . In the figure two jet cones $j_1$ and $j_2$ are illustrated, along with their associated momentum vectors $\vec{p}_1$ and $\vec{p}_2$ . . . . .	73
204	7.8 Illustration of track coordinates $d_0$ and $z_0$ . . . . .	74
205	7.9 Distributions of the track multiplicity in the leading and subleading jets, comparing signal and background PFN training samples. . . . .	74
207	7.10 A diagram demonstrating how the two jet system is rotated in $(\eta, \phi)$ . The jet cones and associated jet tracks are illustrated. The dashed tracks represent dark hadrons while the solid tracks represent SM hadrons. The system average $(\bar{\eta}, \bar{\phi})$ is shown in red and an example track with coordinates $(\eta_i, \phi_i)$ is shown in purple. . . . .	75
211	7.11 The 6 PFN track variables in background MC (blue) and signal MC (orange) before scaling and rotation. The track kinematics are largely similar, and the variation in the $\phi$ distribution is explained in the text. . . . .	77
214	7.12 The 6 PFN track variables in background MC (blue) and signal MC (orange) after scaling and rotation. The $\phi$ distribution is modified by the rotation procedure, as explained in the text. . . . .	78
217	7.13 The 6 PFN track variables in background MC (blue) and data (orange), after the scaling and rotation procedure is applied. There is excellent modeling of the data by the MC within the track variables. The slight discrepancy in the $\phi$ distribution due to the inaccuracies of modeling dead TileCal cells in the QCD MC is considered. The level of discrepancy is determined to be within tolerance given that the final result will be data driven and the QCD model is used in the PFN training only. . . . .	79
223	7.14 PFN score for full-background MC (black), data (red), and 2 representative signal points (green). The left plot is from a QCD-only training, while the right plot is from a full-background training. The histograms have been normalized to visualize the shapes better - the actual number of plotted events is shown in the legend. In the left plot we observe that both signal points are strongly classified as signal-like. In the right plot we observe less background contamination in the high score region, but worse signal classification. Both PFN trainings were tested for their effect on the analysis sensitivity and the QCD-only training was found to be favorable. . . . .	81

231	7.15 PFN architecture loss during training as a function of epoch (left) and the evaluated score for signal and background training samples (right). The loss vs. epoch plot shows that the network is not overtrained. The score plot shows a good separation between signal and background. . . . .	82
232		
233		
234		
235	7.16 ROC for the PFN, using SVJ signal events (true positive) and data (false positive). . . . .	83
236		
237	7.17 AUC for the PFN, shown for each signal in the SVJ grid. . . . .	83
238		
239		
240		
241	7.18 Illustration of the PFN score selection, showing the separation between data (black) and 4 signal points (blue and green). The legend information takes the form “ $m_Z'$ $R_{inv}$ ” for the signal. The PFN score selection value is shown by the pink line. Only events with a score $> 0.6$ will be accepted for use in the analysis. We see that most background (data) is rejected, while most signal is accepted. . . . .	84
242		
243		
244		
245	7.19 An annotated diagram of the ANTELOPE architecture. Step 1 illustrates the PFN which is fully trained before its use in the ANTELOPE network. Step 2 illustrates the variational auto-encoder. The Gaussian sampling of the latent space is shown, illustrating how the VAE differs from the AE shown in Figure 7.4. . . . .	86
246		
247		
248		
249		
250		
251	7.20 A visual representation of the 64 PFN $O$ which create the input for the VAE component of ANTELOPE. The plot is 2D histogram of the PFN $O$ index (0-63) versus the value assumed by that index. Many entries have a $O$ value of exactly 0.0. To visually separate these from entries with a small but non-zero $O$ value, any entries with value = 0.0 are moved to value = -0.01 (leftmost column) for the purpose of the plot only. . . . .	87
252		
253	7.21 ANTELOPE architecture loss during training as a function of epoch. . . . .	88
254		
255		
256		
257	7.22 Anomaly score distribution (left), comparing all data (orange) and all SVJ signals (blue). The signals have a small but consistently higher score than the data, indicating that they are tagged as more anomalous by ANTELOPE. A ROC curve for an example signal point is also shown (right). . . . .	89
258		
259		
260		
261		
262	7.23 AUC from the ANTELOPE score for each signal in the SVJ grid. . . . .	90
263		
264		
265		
266	7.24 Comparing data and the alternate signal models for the PFN score (left) and ANTELOPE score (right). The emerging jet signal (dark blue) and gluino R-hadron signals (red, light green) are an example of the advantage of the model-independent ANTELOPE approach. These signals have a bimodal shape in PFN score but are clearly tagged with a high anomaly score by the ANTELOPE. . . . .	91
267		

263	8.1 Energy and momentum analysis variables at preselection, for data, all background 264 MC and representative signal models. $m_T$ is the key fit variable, and this plot 265 illustrates the smoothly falling background in comparison to the resonant shape of 266 the signals. $m_T$ is further illustrated in Figure 8.8. . . . .	95
267	8.2 Orientation analysis variables at preselection, for data, all background MC and 268 representative signal models. While $\Delta\phi(E_T^{\text{miss}}, j)$ variables are not used explicitly 269 in the analysis flow, they help create a picture of the event. . . . .	96
270	8.3 Flow of analysis selections, regions, and background estimation/validation fitting 271 strategy. TODO: diagram needs to be corrected . . . . .	97
272	8.4 Distributions of the subleading jet width $\text{width}_{j2}$ (left) and leading jet with $\text{width}_{j1}$ 273 (right) in data, background MC and signals at preselection. All SVJ signals are 274 seen to be wider than the background in $\text{width}_{j2}$ . The same is not true for $\text{width}_{j1}$ , 275 where some signals are observed to closely match the background. . . . .	98
276	8.5 2D plots revealing correlations between $\text{width}_{j2}$ and $m_T$ (left), $\text{width}_{j2}$ and ML 277 score (middle), and $m_T$ with ML score (right). For the top row, the ML score is 278 the PFN score, and for the bottom three, the ML score is the ANTELOPE score. 279 Minimal correlations are observed and are shown to not sculpt $m_T$ , validating these 280 variables for analysis region construction and statistical treatment. . . . .	99
281	8.6 $m_T$ in simulation across the CR, VR, and SR for both PFN (left) and ANTELOPE 282 (right) selections. . . . .	100
283	8.7 Definition of CR, VR, and SR regions using $\text{width}_{j2}$ and the ML score, along with 284 the population of each region in data statistics. The SVJ Fit region is shown on top 285 with the PFN score on the x-axis, and Discovery region is shown on the bottom, 286 with the ANTELOPE score on the x-axis. . . . .	101
287	8.8 The resonant shape of the SVJ signals in $m_T$ , in contrast to the smoothly falling 288 $m_T$ background. The high $R_{\text{inv}}$ signals (right) boast a wider shape, making them 289 more difficult to detect, while the low $R_{\text{inv}}$ signals(left) produce a more narrow 290 resonance in $m_T$ . . . . .	102
291	8.9 Background-only $m_T$ fits using representative MC in the CR (left), VR (middle), 292 and SR (right). . . . .	104
293	8.10 Background-only $m_T$ fits using data in the full statistics CR and VR regions. . . . .	105
294	8.11 $m_T$ distribution in the data CR, before (left) and after (right) smoothing. . . . .	106
295	8.12 Background-only $m_T$ fits using pseudo-data from the CR template. . . . .	107

296	8.13 $p$ -value histograms from 100 fits to Asimov data in the CR. . . . .	107
297	8.14 Example S+B fit on a background $m_T$ spectrum with injected signal from the point (4000 GeV, $R_{inv}=0.2$ ). . . . .	108
299	8.15 Measured signal at a variety of injected values (1x, 2x, and $5x\sqrt{b}$ ), for all signal points in the grid, $R_{inv}=0.2$ (top left), 0.4 (top right), 0.6 (bottom left), and 0.8 (bottom right). . . . .	109
302	8.16 95% C.L. upper limits for signal models across $Z'$ mass, for four different $R_{inv}$ frac- tions, from the CR region (without systematics). TODO - ATLAS style . . . . .	110
304	8.17 95% C.L. upper limits and observed limit for signal models across $Z'$ mass, with varying amounts of signal injected. TODO - ATLAS style . . . . .	111
306	8.18 Post-fit function and residuals for the ANTELOPE CR and VR. . . . .	112
307	8.19 BumpHunter fits on the ANTELOPE $m_T$ spectra for both the CR (left) and VR (right). In a signal-depleted region, good agreement with the background estima- tion is observed. . . . .	113
310	8.20 BumpHunter p-values extracted for 100 Asimov toys for both the ANTELOPE CR (left) and VR (right). . . . .	114
312	8.21 Example injected gaussian signal. . . . .	114
313	8.22 Response of the BumpHunter framework to signal injection of $5\sigma$ significance to the model-dependent polynomial fit framework. The local significance (top) and bump location (bottom) are shown. . . . .	116
316	8.23 Example BH response to gaussian signal injection at 4000 GeV with width of 10%. . . . .	116
317	9.1 $m_T$ in the unblinded SVJ Fit SR with a background-only fit ( $p$ -value = 0.265). . . . .	117
318	9.2 Example spurious signal fits, indicating a Gaussian distribution around the mean of spurious signal events. . . . .	119
320	9.3 Spurious signal as a function of resonance mass. The requirement $\mu/\sigma < 0.5$ is satisfied for all signal points, where $\mu$ is the mean number of spurious signal events and $\sigma$ is the standard deviation of the number of spurious signal events from 100 pseudo-data experiments. . . . .	119

324	9.4	$m_T$ of the 3500 GeV $Z'$ , $R_{inv} = 0.2$ signal point, shown with an example JES 325 variation. The nominal shape (“Nom”), $1\sigma$ up (“Up”), and $1\sigma$ down (“down”) 326 variations are shown. The variation is seen to have a negligible impact on the 327 signal shape. . . . .	121
328	9.5	$m_T$ of the 3500 GeV $Z'$ , $R_{inv} = 0.2$ signal point, shown with the sum in quadrature 329 of all JES and JER variations. The nominal shape (“Nom”), $1\sigma$ up (“Up”), and $1\sigma$ 330 down (“down”) variations are shown. . . . .	122
331	9.6	Signal distribution of $m_T$ , varying the ISR, FSR and MPI configuration. . . . .	122
332	9.7	Expected and observed 95% CL limits in the unblinded SR, as a function of $Z'$ 333 masses for $R_{inv}=0.2$ (top left), 0.4 (top right), 0.6 (bottom left), 0.8 (bottom right); 334 no systematics. . . . .	124
335	9.8	$m_T$ in the unblinded ANTELOPE SR with a background-only fit (p-value = 0.74), 336 left. BumpHunter test selecting the most significant data excess with a p-value of 337 0.8098, right. . . . .	125
338	A.1	Trigger yield and efficiency for both the MET trigger and small-R jet trigger ap- 339 proach. Each entry represent a signal point, labelled by the $Z'$ mass and the 340 $R_{inv}$ fraction. . . . .	138
341	A.2	The factor of improvement in $S/\sqrt{B}$ for each trigger method compared to the un- 342 triggered case. . . . .	139
343	A.3	The ratio of $S/\sqrt{B}$ of jet trigger over $E_T^{\text{miss}}$ trigger selection. . . . .	139
344	A.4	Analysis variables where high $R_{inv}$ signals a clearly distinct from background and 345 low $R_{inv}$ variables. On the contrary, leading jet $p_T$ is one of the only variables 346 where low $R_{inv}$ signals are distinct from background. . . . .	141
347	A.5	OR of jet and $E_T^{\text{miss}}$ triggers. . . . .	141
348	B.1	. . . . .	142
349	B.2	. . . . .	143
350	B.3	Comparison of PFN AUC (top) and sensitivity in the $m_T$ mass window (bottom) 351 for a single PFN model (left) vs. two models trained on $R_{inv} < 0.5$ and $> 0.5$ 352 separately (right). . . . .	144
353	B.4	Scans done to check for optimality of PFN training parameters. . . . .	145

354	B.5 $\phi$ Performance comparison between single jet and jet system ML approach . . . . .	146
355	B.6 $\phi$ Comparison in the AUC score across the grid for the mixed background strategy	
356	vs the QCD only strategy. The bottom table highlights that the QCD only strategy	
357	gives superior sensitivity across the signal grid. . . . .	147
358	B.7 $E_T^{\text{miss}}$ in data before and after Tight event cleaning is applied. . . . .	148
359	B.8 $E_T^{\text{miss}}$ vs jet1 $p_T$ in data before and after Tight event cleaning is applied. . . . .	149
360	B.9 $\eta$ vs $\phi$ for leading and subleading jets, before and after the application of tight	
361	cleaning. . . . .	149
362	B.10 Added NCB preselection and impact on $E_T^{\text{miss}}$ shape. . . . .	150
363	B.11 NCB preselection impact on data and signal yields. . . . .	151
364	B.12 Impact of tight cleaning and non-collision background preselection. . . . .	152
365	B.13 $E_T^{\text{miss}}\phi$ in data, before (left) and after (right) application of the TileCal correction	
366	tool. . . . .	152
367	C.1 Index of jets truth matched (by requirement of $\Delta R < 0.4$ ) with dark quark. . . . .	153
368	C.2 Percent of jets with $\Delta R(j, E_T^{\text{miss}}) < 0.4$ comparing two jet identification strategies.	
369	Leading and subleading jets are seen to be the better metric for identifying jets	
370	associated with the dark quark decay. . . . .	154
371	D.1 Example determinations of the 60% mass window means for several signal points. . . . .	156
372	D.2 Signal mass resolution for $m_T$ binning for the signal grid in $(R_{inv}, \text{mass})$ space. . . . .	156
373	D.3 $m_T$ bins based on the signal mass resolution and the minimum 100 GeV width	
374	requirement, for each $R_{inv}$ signal category. . . . .	157

## List of Tables

376	4.1 General performance goals of the ATLAS detector [34]. . . . .	27
377	6.1 Fixed parameters in the Pythia8 HV model . . . . .	65
378	6.2 Values for $m_{dark}$ . . . . .	65
379	6.3 Mass points and cross sections of the SVJ search signal grid. The cross section is 380 determined only by the $Z'$ mass and is not impacted by the $R_{inv}$ . . . . .	65
381	8.1 Preselection cuts for data (left) and signal (right). . . . .	93
382	8.2 Post-fit parameters for the PFN CR and VR. $p1$ can also be considered $N_{bkg}$ or the 383 normalization factor. . . . .	105
384	8.3 Post-fit parameters for the ANTELOPE CR and VR. . . . .	112
385	9.1 Post-fit parameters for the PFN SR. $p1$ can also be considered $N_{bkg}$ or the normal- 386 ization factor. . . . .	118
387	9.2 Summary of Experimental Uncertainties and their impact on the yield of MC signal 388 events. . . . .	120

389

## Acknowledgements

390        Insert your acknowledgements text here. This page is optional, you may delete it if not  
391        needed.

392

## **Dedication**

393

Dedicated to my friends and family

394

## **Introduction or Preface**

395        Insert your preface text here if applicable. This page is optional, you may delete it if not  
396        needed. If you delete this page make sure to move page counter comment in thesis.tex to correct  
397        location.

398

## **Part I**

399

## **Theory**

400

401

## Chapter 1: The Standard Model

402     The Standard Model of particle physics is a universally accepted framework which explains  
403     the interactions of fundamental particles. All known fundamental particles, outlined in Figure  
404     1.1, are represented in the Standard Model. The model describes three of the four known forces:  
405     the electromagnetic force, the weak force, and the strong force. Gravity, the fourth fundamental  
406     force, is not addressed by the Standard Model. The Standard Model was primarily developed over  
407     the course of the 1960s and 1970s, by combining the work of many physicists into one coherent  
408     model. The Standard Model has been established as a well-tested theory by decades of experimen-  
409     tal physics research.

410     This chapter will seek to introduce the phenomenology and mathematical foundations of the  
411     Standard Model, and present the supporting experimental evidence. Phenomenon which are unex-  
412     plained by the Standard Model such as gravity will be considered at the end of the chapter, leading  
413     to an exploration of theories beyond the Standard Model in the subsequent chapter.

414     **1.1 Phenomenology: Particles and Forces**

415     **1.1.1 Particles**

416     A classic representation of the particles comprising the Standard Model is shown in Figure  
417     1.1. The two primary particles classes are bosons (gauge bosons and the scalar Higgs boson) and  
418     fermions (leptons and quarks). The bosons are carriers of fundamental forces, while the fermions  
419     are the building blocks of matter. Fermions are sorted into three *generations*, and each fermion is  
420     identified by a unique *flavor*.

421     Each entry in the table in Figure 1.1 is accompanied by 3 characteristic numbers: mass, charge,  
422     and spin. The mass of each particle is determined to limited precision by experimental observation,

## Standard Model of Elementary Particles

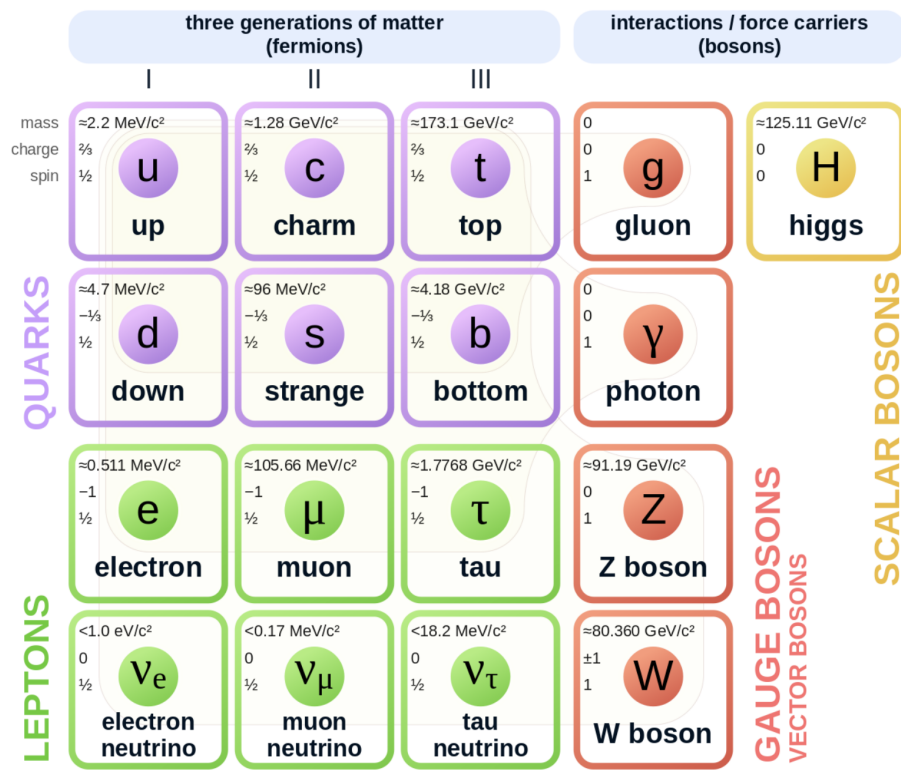


Figure 1.1: Diagram of the 17 particles comprising the Standard Model

423 with the exception of photons and gluons which are known to be massless. Charge refers to the  
424 electromagnetic charge, which is integer for leptons and fractional for quarks. Spin is an intrinsic  
425 form of angular momentum carried by fundamental particles; all fermions have half integer spin,  
426 while bosons have integer spin.

427 Each particle is also known to have an *antiparticle*. Each antiparticle has the same mass but the  
428 opposite charge of their Standard Model counter part; for example, the antiparticle of the electron  
429 is the positron, which has all the same properties but a positive charge. The photon, Z boson,  
430 and Higgs are each their own antiparticle. The nature of antineutrinos is an open question driving  
431 neutrino physics research, as it is not currently known whether neutrinos are their own antiparticle.

432 1.1.2 Forces

433 The three fundamental forces explained by the Standard Model are the electromagnetic force,  
434 the strong force, and the weak force. The photon is the carrier of the electromagnetic force, which  
435 dictates the nature of interactions between electrically charged particles, and is widely covered by  
436 introductory physics courses. The electromagnetic force has an infinite interaction range, a result  
437 of the massless and non-self interaction nature of the photon. The electromagnetic interaction is  
438 described by the theory of quantum electrodynamics (QED).

439 The weak force gives rise to atomic radiation and decay. It allows for the processes of beta  
440 decay, which enables conversion between neutrons and protons within the nucleus of an atom. In  
441 the process of beta decay, a proton decays into a neutron, a positron, and a neutrino; or, a neutron  
442 decays into a proton, an electron and an antineutrino. The weak interaction allows for quark flavor  
443 mixing, the which enables beta decay. The  $W^+$ ,  $W^-$ , and  $Z^0$  are the force carriers of the weak force.  
444 The effective range of the weak force is limited to subatomic distances, as a result of the massive  
445 nature of the mediator bosons. The unified theory of the electroweak interaction posits that at high  
446 enough energies the electromagnetic interaction and the weak force merge into the same force.  
447 This threshold is termed the unification energy and calculated to be about 246 GeV [1].

448 The strong force confines quarks into hadron particles, such as protons and neutrons. The

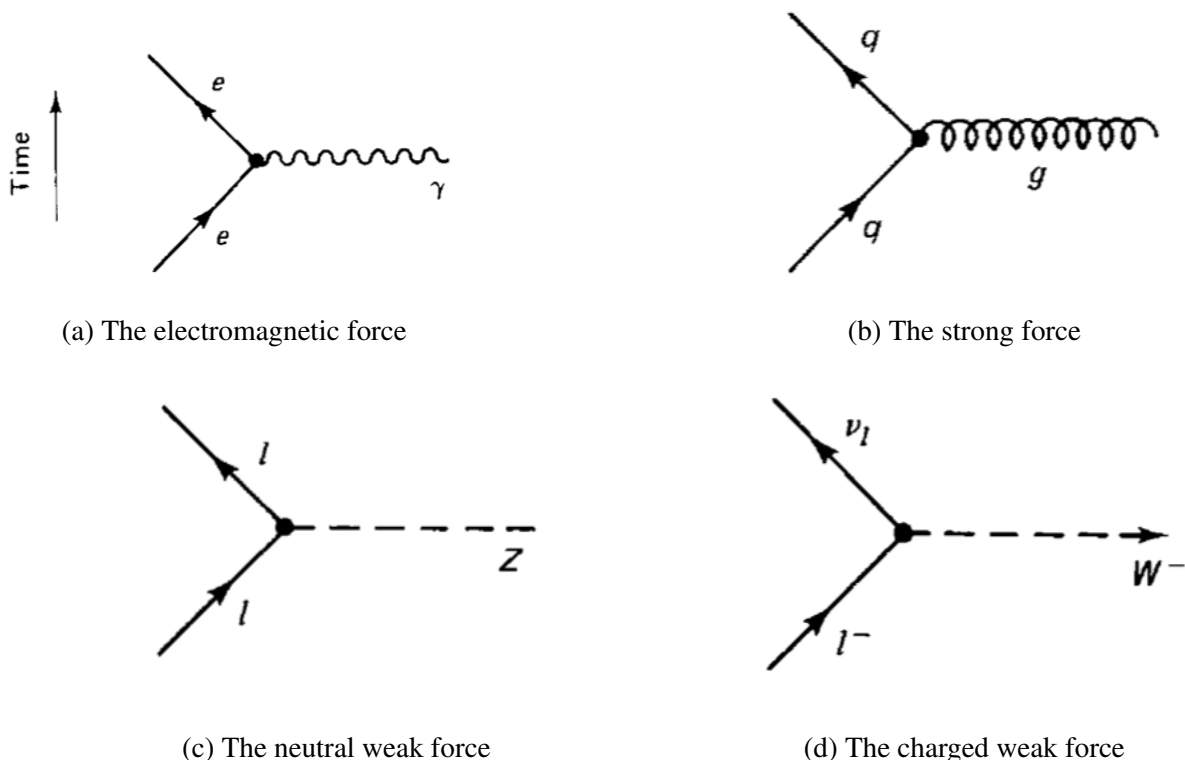


Figure 1.2: Fundamental particle interactions of the three fundamental forces described by the Standard Model [2].

449 strong force also allows for the creation of atomic nuclei by binding protons and neutrons together,  
450 and is generally referred to as the “nuclear force” in this context. The gluon is the mediator of  
451 the strong force, which is a short-range force which acts at subatomic distances on the order of  
452  $10^{-15}$  m. At this range, the strong force is about 100x as strong as the electromagnetic force,  
453 which allows for the creation of positively charged nuclei [2]. The strong force is described by the  
454 theory of quantum chromodynamics (QCD). In the same way that QED dictates the interaction of  
455 electrically charges particles, QCD dictates the interactions of *color-charged* particles. Due to the  
456 particular importance of QCD in this thesis, this topic will be explored in detail in section 1.2.

457 The fundamental Feynmann diagram for each of the three forces discussed here is depicted  
458 in Figure 1.2. The fourth fundamental force, gravity, is not currently explained by any known  
459 mechanism within the Standard Model.

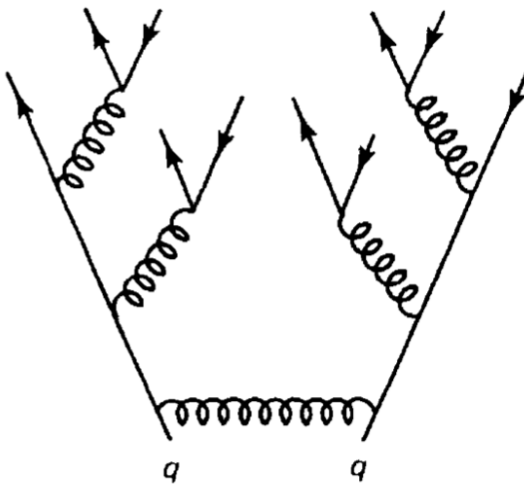


Figure 1.3: An example Feynmann diagram of jet production

## 460 1.2 QCD and Jets

461 While there is only one type of electric charge, there are three types of color charge; red, green,  
 462 and blue. In the process  $q \rightarrow q + g$ , the color of the quark can change. In order to conserve color  
 463 charge, gluons are bicolored, and always carry some positive color charge and some negative color  
 464 charge.

465 Color charged particles can only exist in bound states which result in a neutral total color  
 466 charge, a principle known as confinement. This requires that quarks and gluons exist in group  
 467 states known as hadrons; either mesons in the case of two quarks or baryons in the case of three  
 468 quarks. When a quark is separated from a hadron, confinement dictates that other colored objects  
 469 are produced around the quark to obey confinement. An example of this process is shown in  
 470 Figure 1.3. This ensemble of objects, generally a mixture of quarks and gluons, is termed a *jet*.  
 471 Jets are among the most common phenomenon observed by detectors at hadron colliders, and their  
 472 complex structure makes them a key focus of many physics analyses.

473    **1.3 Symmetries**

474    The Standard Model is a renormalizable quantum field theory that obeys the local symmetry

475     $G_{SM}$ :

$$G_{SM} = SU(3)_C \times SU(2)_L \times U(1)_Y. \quad (1.1)$$

476    The  $SU(3)_C$  symmetry component represents the non-Abelian gauge group of QCD. There  
477    are 8 generators for the  $SU_C(3)$  group which correspond to 8 types of gluon, each representing a  
478    different superposition of color charge [3]. The  $SU(2)_L \times U(1)_Y$  symmetry group represents the  
479    electroweak sector of the Standard Model, which can be spontaneously broken into the electromag-  
480    netic and weak sectors. There are 4 generators for this group, which correspond to four massless  
481    gauge bosons  $W^1$ ,  $W^2$ ,  $W^3$ , and  $B$ . From these massless gauge bosons are formed the massive  
482    mediators of the weak force, the  $W^-$ ,  $W^+$  and  $Z^0$  bosons, and the massless electromagnetic force  
483    carrier, the photon  $\gamma$ . Spontaneous symmetry breaking and the process by which gauge bosons  
484    acquire mass will be addressed in section 1.3.1.

485    Noether's theorem [4] stipulates that any continuous symmetry is associated with a conserved  
486    quantity. In the Standard Model, this means that the  $SU(3)_C$  symmetry gives rise to conservation of  
487    color charge. The  $SU(2)_L \times U(1)_Y$  symmetry gives rise to conservation of electromagnetic charge.  
488    Conservation of spin results from the Poincaré symmetry described by the theory of special rela-  
489    tivity, which combined with Noether's theorem gives us the conservation of energy, momentum,  
490    and angular momentum.

491    The SM Lagrangian is invariant under  $CPT$  symmetry, or charge, parity, and time reversal.  
492    Charge conjugation ( $C$ ) transform a particle into its corresponding antiparticle by reversing the  
493    charge and other quantum numbers. Parity conjugation ( $P$ ) reverses spatial coordinates, which  
494    transforms left-handed particles into right-handed particles and vice-versa. Time reversal ( $T$ ) is  
495    the theoretical process of reversing time. The  $L$  subscript in the  $SU(2)_L$  group indicates that this  
496    symmetry only applies to left-handed fermions. As a result, the  $W^{1,2,3}$  gauge bosons of  $SU(2)_L$

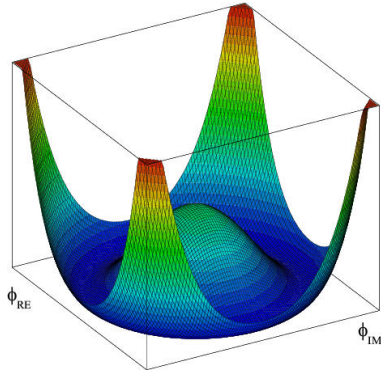


Figure 1.4: An illustration of the “hat shaped” potential of the Higgs field, resulting in a non-zero vacuum expectation value.

only interact with left handed particles, a process which maximally violates P-symmetry in the weak force. A small amount of the CP symmetry violation is also observed in the Standard Model, through the decays of strange flavored mesons [5] and  $b$ -mesons [6]. The CPT theorem posits that the violation of CP symmetry implies that T-symmetry must also be violated, so that CPT is a preserved symmetry.

### 1.3.1 Spontaneous Symmetry Breaking and The Higgs Mechanism

Spontaneous symmetry breaking is the process by which a Lagrangian obeys a symmetry at high energies, but exhibits asymmetric behavior at lower energies. The electroweak symmetry group is spontaneously broken as  $SU(2)_L \times U(1)_Y \rightarrow U(1)_{EM}$ . The quantity conserved by the  $SU(2)_L$  symmetry is weak isospin  $T_{1,2,3}$ , while the quantity conserved by  $U(1)_Y$  symmetry is weak hypercharge  $Y$ . Below very high energies, the presence of the Higgs field causes the electroweak symmetry to break. The Higgs field is a scalar field which forms a complex doublet of the  $SU(2)$  symmetry group, with four degrees of freedom. The shape of the Higgs field potential, shown in Figure 1.4, results in a ground state with a non-zero vacuum expectation value; thus the Higgs field takes a non-zero value throughout all space, which breaks the symmetry of the weak isospin  $SU(2)$  group.

The interaction with the Higgs field mixes the four massless gauge bosons  $W^{1,2,3}$  and  $B$ . Three Higgs field degrees of freedom mix with the massless gauge bosons, resulting in three massive

515 gauge bosons  $W^-$ ,  $W^+$  and  $Z^0$ . The massless photon  $\gamma$  is created from the components of the  
516 massless gauge bosons which do not interact with the Higgs field. The scalar Higgs boson arises  
517 from the one unmixed degree of freedom the Higgs field. Spontaneous symmetry breaking also  
518 violates the conservation of weak isospin and weak hypercharge, leaving only electromagnetic  
519 charge ( $Q = T_3 + \frac{1}{2}Y$ ) as a conserved quantity associated with the  $U(1)_{EM}$  symmetry.

## 520 1.4 Experimental Validation of the Standard Model

521 The theoretical framework of the Standard Model coalesced into a unified theory in the mid-  
522 20th century. A cascade of discoveries providing empirical evidence for the model followed  
523 closely. In the 1960s, three quarks (up, down and strange) and four leptons (electron, muon,  
524 and their associated neutrinos) were the known particulate building blocks of matter and the Stan-  
525 dard Model. The discovery of the charm quark in 1974, through the observation of the  $J/\psi$  meson  
526 [7][8], confirmed the existence of a fourth quark flavor. The discovery of the  $\tau$  in 1975 [9] provided  
527 the first evidence of a 3rd generation of matter. This was quickly followed by the observation of  
528 the  $\Upsilon$  meson in 1977 [10], which provided evidence for the existence of a fifth quark, the  $b$  quark  
529 (bottom, or beauty). The existence of a 3rd generation of fermion also explained the observation  
530 of CP violation in the weak force, as it allowed for the addition of a complex phase in the CKM  
531 matrix (a unitary matrix which describes flavor mixing in the weak interaction). The top quark  
532 ( $t$ ) and tau neutrino ( $\nu_\tau$ ) were predicted at this point as the final building blocks of three complete  
533 generations of fermions, and they were discovered by experimental observation around the turn of  
534 the 21st century [11] [12] [13].

535 The W and Z bosons were predicted by the Standard Model, but to observe them required the  
536 construction of a particle accelerator powerful enough to produce them. They were finally observed  
537 at CERN in 1983 by the UA1 and UA2 experiments [14] [15] at the newly constructed Super Proton  
538 Synchrotron (SPS). Their masses were observed to be compatible with the masses predicted by the  
539 Standard Model nearly a decade earlier. The final missing piece then was confirming the existence  
540 of the Higgs, which again required the construction of a newer and more powerful collider. CERN

541 achieved this with the construction of the Large Hadron Collider (LHC), and in 2012 the ATLAS  
542 and CMS experiments announced the discovery of the Higgs particle [16] [17].

## 543 1.5 Limitations of the Standard Model

544 While the Standard Model has enjoyed decades of experimental results which confirm its pre-  
545 dictions, there are several glaring shortcomings. The observed phenomenon for which the Standard  
546 Model provides no explanation are summarized below.

- 547 • Gravity - the Standard Model does not account for the fourth fundamental force of gravity.
- 548 • Dark Matter - there is no viable candidate to explain the existence of dark matter, a non-  
549 interacting form of matter which must exist to account for gravitational observations which  
550 cannot be explained by general relativity, such as the motion of galaxies, gravitational lens-  
551 ing, and the structure of the universe [18].
- 552 • Matter-Antimatter asymmetry - the level of CP violation in the Standard Model isn't suf-  
553 ficient to explain the large discrepancy between the amount of matter and the amount of  
554 antimatter in the universe today, and the origins of this imbalance are not understood.
- 555 • Neutrino masses - the Standard Model assumes that neutrinos are massless and provides  
556 no mechanism for them to acquire mass. However, observations of neutrino oscillations  
557 indicates they posses some small non-zero mass [19].

558 In addition to these unexplained natural phenomenon, there are several questions about the  
559 *naturalness* of the Standard Model. The principle of naturalness states that dimensionless ratios  
560 between physical constants should be of order 1, and that nature should not be arbitrarily fine-  
561 tuned. While this is largely an aesthetic argument, it points to many aspects of the Standard Model  
562 for which there exists no natural explanation.

- 563 • Strong CP - while CP symmetry is violated in the weak force, observations indicate that it  
564 is preserved by the strong force [20]. The Standard Model predicts that CP violation in the

565 strong force is possible. There is no principle which motivates this incongruity between the  
566 weak force and strong force.

- 567 • Hierarchy Problem - The wide range of masses for elementary particles and the wide range of  
568 scales at which the four fundamental forces operate is not motivated by the SM. Specifically,  
569 it is not understood why the Higgs mass is observed to be well below the Plank scale  $\lambda$ ,  
570 which is the energy level at which the effects of quantum gravity become significant. QFT  
571 indicates that the Higgs mass is determined by contributions from all energy scales including  
572  $\lambda$ , meaning that its observed mass is inexplicably small.

573 The limitations of the Standard Model provide a road map for theoretical and experimental  
574 particle physicists, who seek to develop new theories which account for these observations, and  
575 then to find evidence which might support these *Beyond the Standard Model* (BSM) theories. The  
576 next chapter will introduce the BSM theories which motivate the physics search presented in this  
577 thesis.

## Chapter 2: Physics Beyond the Standard Model

580 In light of the various phenomenon unexplained by the Standard Model, physicists have pro-  
 581 posed various extensions to the Standard Model, collectively termed *Beyond the Standard Model*  
 582 (BSM) theories. A particular focus of the physics programs at the Large Hadron Collider (LHC)  
 583 are BSM models which suggest dark matter candidate particles. If these particles couple to Stan-  
 584 dard Model, they could be produced and observed at the LHC. This chapter will explore Hidden  
 585 Valley models, and in particular the potential for Hidden Valley models to produce *semi-visible*  
 586 *jets*. This will set the theoretical foundations for the experimental search presented in the later  
 587 chapters of this thesis. The mechanisms of dark QCD that arise from these models and allow for  
 588 the production of semi-visible jets will also be discussed.

589 **2.1 Hidden Valley Models**

590 Hidden Valley (HV) models are a category of BSM models that allow for dark matter (DM)  
 591 production at the LHC. They extend the Standard Model with an additional non-Abelian gauge  
 592 group [21]. This introduces the possibility of a complex dark sector, which mirrors the complexities  
 593 of Standard Model QCD, and introduces the possibility of dark quarks and gluons. The term  
 594 “hidden valley” refers to the idea that the DM is hidden from the SM by a high-energy barrier, as  
 595 illustrated in Figure 2.1. The dark sector is assumed to communicate with the Standard Model via  
 596 a “portal”, or “messenger particle”, that can interact with both Standard Model and HV forces. For  
 597 the s-channel scenario, the portal is considered to be a new massive mediator particle  $Z'$ .

598 The portal particle allows for the production of dark sector particles at hadron colliders. If  
 599 dark quarks are produced via the decay  $Z' \rightarrow q_D q_D$  they can hadronize and form dark jets. The  
 600 properties of the dark jets are determined by the dynamics of the dark sector, which are explored in

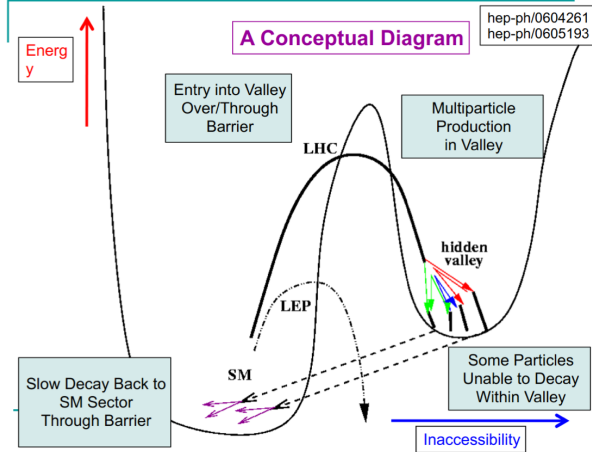


Figure 2.1: Illustration of the hidden valley potential.

601 the subsequent section. Depending on the details of the model, the jets formed by the dark hadrons  
 602 can be categorized as fully dark, semi-visible, leptonic, emerging, or other [21].

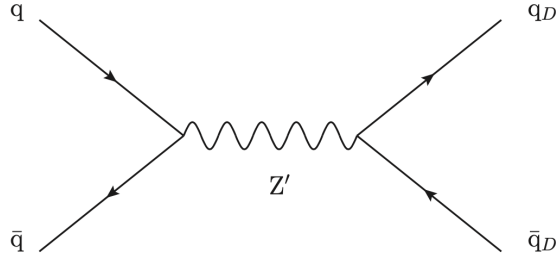


Figure 2.2: The massive mediator particle  $Z'$  of the s-channel realization of a HV model

## 603 2.2 Dark QCD

604 The theoretical underpinning of the semi-visible jet phenomenology is a dark sector with a  
 605 gauge group  $SU(N)_d$  leading to confinement at a scale  $\Lambda_d$ . For illustration, let's consider the  
 606 case of an  $SU(2)_d$  gauge theory, which gives rise to two dark fermionic generations  $\chi_a = \chi_1, \chi_2$ .  
 607 Following the work of Ref [22] we can write the fundamental dark Lagrangian as:

$$\mathcal{L}_{dark} \supset -\frac{1}{2} \text{Tr} G_{\mu\nu}^d G^{d\mu\nu} - \bar{\chi}_a (i\cancel{D} - M_{d,a}) \chi_a \quad (2.1)$$

608        The first term allows for the dark gluons to self-interact, while the second term enables the dark  
609        quarks to hadronize and acquire mass. The dark quarks are assumed to have a common mass  $M_d$ .  
610        The coupling strength of the strongly interacting dark quarks is termed  $\alpha_d$ . At the confinement  
611        scale  $\Lambda_d$ , the dark quarks can form bound states. At the scale  $M_d \approx \Lambda_d$  a QCD-like shower occurs.

612        The properties of the hadrons formed by the dark quarks are of particular importance to the  
613        observed dark QCD dynamics. Dark-isospin number  $U(1)_{1-2}$  and dark-baryon number  $U(1)_{1+2}$   
614        are accidental symmetries of the theory which determine the stability of the hadrons. In the case  
615        of two dark flavors, six dark hadrons can be formed: four mesons ( $\chi_1\bar{\chi}_1$ ,  $\chi_2\bar{\chi}_2$ ,  $\chi_1\bar{\chi}_2$ ,  $\bar{\chi}_1\chi_2$ ) and  
616        two baryons ( $\bar{\chi}_1\bar{\chi}_2$ ,  $\bar{\chi}_1\bar{\chi}_2$ ). The mesons  $\chi_1\bar{\chi}_2$  and  $\bar{\chi}_1\chi_2$  are charged under dark-isospin and will be  
617        stable if this symmetry is unbroken. The baryons would also be stable as they are charged under  
618        the dark-baryon number. These four stable hadrons become dark matter candidates of the theory.  
619        The  $\chi_1\bar{\chi}_1$  and  $\chi_2\bar{\chi}_2$  mesons are not charged under either symmetry and are thus expected to decay.  
620        The unstable mesons can decay into stable dark mesons, or into an off-shell  $Z'$ . The off-shell  $Z'$   
621        will then decay into two DM quarks or two SM quarks, and its products will continue to shower  
622        until the final state particles are stable.

623        The number of stable and unstable dark states varies substantially depending on the details  
624        of the model. The model discussed above can be generalized from  $SU(2)_d$  to  $SU(N)_d$ , with any  
625        number of colors  $N_c$  or flavors  $N_f$ . This affects the ratio of possible stable to unstable mesons,  
626        which can directly impact the amount of missing energy. The fraction of missing energy is a  
627        variable in many dark QCD models, and is especially important in the case of semi-visible jets.

## 628        **2.3 Semi-visible Jets**

629        A “semi-visible jet” occurs when the heavy  $Z'$  messenger particle decays into dark quarks,  
630        which then hadronize in a QCD-like shower. If some of the dark hadrons are stable while others  
631        decay to SM quarks via the off-shell  $Z'$ , a collimated mixture of visible and dark matter is formed  
632        – this is termed a semi-visible jet. If the  $Z'$  messenger particle is produced at rest, the two jets will  
633        be back-to-back in the transverse plane. If there is an imbalance in the amount of invisible particles

634 between the two jets, one of the jets will be observed to be aligned with missing transverse energy.

635 While there are a myriad of HV and dark QCD models, a handful of model parameters are most  
636 important in determining the observable of these showers within a particle detector. The coupling  
637 strength  $\alpha_d$  is one of the most important, as it controls the fraction of dark hadrons emitted in the  
638 shower and their average  $p_T$ . The mass of the dark quarks directly impacts the jet mass. If the  
639 masses of the dark quark flavors are comparable, the ratio of stable to unstable dark hadrons will  
640 be approximately 1:1. However, if there is a mass splitting, stable or unstable dark hadrons may  
641 be favored, which impacts the amount of missing energy observed.

642 The ratio of stable to unstable dark hadrons in the shower is a critical variable for capturing the  
643 behavior of dark showers. This value is termed  $R_{inv}$ :

$$R_{inv} = \frac{\# \text{ of stable hadrons}}{\# \text{ of hadrons}} \quad (2.2)$$

644 Events containing jets aligned with missing transverse momentum are generally considered to  
645 be misreconstructed by other DM searches, and therefore discarded. This class of final states is  
646 therefore largely uncovered by existing DM searches. The nature of the dark hadron shower is  
647 determined by the following parameters: the  $Z'$  mass  $m_{Z'}$ , the  $Z'$  couplings to visible and dark  
648 quarks  $g_q$  and  $g_{q_D}$ , the number of dark colors and flavors, the characteristic scale of the dark sector  
649 confinement  $\Lambda_D$ , the mass scale of the dark hadrons  $m_D$ , and the average fraction of stable hadrons  
650 in the decay  $R_{inv}$ . The coupling to SM quarks determines the  $Z'$  production cross section.

651

## **Part II**

652

## **Experiment**

653

654

## Chapter 3: The Large Hadron Collider

655       The Large Hadron Collider (LHC) is a 26.7 km circular high-energy particle accelerator, span-  
656       ning the Swiss-French border near the city of Geneva, Switzerland [23]. The LHC occupies the  
657       tunnel constructed in 1989 for the Large Electron-Positron (LEP) Collider, and reaches a maxi-  
658       mum depth of 170m below the surface. The LHC is operated by the European Organization for  
659       Nuclear Research (CERN), the largest international scientific collaboration in the world.

660       The LHC accelerates protons and heavy ions, and collides them at four interaction points  
661       around the ring, with a design center-of-mass energy per collision of  $\sqrt{s} = 14$  TeV. Each interaction  
662       point is home to one of four detector experiments, which study the products of the collisions. The  
663       largest of these experiments is the ATLAS detector, a general purpose detector designed to study  
664       the Standard Model and search for new physics that could be produced in LHC collisions [24].  
665       The CMS detector is another general purpose detector, designed and operated independently of the  
666       ATLAS detector, but intended to probe the same range of physics [25]. The ALICE experiment is  
667       a dedicated heavy ion experiment, and the LHC-b experiment is a dedicated *b*-physics experiment  
668       [26] [27].

669       This chapter will cover the multi-component accelerator complex powering the LHC, the state-  
670       of-the-art magnets which steer the particle beams, measurements of the intensity and number of  
671       collisions produced by the LHC, and finally an overview of LHC activities in the past, present, and  
672       future.

673 **3.1 Accelerator Physics**

674 **3.1.1 The Journey of a Proton**

675 From 2010 - 2018, the protons which fed the LHC started as hydrogen gas. The electrons were  
676 removed from the hydrogen atoms through the use of strong electric fields. The linear accelerator  
677 LINAC2 then accelerated the protons to an energy of 50 MeV. Between 2018 and 2020, LINAC2  
678 was replaced with LINAC4, which instead accelerates  $H^-$  ions, hydrogen atoms with two electrons.  
679 LINAC4 is capable of accelerating the  $H^-$  ions to 160 MeV. Before injection to the next part of  
680 the acceleration chain, both electrons are stripped from the  $H^-$  ions, leaving just protons. From  
681 here the protons enter the Proton Synchrotron booster, where they are accelerated up to 1.4 GeV of  
682 energy. Subsequently they are sorted into bunches separated in time by 25 ns, where each bunch  
683 contains approximately  $10^{11}$  protons. Next the bunches pass through the Proton Synchrotron (PS)  
684 and the Super Proton Synchrotron (SPS), where they reach energies of 25 GeV and 450 GeV  
685 respectively. Finally they are injected into the LHC as two beams traveling in opposite direction.  
686 The original design allowed each beam to be accelerated up to 7 TeV of energy. Due to limitations  
687 in the performance of the superconducting LHC magnets, the highest energy actually achieved by  
688 the LHC beams during Run 2 was 6.5 TeV, giving a collision center-of-mass energy of  $\sqrt{s} = 13$   
689 TeV [28]. Figure 3.1 shows the full LHC accelerator complex.

690 Acceleration in the LHC is performed by eight radio frequency (RF) cavities located around the  
691 ring. Each RF cavity produces a 2 MV electric field oscillating at 40 MHz. The 40MHz oscillation  
692 produces a point of stable equilibrium every 2.5 ns. These points of equilibrium are synchronized  
693 with the occurrence of the proton bunches produced in the PS – a proton bunch occupies one out  
694 of every ten points of stable equilibrium, such that the bunches maintain a 25 ns spacing [28].

695

## The CERN accelerator complex Complexe des accélérateurs du CERN

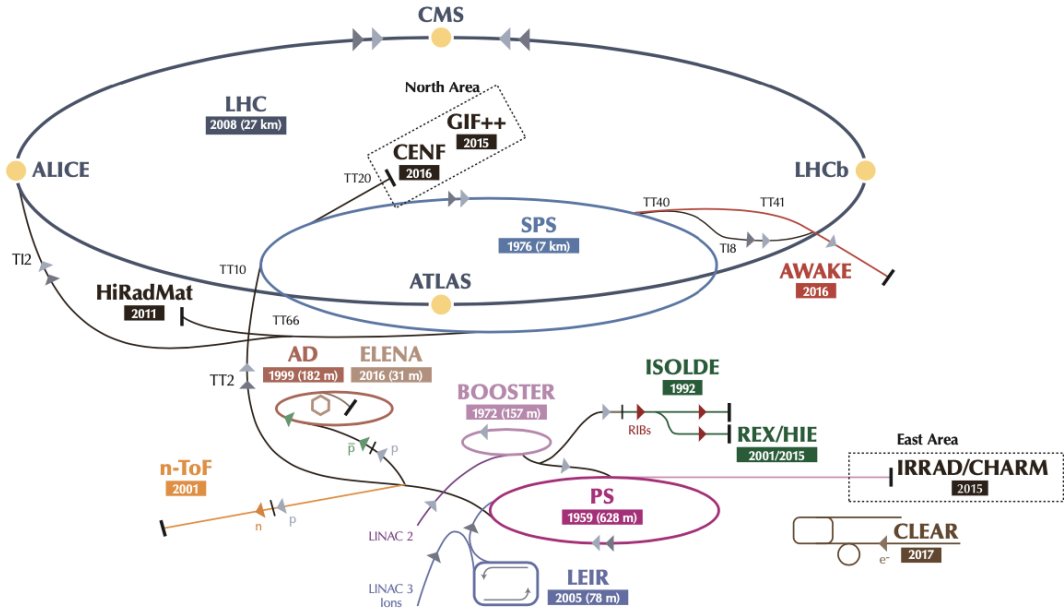


Figure 3.1: The LHC accelerator complex at CERN [29]

### 696 3.1.2 Magnets

697 In addition to the acceleration cavities, the LHC houses 9593 superconducting magnets which  
 698 direct and focus the proton beam on its 27 kilometer journey. The magnets are comprised of super-  
 699 conducting Niobium-Titanium coils cooled to 1.9K by superfluid helium. As the beams approach  
 700 one of the four collision points around the ring, multipole magnets focus and squeeze the beam for  
 701 optimal collisions [28].

702 The LHC is divided into sections, where each section contains an arc and a straight insertion. The arcs are composed of 1232 large dipole magnets which bend the beam  
 703 to follow the roughly circular 27 km path. The main dipoles generate powerful 8.3 tesla magnetic  
 704 fields to achieve this bend. Each dipole magnet is 15 meters long and weighs 35 tonnes. The  
 705 dipoles work in conjunction with quadrupole magnets, which keep the particles in a focused beam,  
 706 and smaller sextupole, octupole and decapole magnets which tune the magnetic field at the ends of  
 707 the dipole magnets [30].

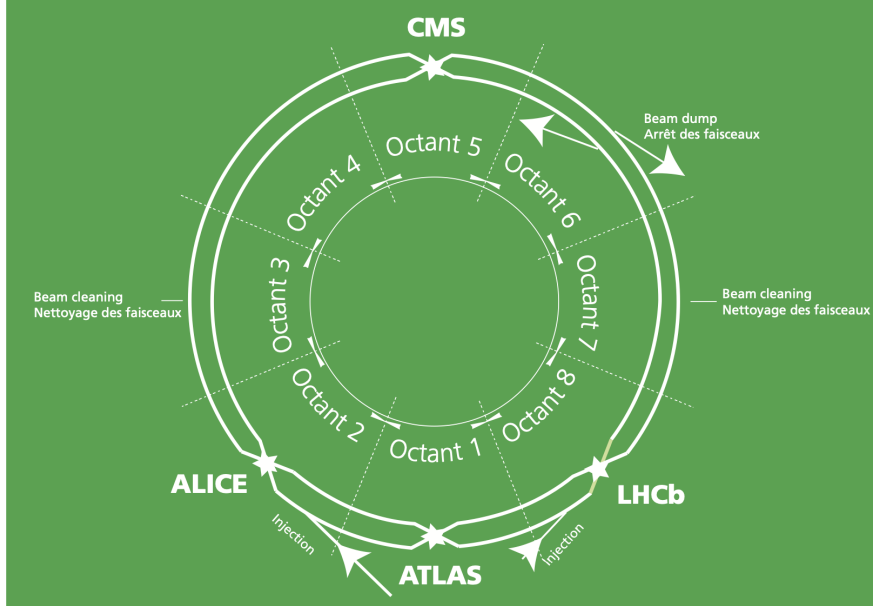


Figure 3.2: The octants of the LHC and location of various beam activities [28]. Stars indicate the locations of beam collisions, and the associated detectors recording the outcome of those collisions.

709     The straight insertion sections have different purposes depending on their location around the  
 710     ring: beam collisions, beam injection, beam dumping, or beam cleaning. At the four collision  
 711     points, insertion magnets squeeze the beam to ensure a highly focused collision. This is accom-  
 712     plished with a triplet of quadrupole magnets, which tighten the beam from 0.2 millimeters to just  
 713     16 micrometers in diameter. Insertion magnets also clean the beam, which prevents stray particles  
 714     from hitting sensitive components throughout the LHC. When the LHC is ready to dispose of a  
 715     beam of particles, beam dump magnets deflect the path of the beam into a straight line towards  
 716     a block of concrete and graphite that stops the beam. A dilution magnet then reduces the beam  
 717     intensity by a factor of 100,000 before the final stop [30]. Figure 3.2 shows the locations various  
 718     beam activities.

### 719     3.2 Luminosity

720     Collisions at the LHC occur when the two beams of proton bunches cross at one of the four  
 721     interaction points. The intensity of collisions is described by the instantaneous luminosity, the

722 formula for which is given in equation 3.1.

$$L = \frac{fN_1N_2}{4\pi\sigma_x\sigma_y} \quad (3.1)$$

723 Here  $f$  is the revolution frequency,  $N_1$  and  $N_2$  are the number of particle per bunch for each  
724 beam, and  $\sigma_x$ ,  $\sigma_y$  are the horizontal and vertical beam widths.

725 The instantaneous luminosity gives the number of the collisions that could be produced at the  
726 interaction point per unit of cross-sectional area per unit of time, generally expressed in  $\text{cm}^{-2}\text{s}^{-1}$ .  
727 The integrated luminosity is obtained by integrating the instantaneous luminosity over a given  
728 block of time, and measures the total number of collisions which have occurred during that op-  
729 eration period. The total integrated luminosity is directly correlated with the size of the datasets  
730 collected by the LHC experiments. Total integrated luminosity for Run 2 is illustrated in Figure  
731 3.3.

732 High levels of instantaneous luminosity result in multiple  $pp$  collisions per bunch crossing,  
733 which leads to an effect known as *pileup*. Pileup poses a challenge for detector physics, as recon-  
734 structing the products of multiple simultaneous events is far more challenging than reconstructing  
735 a single event with no pileup. Pileup conditions vary from year-to-year and run-to-run of LHC op-  
736 eration, and the impact of these conditions are taken into account when analyzing the data, as will  
737 be discussed further in Chapter 5. Measurement of pileup conditions during Run 2 are illustrated  
738 in Figure 3.3.

739 The design peak luminosity of the LHC is  $1.0 \times 10^{34} \text{ cm}^{-2}\text{s}^{-1}$ . During Run 1 of the LHC the  
740 peak instantaneous luminosity was  $0.8 \times 10^{34} \text{ cm}^{-2}\text{s}^{-1}$ . Over the course of Run 1 the LHC collected  
741 a total integrated luminosity of  $5.46 \text{ fb}^{-1}$  at  $\sqrt{s} = 7 \text{ TeV}$ , and  $22.8 \text{ fb}^{-1}$  at  $\sqrt{s} = 8 \text{ TeV}$ . Following the  
742 first long shutdown and upgrade phase of operations, the LHC achieved a center of mass energy  
743  $\sqrt{s} = 13 \text{ TeV}$  at the beginning of Run 2 in 2015. The LHC was also able to deliver  $2.0 \times 10^{34}$   
744  $\text{cm}^{-2}\text{s}^{-1}$  peak instantaneous luminosity, double the design value. During LHC Run 2, from 2015-  
745 2018, the LHC delivered  $156 \text{ fb}^{-1}$  of integrated luminosity for proton-proton collisions. Run 3 of

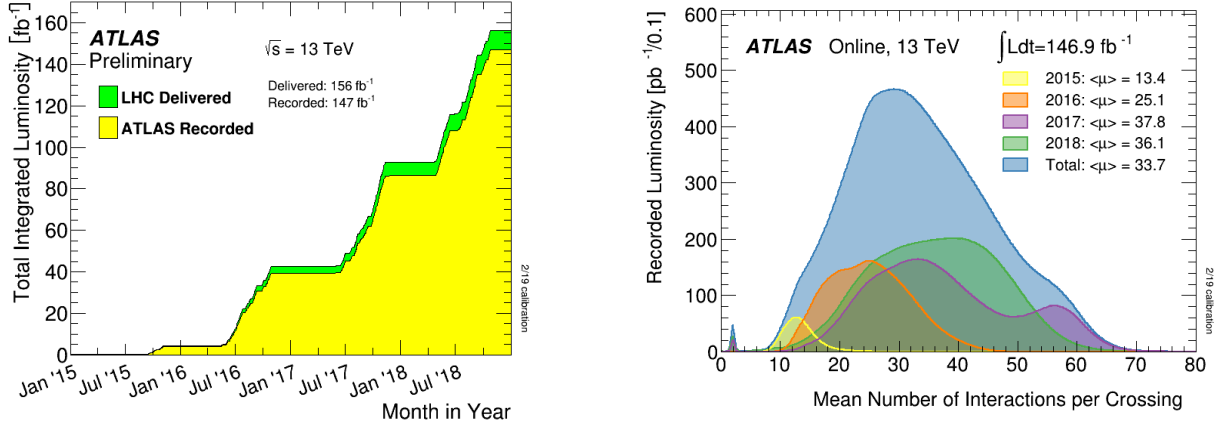


Figure 3.3: (Left) Total integrated luminosity over the course of Run 2. (Right) Average number of  $pp$  interactions per bunch crossing in Run 2. Each curve is weighted by the integrated luminosity for the year.

746 the LHC began in 2022, and is expected to deliver  $250 \text{ fb}^{-1}$  of integrated luminosity to the ATLAS  
 747 and CMS experiments by 2026 [31].

748 The goal of LHC physic analyses is to find and study rare events produced by interesting  
 749 physics processes. The cross section  $\sigma$  of a given process indicates the probability of that process  
 750 occurring given the beam conditions of the LHC. Multiplying the cross section by the integrated  
 751 luminosity of a dataset gives the expected number of events for that process within the dataset.

$$N_{\text{events}} = \int \sigma L(t) dt = \mathcal{L} \times \sigma \quad (3.2)$$

752 The cross section for most processes of interest, especially BSM processes, is several orders of  
 753 magnitude below the total cross section for the LHC. Therefore maximizing the number of events  
 754 produced in collisions is crucial to increase the likelihood of producing events from processes of  
 755 interest. For this reason, maximizing instantaneous luminosity is a key factor in accelerator design  
 756 and operation, while mitigating the resulting pileup effects is a key component in detector design  
 757 and operation.

758    **3.3 LHC Timeline**

759    The first proton-proton collisions at the LHC were achieved in 2010 with a center-of-mass  
760    energy of  $\sqrt{s} = 7$  TeV. Run 1 of the LHC took place between 2010 and early 2013, during which  
761    time the center-of-mass collision energy increased from 7 TeV to 8 TeV. Figure 3.4 shows an  
762    overview of LHC activities beginning in 2011, in the midst of Run 1. The data collected during  
763    Run 1 led to the discovery of the Higgs Boston in 2012 [32].

764    Between 2013 and 2015 the LHC underwent the first Long Shutdown (LS1) during which  
765    time maintenance and renovation was performed on the accelerator chain, including the repair and  
766    consolidation of the high-current splices which connect the super-conducting LHC magnets. Run  
767    2 of the LHC took place from 2015 to 2018 and achieved a center-of-mass energy of  $\sqrt{s} = 13$  TeV.  
768    Analysis of data collected in Run 2 is still on going, and is the subject of study in this thesis.

769    Between 2018 and 2022 the LHC underwent the second Long Shutdown (LS2), allowing for  
770    further detector and accelerator maintenance and upgrades. Key improvements to the LHC in-  
771    cluded the improvement of the insulation for over 1200 diode magnets, and the upgrade from  
772    LINAC2 to LINAC4 mentioned in Section 3.1.1. Run 3 of the LHC began in 2022 and achieved a  
773    center-of-mass energy of  $\sqrt{s} = 13.6$  TeV.

774    Run 3 is scheduled to continue through 2026, at which point the LHC machine and detectors  
775    will undergo upgrades for the *high luminosity* LHC (HL-LHC). The HL-LHC will increase the  
776    instantaneous machine luminosity by a factor of 5 - 7.5 with respect to the nominal LHC design.  
777    The bottom panel of Figure 3.4 shows an overview of the preparation work for the HL-LHC that  
778    has been going on concurrently with Run 1, 2, and 3 of the LHC [33].



Figure 3.4: Timeline of LHC and HL-LHC activities [31]. Integrated luminosity estimates are approximate, and not reflective of the exact amount delivered to each experiment.

## Chapter 4: The ATLAS Detector

781 The ATLAS detector (**A** Toroidal **L**H**C** Apparatu**S**) is one of two general purpose physics  
 782 detectors designed to study the products of proton-proton collisions at the LHC. The detector is  
 783 composed of a variety of specialized subsystems, designed to fully capture a wide array of physics  
 784 processes. A diagram of the detector is shown in Figure 4.1. The apparatus is 25m high, 44m in  
 785 length, and weighs over 7000 tons [34]. The LHC beam pipes direct proton beams to an interaction  
 786 point at the center of ATLAS, and the cylindrical detector design captures a complete  $360^\circ$  view  
 787 of the *event*<sup>1</sup>, tracking all particles that result from the collision.

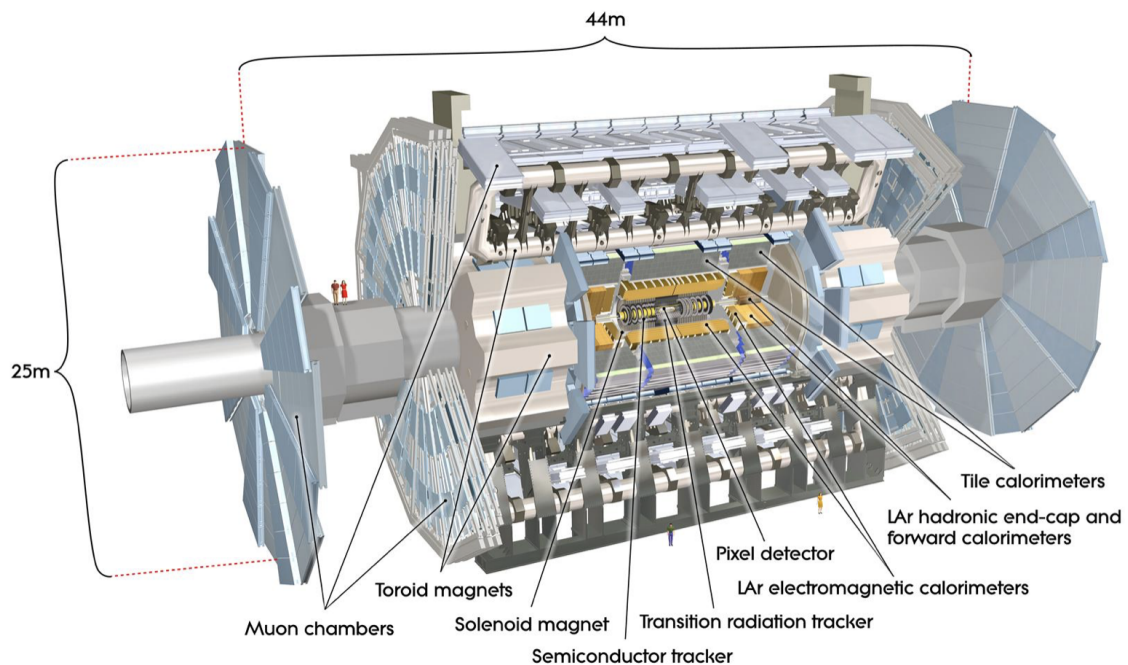


Figure 4.1: The ATLAS detector [34].

---

<sup>1</sup>An ATLAS event is a snapshot of all the measurements associated to a given  $p p$  collision

788 The main components of the ATLAS detector are the Inner Detector (ID) which provides high  
 789 precision tracking of charged particles leaving the collision vertex, the calorimeter system which  
 790 measures the energy of electromagnetic and hadronic objects, and the Muon Spectrometer (MS)  
 791 which gives detailed information about muons that reach the outer radii of the detector. A summary  
 792 of the resolution and angular coverage of each of these systems is presented in Table 4.1. Two  
 793 magnet systems, a 2 T solenoid magnet surrounding the ID, and a 0.5-1.0 T toroid magnet system  
 794 situated throughout the MS, produce magnetic fields which bend the trajectory of charged particles  
 795 traversing the detector. In addition to the main detector components, dedicated forward detectors  
 796 monitor beam conditions and instantaneous luminosity, and an online trigger system reduces the  
 797 data rate to a manageable level for storage. Each of these components will be discussed in further  
 798 detail in this chapter.

<b>Detector component</b>	<b>Required resolution</b>	<b><math>\eta</math> coverage</b>	
		Measurement	Trigger
Tracking	$\sigma_{p_T}/p_T = 0.05\% p_T \oplus 1\%$	$\pm 2.5$	
EM calorimetry	$\sigma_E/E = 10\%/\sqrt{E} \oplus 0.7\%$	$\pm 3.2$	$\pm 2.5$
Hadronic calorimetry (jets)			
barrel and end-cap	$\sigma_E/E = 50\%/\sqrt{E} \oplus 3\%$	$\pm 3.2$	$\pm 3.2$
forward	$\sigma_E/E = 100\%/\sqrt{E} \oplus 10\%$	$3.1 <  \eta  < 4.9$	$3.1 <  \eta  < 4.9$
Muon spectrometer	$\sigma_{p_T}/p_T = 10\% \text{ at } p_T = 1 \text{ TeV}$	$\pm 2.7$	$\pm 2.4$

Table 4.1: General performance goals of the ATLAS detector [34].

## 799 4.1 Coordinate System and Geometry

800 The ATLAS detector employs a right hand cylindrical coordinate system. The  $z$  axis is aligned  
 801 with the beam line, and the  $x - y$  plane sits perpendicular to the beam line. The coordinate system  
 802 origin is centered on the detector, such that the origin corresponds with the interaction point of the  
 803 two colliding beams. The detector geometry is usually characterized by polar coordinates, where  
 804 the azimuthal angle  $\phi$  spans the  $x - y$  plane. The polar angle  $\theta$  represents the angle away from the  
 805 beam line, or  $z$  axis.  $\theta = 0$  aligns with the positive  $z$  axis, and  $\phi = 0$  aligns with the positive  $x$  axis.

806     The polar coordinate  $\theta$  is generally replaced by the Lorentz invariant quantity *rapidity* or  $y$ :

$$y = \frac{1}{2} \ln\left(\frac{E + p_z}{E - p_z}\right). \quad (4.1)$$

807     This substitution is advantageous because objects in the detector are traveling at highly rela-  
808     tivistic speeds. The relativistic speed also means that the masses of the particles are generally small  
809     compared to their total energy. In the limit of zero mass, the rapidity  $y$  reduces to the pseudorapid-  
810     ity  $\eta$ , which can be calculated directly from the polar angle  $\theta$ :

$$\eta = -\ln\left(\frac{\theta}{2}\right). \quad (4.2)$$

811     The distance between physics objects in the detector is generally expressed in terms of the solid  
812     angle between them  $\Delta R$ :

$$\Delta R = \sqrt{\Delta\phi^2 + \Delta\eta^2} \quad (4.3)$$

813     Figure 4.2a depicts the orientation of the coordinate system with respect to the ATLAS detector,  
814     while Figure 4.2b illustrates the relationship between  $\theta$ ,  $\eta$ , and the beamline axis  $z$ . Direct or “head  
815     on” proton-proton collisions are more likely to result in objects whose momentum is directed  
816     along transverse plane (low  $|\eta|$ ); glancing proton-proton collisions are more likely to result in  
817     objects whose momentum is directed along the  $z$ -axis (high  $|\eta|$ ). Due to the difference in the  
818     nature of these collisions, as well as the cylindrical design of the ATLAS detector, the detector  
819     is divided into regions of low and high  $|\eta|$ . Each subsystem has a “central” or “barrel” region  
820     covering low  $|\eta|$ , while the “forward” or “end-cap” regions cover the area up to  $|\eta| = 4.9$ . Each of  
821     the three main ATLAS subsystems will be discussed in the following sections.

## 822     **4.2 Inner Detector**

823     The Inner Detector (ID) is the ATLAS subsystem closest to the interaction point. The primary  
824     purpose of the ID is to determine the charge, momentum, and trajectory of charged particles pass-

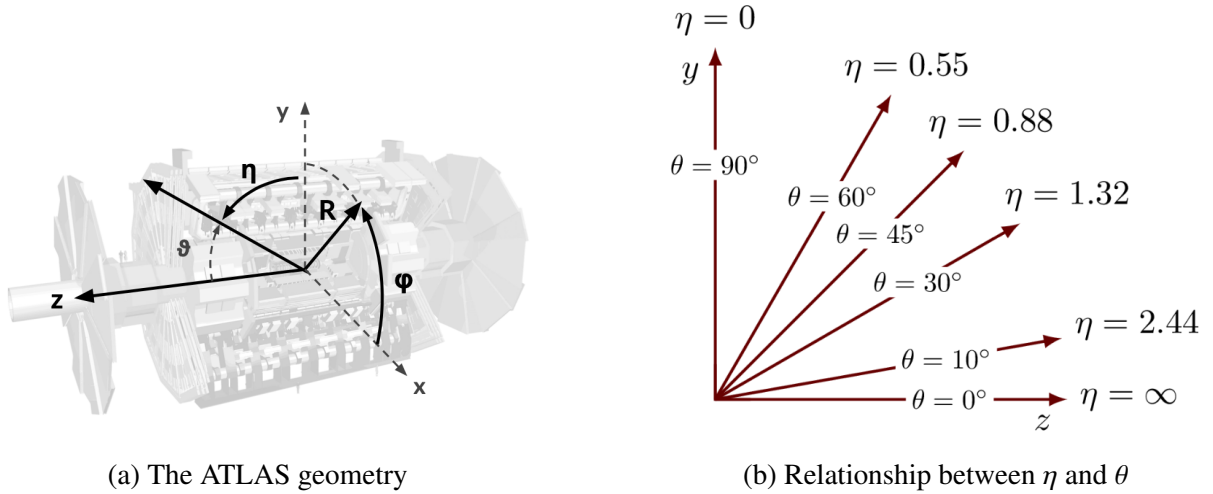


Figure 4.2: ATLAS coordinate system and geometry

825 ing through the detector. With this information the ID is also able to precisely determine interaction  
826 vertices.

827 The ID is composed of three sub-detectors; the Pixel Detector, the Semiconductor Tracker  
828 (SCT) and the Transition Radiation Tracker (TRT) [34]. Figure 4.3 shows the location of these  
829 three subsystems with respect to each other and the interaction point.

#### 830 4.2.1 Pixel Detector

831 The pixel detector is the first detector encountered by particles produced in LHC collisions.  
832 The original pixel detector consists of 3 barrel layers of silicon pixels, positioned at 5 cm, 9 cm  
833 and 12 cm from the beamline. There are also 3 disks on each end-cap positioned 50 - 65 cm  
834 from the interaction point, providing full coverage for  $|\eta| < 2.5$ . Figure 4.4 illustrates the end-cap  
835 geometry for the ID. The layers are comprised of silicon pixels each measuring  $50 \times 400 \mu\text{m}^2$ ,  
836 with 140 million pixels in total. The pixels are organized into modules, which each contain a set  
837 of radiation hard readout electronics chips. In 2014, the Insertable B-layer (IBL) was installed,  
838 creating a new innermost layer of the pixel detector sitting just 3.3 cm from the beamline. The  
839 pixels of the IBL measure 50  $\mu\text{m}$  by 250  $\mu\text{m}$ , and cover a pseudo-rapidity range up to  $|\eta| < 3$ .  
840 The IBL upgrade enhances the pixel detector's ability to reconstruct secondary vertices associated

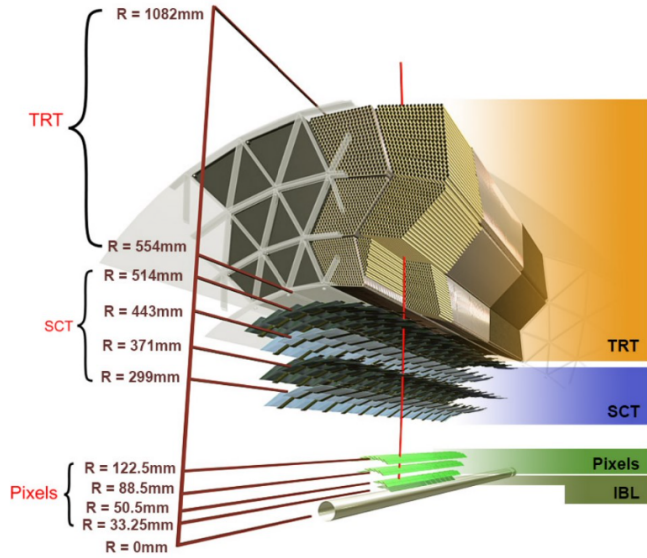


Figure 4.3: A 3D visualization of the structure of the ID in the barrel region [35]

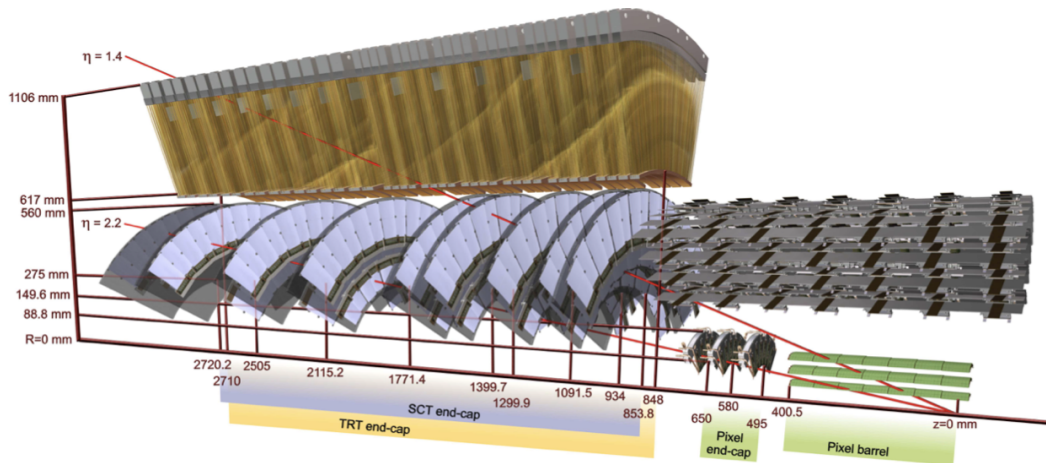


Figure 4.4: A 3D visualization of the structure of the ID end-caps [34]. The paths of two charged particles ( $\eta = 1.4$  and  $2.2$ ) are illustrated.

841 with short-lived particles such as the b-quark. The improved vertex identification also helped  
842 compensate for increasing pile-up in Run 2.

843 **4.2.2 Semiconductor Tracker**

844 The SCT provides at least 4 additional measurements of each charged particle. It employs the  
845 same silicon technology as the Pixel Detector, but utilizes larger silicon strips which measure 80  
846  $\mu\text{m}$  by 12.4 cm. The SCT is composed of 4 barrel layers, located between 30 cm and 52 cm from  
847 the beamline, and 9 end-cap layers on each side. The SCT can distinguish tracks that are separated  
848 by at least 200  $\mu\text{m}$ .

849 **4.2.3 Transition Radiation Tracker**

850 The TRT provides an additional 36 hits per particle track. The detector relies on gas filled  
851 straw tubes, a technology which is intrinsically radiation hard. The straws which are each 4 mm in  
852 diameter and up to 150 cm in length and filled with xenon gas. The detector is composed of about  
853 50,000 barrel region straws and 640,000 end-cap straws, comprising 420,000 electronic readout  
854 channels. Each channel provides a drift time measurement with a spatial resolution of 170  $\mu\text{m}$  per  
855 straw. As charged particles pass through the many layers of the detector, transition radiation is  
856 emitted. The use of two different drift time thresholds allows the detector to distinguish between  
857 tracking hits and transition radiation hits.

858 **4.3 Calorimeters**

859 The ATLAS calorimeter system is responsible for measuring the energy of electromagnetically  
860 interacting and hadronically interacting particles passing through the detector. The calorimeters are  
861 located just outside the central solenoid magnet, which encloses the inner detectors. The calorime-  
862 ters also stop most known particles, which the exception of muons and neutrinos, preventing them  
863 from traveling to the outermost layers of the detector. The ATLAS calorimetry system is composed  
864 of two subsystems - the Liquid Argon (LAr) calorimeter for electromagnetic calorimetry and the

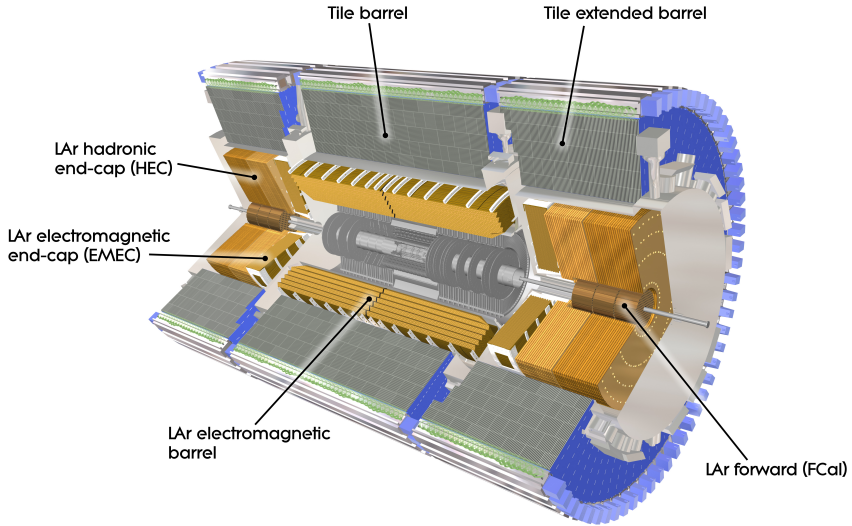


Figure 4.5: ATLAS calorimetry system [36]

865 Tile calorimeter for hadronic calorimetry. The full calorimetry system is shown in Figure 4.5.

#### 866 4.3.1 Liquid Argon Calorimeter

867 The LAr calorimeter is a sampling calorimeter designed to trigger on and measure the ener-  
 868 gies of electromagnetic (EM) particles, as well as hadronic particles in the high  $|\eta|$  regions [37].  
 869 It is divided in several regions, as shown in Figure 4.5. For the region  $|\eta| < 1.4$ , the electro-  
 870 magnetic barrel (EMB) is responsible for EM calorimetry, and provides high resolution energy,  
 871 timing, and position measurements for electrons and photons passing through the detector. The  
 872 electromagnetic end-cap (EMEC) provides additional EM calorimetry up to  $|\eta| < 3.2$ . In the  
 873 region  $1.4 < |\eta| < 3.2$ , the hadronic end-cap (HEC) provides hadronic calorimetry. For hadronic  
 874 calorimetry in the region  $|\eta| < 1.4$ , corresponding to a detector radii  $> 2.2$  m, the less expensive  
 875 tile calorimeter (discussed in the next section) is used instead. A forward calorimeter (FCAL)  
 876 extends the hadronic calorimetry coverage up to  $3.1 < |\eta| < 4.9$ .

877 The LAr calorimeter is composed of liquid argon sandwiched between layers of absorber mate-  
 878 rial and electrodes. Liquid argon is advantageous as a calorimeter active medium due to its natural  
 879 abundance and low cost, chemical stability, radiation tolerance, and linear response over a large

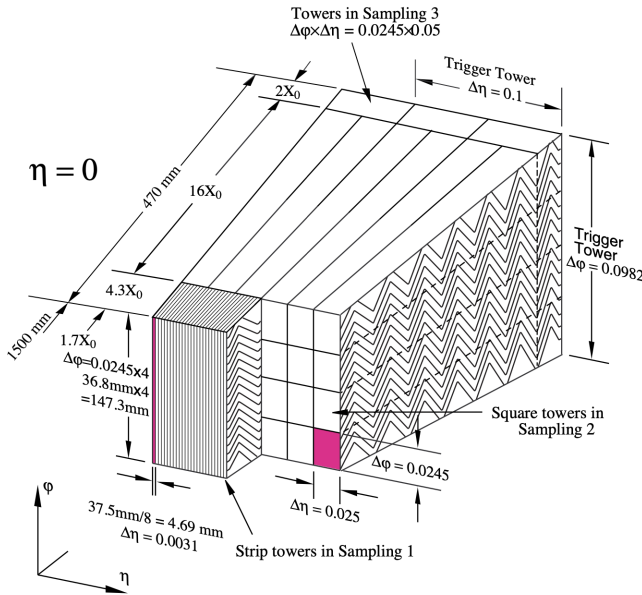


Figure 4.6: Diagram of a segment of the EMB, demonstrating the accordion plate arrangement and the cell segmentation pattern [37]. Three layers are illustrated, and the variation in the cell granularity between the front layer (Sampling Layer 1) and the back layer (Sampling Layer 3) is shown.

880 energy range [38]. The calorimeter is cooled to 87k by three cryostats: one barrel cryostat encom-  
 881 passing the EMB, and two end-cap cryostats. The barrel cryostat also encloses the solenoid which  
 882 produces the 2T magnetic field for the inner detector. Front-end electronics are housed outside the  
 883 cryostats and are used to process, temporarily store, and transfer the calorimeter signals.

#### 884 Electromagnetic Calorimeter

885 For the electromagnetic calorimeters, the layers of electrodes and absorber materials are ar-  
 886 ranged in an accordion shape, as illustrated in Figure 4.6. The detector is divided into  $\eta - \phi$  regions  
 887 or *cells*, which are each read out independently. The The accordion shape ensures that each half  
 888 barrel is continuous in the azimuthal angle, which is a key feature for ensuring consistent high  
 889 resolution measurements. Liquid argon permeates the space between the lead absorber plates, and  
 890 a multilayer copper-polymide readout board runs through the center of the liquid argon filled gap.

891 The detection principle for the LAr calorimeter is the current created by electrons which are

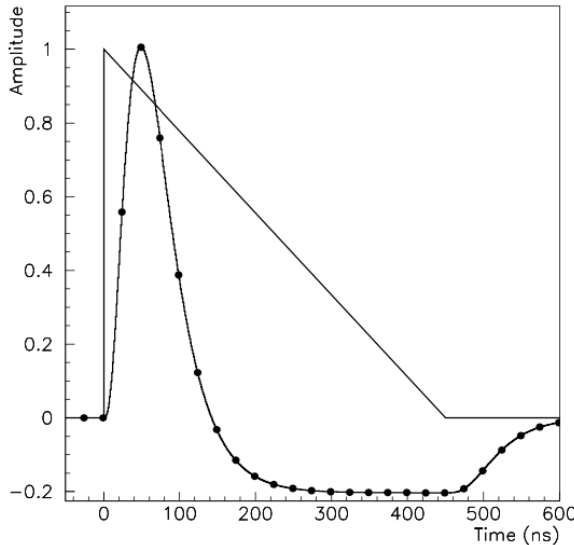


Figure 4.7: A LAr pulse as produced in the detector (triangle) and after shaping (curve) [37]

released when a charged particle ionizes the liquid argon. In the barrel region, the electrons are driven towards the center electrodes by a 2,000 V potential with a drift time of less than 450 ns [39]. In the end-caps the voltage varies as a function of the radius in order to maintain a flat response [37]. The amount of current produced by the ionized electrons is proportional to the energy of the particle creating the signal. Figure 4.7 shows the shape of the signal produced in the LAr calorimeter, before and after it undergoes shaping during the readout process. The shaping of the pulse enforces a positive peak and a negative tail, which ensures that subsequent pulses can be separated with the precision required for the 25 ns LHC bunch spacing.

## Hadronic End-cap Calorimeter

The HEC sits radially beyond the EMEC. The copper absorber plates in the HEC are oriented perpendicular to the beamline, with LAr as the active medium. Each end-cap is divided into two independent wheels; the inner wheel uses 25 mm copper plates, while the outer wheel uses 50 mm plates as a cost saving measure. In each wheel, the 8.5 mm plate gap is crossed by three parallel electrodes, creating an effective drift distance of 1.8 mm. This gap is illustrated in Figure 4.8. Each wheel is divided into 32 wedge-shaped modules, each containing their own set of readout

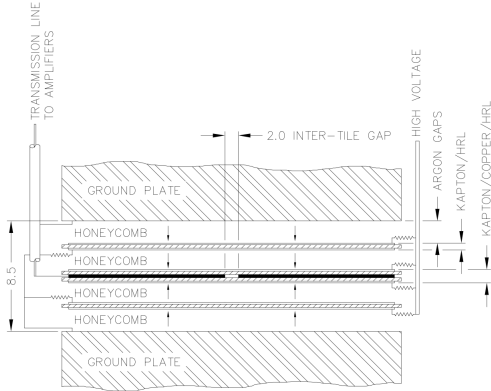


Figure 4.8: Readout gap structure in HEC [37]

907 electronics.

## 908 Forward Calorimeter

909 The forward range ( $3.1 < |\eta| < 4.9$ ) is covered by the FCal, which provides both EM and  
 910 hadronic calorimetry. It is composed of three active cylindrical modules; one EM module with  
 911 copper absorber plates, and two hadronic modules with tungsten absorber plates [37]. The plates  
 912 are oriented perpendicular to the beamline, and LAr is used as the active material throughout. The  
 913 electrodes of the FCal consist of tubes that run parallel to the beam line, arranged in a honeycomb  
 914 pattern. The resulting LAr gaps are as small as  $250 \mu\text{m}$ , which enables the FCal to handle the high  
 915 particle flux in the forward region.

### 916 4.3.2 Tile Calorimeter

917 The Tile Calorimeter (TileCal) provides hadronic calorimetry in the region  $|\eta| < 1.7$ , and sur-  
 918 rounds the LAr calorimeter. It is responsible for measurements of jet energy and jet substructure,  
 919 and also plays an important role in electron isolation and triggering (including muons) [40]. Tile-  
 920 Cal is composed of 3 sections, as shown in Figure 4.5; a barrel calorimeter sits directly outside the  
 921 LAr EMB and provides coverage up to  $|\eta| < 1.0$ . Two extended barrel sections sit outside the LAr  
 922 end-caps and cover the region  $0.8 < |\eta| < 1.7$ .

923 TileCal is a sampling calorimeter composed of steel and plastic scintillator plates as illustrated

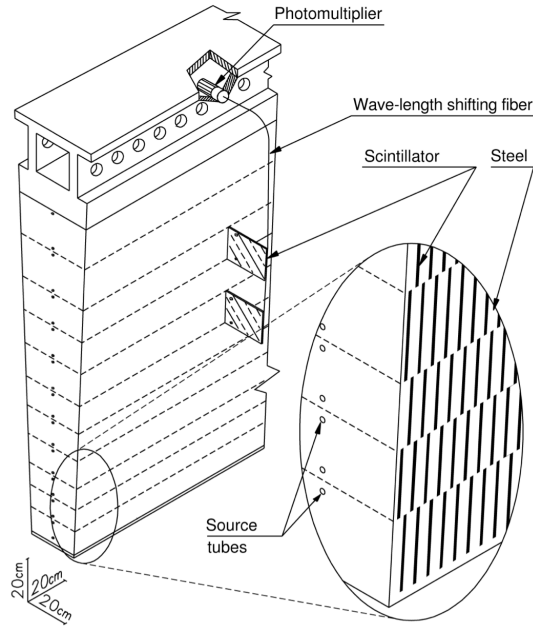


Figure 4.9: TileCal wedge module [40]

in Figure 4.9. A total of 460,000 scintillators are read out by wavelength-shifting fibers. The fibers are gathered to define cells and in turn read out by photomultiplier tubes, which amplify the scintillation light and convert it to an electrical signal. Each cell has an approximate granularity of  $\Delta\eta \times \Delta\phi = 0.1 \times 0.1$ . Each barrel is divided azimuthally into 64 independent modules, an example of which is show in Figure 4.9. The modules are each serviced by front-end electronic housed in a water-cooled drawer on the exterior of the module.

The detection principle of the TileCal is the production of light from hadronic particles interacting with the scintillating tiles. When a hadronic particle hits the steel plate, a shower of particles are produced. The interaction of the shower with the plastic scintillator produces photons, the number and intensity of which are proportional to the original particle's energy.

934

#### 935 4.4 Muon Spectrometer

936 Unlike electrons, photons, and hadrons, muons interact minimally with the ATLAS calorimeters, and can pass through large amounts of detector material without stopping. The ATLAS Muon

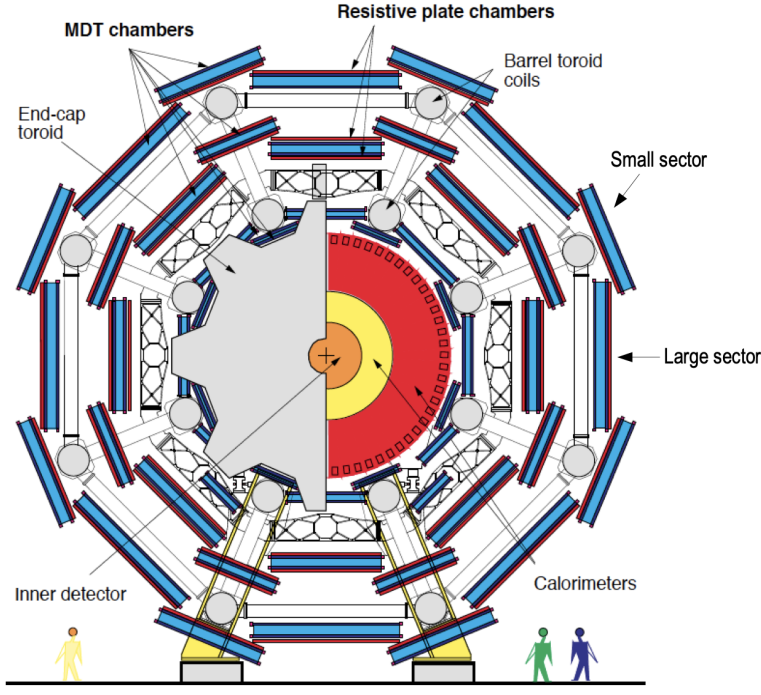


Figure 4.10: Cross section view of the muon spectrometer system [41]

938 Spectrometer (MS) provides additional tracking information to improve the identification and mea-  
 939 surement of muons [41]. The MS comprises the outermost layers of the detector, and is interspersed  
 940 with toroid magnets (discussed in Section 4.5), which provide a magnetic field of approximately  
 941 0.5 T. The magnetic field bends the trajectory of the muons as they pass through the detector, and  
 942 the degree of the bend is directly correlated with the muon momentum. The path of the muon is  
 943 primarily measured by hits in three layers of Monitored Drift Tube (MDT) precision chambers,  
 944 which cover the range  $|\eta| < 2.7$ . The barrel layout of the MS is shown in Figure 4.10.

945 Muon triggering is provided by three layers of Resistive Plate Chambers (RPC) in the barrel  
 946 ( $|\eta| < 1.05$ ), and 3 - 4 layers of Thin Gap Chambers (TGC) in the end-caps ( $1.05 < |\eta| < 2.4$ ).  
 947 RPCs and TGCs also provide muon track measurements in the non-bending coordinate ( $\phi$ ). RPCs  
 948 are constructed from two parallel resistive plates separated by a 2mm gap filled with a sensitive  
 949 gas mixture. This provides a total of six independent measurements for each muon track, with a  
 950 spatial resolution of  $\sim 1$  cm and a time resolution of  $\sim 1$  ns. Time measurements from the RPCs  
 951 are primarily associated to hits in the MDT precision chambers to determine the bunch crossing.

952 The time measurement is also used to reject cosmic muons, and to search for delayed signals.  
953 TCGs provide triggering in the end-cap regions, and consist of parallel 30  $\mu\text{m}$  wires suspended  
954 in a sensitive gas mixture. TCGs provide high radiation tolerance and a fast response time, both  
955 features that are necessary for handling the high flux of muons in the forward region.

956 Precision measurements of muon momentum and position are primarily achieved by MDTs.  
957 The MDTs are constructed from 30 mm diameter tubes, permeated by a gas mixture of 93% Ar  
958 and 7% CO<sub>2</sub> [42]. The average single-tube spatial resolution is 80  $\mu\text{m}$ . Each chamber consists  
959 of six drift tube layers, which together provide a muon track segment resolution of 35  $\mu\text{m}$ . The  
960 momentum of the muons can be calculated from the bend in the muon trajectory as they pass  
961 through the 0.5T magnetic field provided by the toroids. For a  $p_T = 1$  TeV track, the average  
962  $p_T$  resolution is 11%. In the inner most end-cap wheels, Cathode Strip Chambers (CSC) are  
963 used instead of MDTs, covering the region  $2.0 < |\eta| < 2.7$ . CSCs are multi-wire proportional  
964 chambers, with a cathode strip readout. The CSCs have a spatial resolution in the range of 50  $\mu\text{m}$ ,  
965 and a maximum drift time of about 30 ns, which makes them superior for handling the high flux of  
966 particles in the forward region.

## 967 4.5 Magnet System

968 The ATLAS magnet system consists of four sets of superconducting magnets: a barrel solenoid,  
969 a barrel toroid, and two end-cap toroids [43]. The solenoid magnet produces a 2T magnetic field  
970 responsible for bending the trajectories of charged particles as they pass through the inner detector.  
971 The three toroid magnets provide a field of 0.5 - 1 T and curve the path of muons passing through  
972 the muon spectrometer.

973 The inner solenoid magnet is composed of over 9 km of niobium-titanium superconductor  
974 wires, which are embedded into strengthened pure aluminum strips. The solenoid is just 4.5 cm  
975 thick, which minimizes interactions between the magnet material and particles passing through the  
976 detector. It is housed in the LAr cryostat, as described in section 4.3.1, which further reduces the  
977 amount of non-detector material required to support the solenoid. The return yoke of the magnet

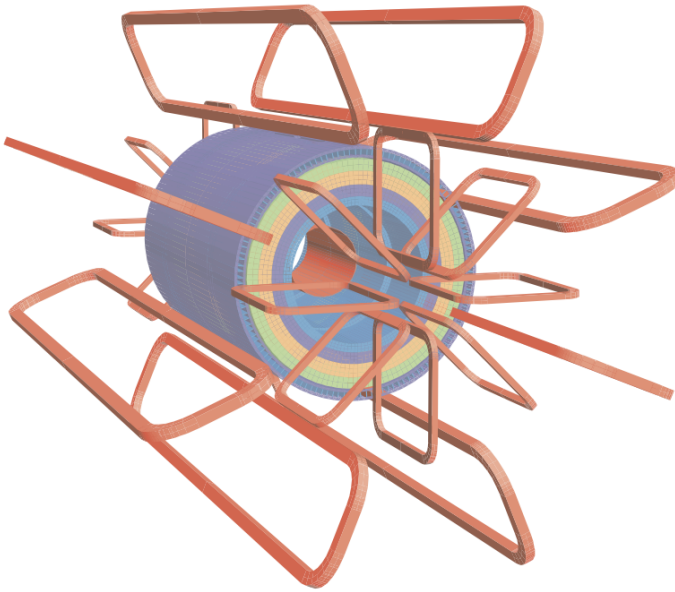


Figure 4.11: Layout of the barrel and end-cap toroid magnets [34]

978 is provided by the iron absorber of the TileCal.

979 The central ATLAS toroid magnet, providing the magnetic field for the barrel region of the  
 980 MS, is the largest toroidal magnet ever constructed at 25.3 m in length [44]. The toroid is com-  
 981 posed of eight individual coils, each housed in their own cryostat. The toroidal magnetic field is  
 982 advantageous as the direction of the field is almost perpendicular to the path of the charged par-  
 983 ticles. 56 km of aluminum stabilized niobium-titanium-copper superconductor wire compose the  
 984 magnet. In each end-cap, eight smaller superconducting coils extend the toroidal magnetic field  
 985 to particles leaving the detector in the forward direction [43]. Figure 4.11 shows the layout of the  
 986 toroid magnets.

## 987 4.6 Forward Detectors

988 In addition to the inner detector, calorimeters, and muon spectrometer, three smaller detectors  
 989 provide coverage in the very forward region. The innermost forward detector, at 17 m from the  
 990 interaction point, is the **L**uminosity measurement using **C**erenkov **I**ntegrating **D**etector (LUCID).  
 991 LUCID's primary purpose is to measure the relative online-luminosity for the ATLAS detector,

992 from inelastic  $p - p$  scattering. The detector is composed of 20 aluminum Cerenkov tubes which  
993 surround the beam pipe and face towards the interaction point.

994 The second forward detector is the Zero-Degree Calorimeter (ZDC), located 140 m from the  
995 interaction point in both directions, at the point where the LHC beam-pipe divides into two separate  
996 pipes. The ZDC's primary purpose is to detect forward neutrons from heavy ion collisions.

997 The third forward detector is the Absolute Luminosity For ATLAS (ALFA) system, located 240  
998 m from the interaction point in both directions. ALFA determines luminosity by measuring elastic  
999 scattering at small angles, from which luminosity can be calculated via the optical theorem. The  
1000 detector is built from scintillating fiber trackers. These are connected to the accelerator vacuum  
1001 via Roman pots, which allow the detector to come as close as 1mm to the beam without disrupting  
1002 the machine vacuum. The LUCID and ALFA detectors are crucial to determining the real-time  
1003 conditions of the beams and the total luminosity delivered to the ATLAS detector [34].

## 1004 **4.7 Trigger and Data Acquisition**

1005 The trigger and Data Acquisition systems (TDAQ) are responsible for selecting the most inter-  
1006 esting events to save for further downstream processing. Because of the high luminosities delivered  
1007 to the ATLAS detector, not all events recorded can be saved; the 40 MHz bunch crossing rate must  
1008 be reduced by 5 orders of magnitude to an event storage rate of  $\sim 1$  kHz. The trigger system is  
1009 composed of three distinct levels: Level 1 (L1), Level 2 (L2) and the event filter [34]. Collectively  
1010 the L2 trigger and the event filter form the High Level Trigger (HLT).

1011 The L1 trigger is implemented in the hardware of the ATLAS calorimeter and muon systems.  
1012 A block diagram of the L1 trigger is available in Figure 4.12. The primary modality of the L1 trig-  
1013 ger is to identify muons, electrons, photons, jets, and  $\tau$ -leptons with high transverse momentum.  
1014 Particles with high transverse momentum are more likely to originate from direct, high energy  
1015 collisions, which are most likely to produce interesting physics processes. The L1 trigger also  
1016 identifies events with large missing transverse energy, which could be indicative of new physics.  
1017 The L1 muon trigger (L1Muon) relies on RPC and TGC trigger chambers in the barrel and end-

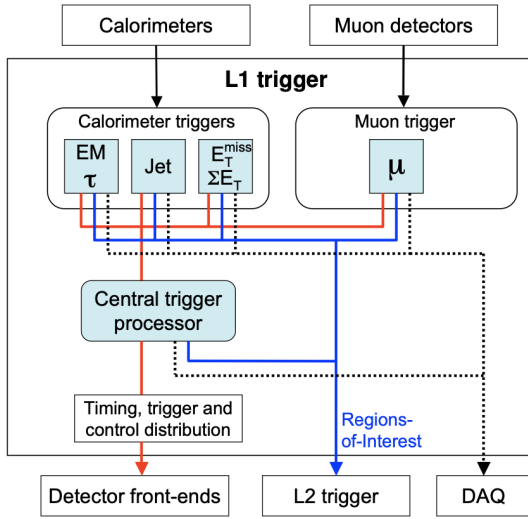


Figure 4.12: Block diagram of the L1 trigger process [34]. The overall L1 trigger decision is made by the CTP.

1018 cap regions of the muon spectrometer. The L1 Calorimeter Trigger (L1Calo) uses reduced gran-  
 1019 ularity information collected by all the calorimeter subsystems. Results from the L1Muon and  
 1020 L1Calo triggers are combined by the Central Trigger Processor (CTP), which implements a trigger  
 1021 ‘menu’, listing various combinations of trigger requirements. The maximum L1 acceptance rate  
 1022 is 100 kHz, and the L1 trigger decision must reach the front-end electronics within 2.5  $\mu$ s of its  
 1023 associated bunch-crossing.

1024 The L1 trigger defines a Region-of-Interest (RoI) for each passing event. The ROI is repre-  
 1025 sented by the  $\eta$ - $\phi$  detector region where interesting features were identified by the L1 selection  
 1026 process. Information about the type of feature identified and the threshold which was exceeded to  
 1027 trigger the L1 response is also recorded. The ROI data is sent to the L2 trigger, which uses all of  
 1028 the available information within the ROI at full granularity and precision. The L2 trigger reduces  
 1029 the event rate from 100 kHz to 3.5 kHz, with an average processing time of 40 ms. The final stage  
 1030 of the HLT is the event filter, which reduces the event rate to 200 Hz (<1 kHz). The event filter uses  
 1031 an offline analysis process to select fully rebuilt events which will be saved for further analysis. A  
 1032 diagram of the full ATLAS TDAQ system is shown in Figure 4.13.

1033 All levels of the ATLAS trigger system depend on specialized electronics. Each detector front-

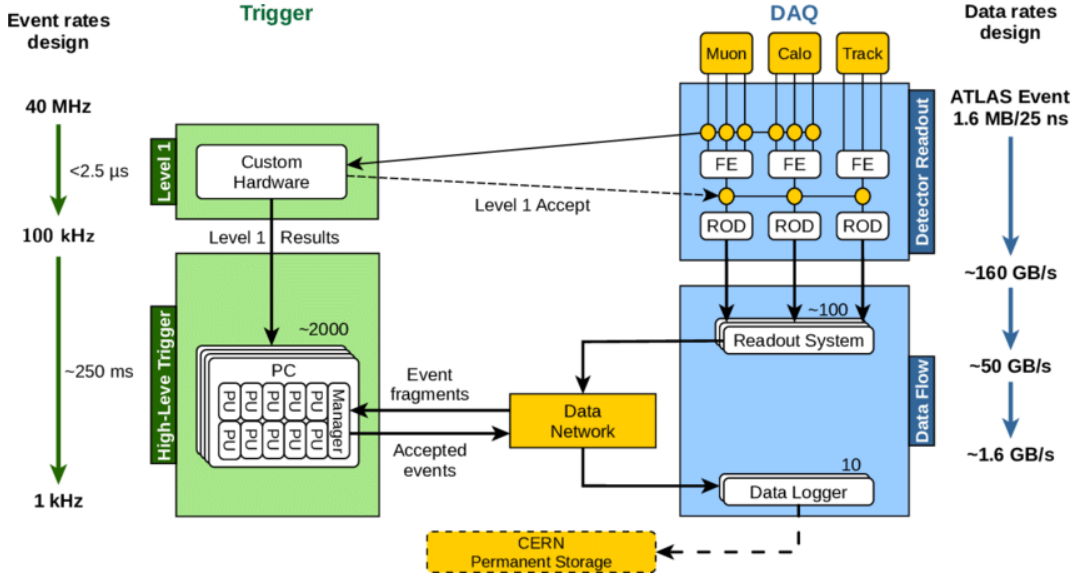


Figure 4.13: Block diagram of the trigger and data acquisition processes, including L1 and HLT processes [45].

1034 end system has a specialized Readout Driver (ROD) which collects information from several front-  
 1035 end data streams at once. The ROD is composed of front-end analogue processing, a L1 buffer  
 1036 which retains the information long enough for the L1 trigger decision, and dedicated links which  
 1037 send the front-end L1 triggered data to Data Acquisition System (DAQ). Any digital signals are  
 1038 formatted as raw data before being transferred to the DAQ. The first stage of the DAQ temporarily  
 1039 stores the L1 data in local buffers. The ROI data is then requested by the L2 trigger, after which  
 1040 selected events are transferred to an event building system, before events passing the event filter  
 1041 are sent to the CERN computer center for permanent storage. The DAQ system not only allows  
 1042 for the readout of detector data, but is also responsible for the monitoring and configuration of  
 1043 the hardware and software components which make up the data readout system via the Detector  
 1044 Control System (DCS).

1045 The DCS allows centralized control of all detector subsystems simultaneously. It continually  
 1046 monitors operational conditions, reports any abnormal behavior to the operator, and can perform  
 1047 both automatic and manual interventions. The DCS reports on real time detector conditions such  
 1048 as high or low voltage detector electronics, gas and cooling systems, magnetic field conditions,  
 1049 humidity and temperature. This information is continually monitored by experts in the ATLAS

1050 control room, so that action can be taken immediately to correct any issues that arise. The DCS also  
1051 handles communication between detector systems, and other systems such as the LHC accelerator,  
1052 the ATLAS magnets, and CERN technical services [34].

1053

1054

## Chapter 5: Particle Reconstruction and Identification

1055 With a design luminosity of  $1.0 \times 10^{34} \text{ cm}^{-2}\text{s}^{-1}$ , and a peak Run 2 instantaneous luminosity of  
1056  $2.0 \times 10^{34} \text{ cm}^{-2}\text{s}^{-1}$ , reconstructing and identifying the products of LHC  $p p$  collisions is one of the  
1057 most complex tasks for each LHC experiment. The accurate reconstruction and identification of  
1058 *physics objects*<sup>1</sup> lays the ground work for all subsequent physics analyses, so it is also one of the  
1059 most fundamentally important tasks performed by an experiment.

1060 Reconstruction is the process of combining raw and uncalibrated hits across various subsystems  
1061 into unique objects. Two particular subsystems, the Inner Detector (ID) tracker and the calorime-  
1062 ters play particularly important roles and will be discussed in detail. Analysis of the properties of  
1063 the reconstructed objects identifies them as photon, electrons, muons, or jets. While photons, elec-  
1064 trons, and muons are fundamental particles, jets represent a collimated shower of many hadronic  
1065 particles, whose definition is more flexible. Jet reconstruction, clustering and track association are  
1066 all of particular import to jet identification, and to the later content of this thesis. Finally, recon-  
1067 struction also identifies *missing transverse energy*  $E_T^{\text{miss}}$  in events, which is a crucial variable for  
1068 BSM physics searches. Figure 5.1 shows how the physics objects listed here interact with various  
1069 systems in the ATLAS detector.

1070 **5.1 Inner Detector Tracks**

1071 As the inner most layer of the detector, the ID measures charged particles close to the interac-  
1072 tion point. The various hits of these charged particles throughout the ID are used to reconstruct  
1073 *tracks* which give the trajectories of charged particles [47]. Track reconstruction begins by clus-  
1074 tering hits in the Pixel and SCT detectors, and combining clusters from different radial layers of

---

<sup>1</sup>A particle which has appeared in the ATLAS detector and whose properties have been estimated via the measurements left in various detector subsystems.

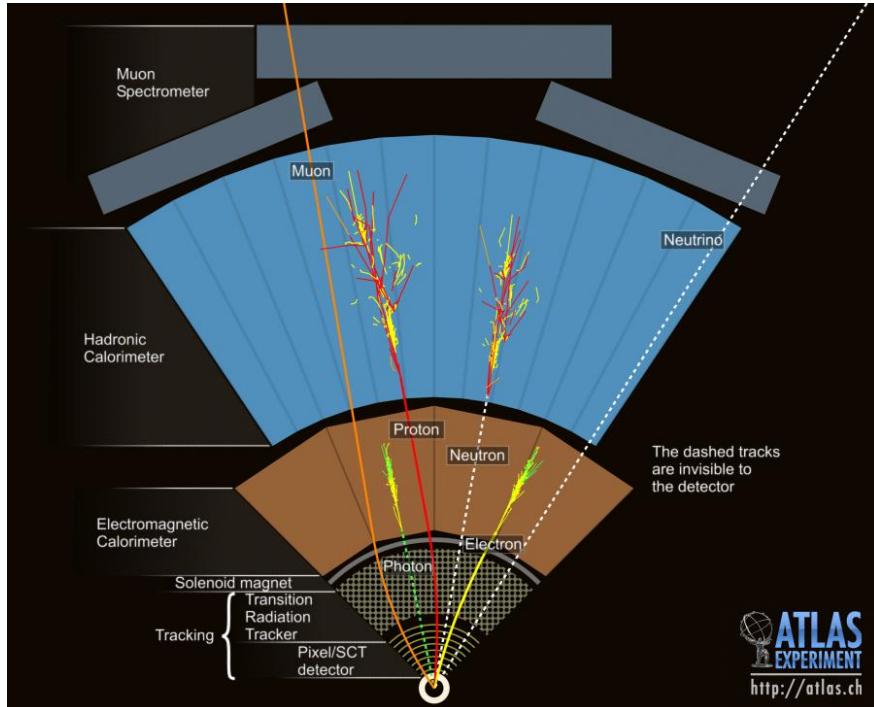


Figure 5.1: This graphic illustrates a slice of ATLAS detector barrel [46]. A photon, electron, and two jets (associated to the proton and neutron) are shown, illustrating each object's interaction with various ATLAS subsystems. The path of the charged particles is curved on account of the strong magnetic field produced by the solenoid and toroid magnets. A neutrino, generally representing the reconstruction of missing transverse energy, is also illustrated.

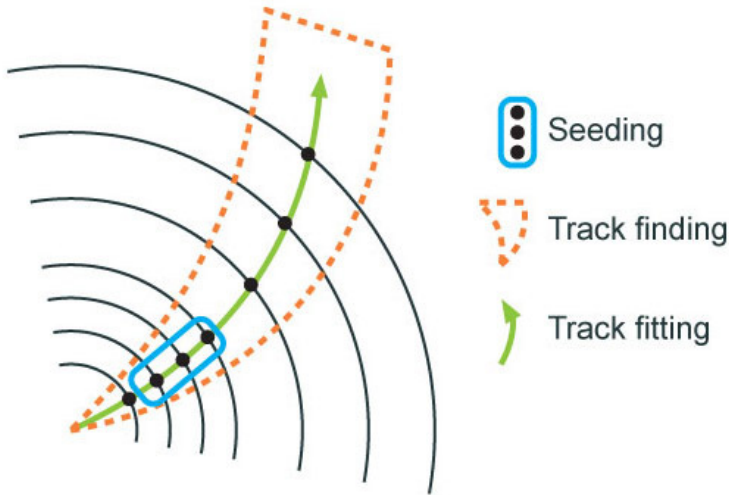


Figure 5.2: Track reconstruction seeding, finding and fitting illustration [47]

1075 these detectors. The multi-layer clusters form track *seeds*, which provide initial estimates of mea-  
 1076 surements belonging to an individual track. The requirement of three points allows for a rough  
 1077 estimate of the track  $p_T$  to be made by calculating the curvature of the track and accounting of the  
 1078 magnetic field in the ID.

1079 Track seeds are subject to a variety of quality requirements, such as having a minimum esti-  
 1080 mated  $p_T$  and passing interaction region compatibility criterion. If these requirements are satisfied,  
 1081 the track seeds are passed to the track finding and fitting algorithms. The interplay of these three  
 1082 track reconstruction steps is illustrated in Figure 5.2.

## 1083 5.2 Photons and Electrons

1084 Photons and electrons shower in the LAr calorimeter, and are identified by the energy deposits  
 1085 they leave there. Energy deposits in a collection of nearby cells are termed *proto-clusters*, which  
 1086 become the starting point for electron and photon reconstruction [48]. The clustering algorithm  
 1087 begins when the energy deposit in a certain cell exceeds the noise threshold with a significance  
 1088 of  $4\sigma$ . The algorithm then collects neighboring cells which have an energy deposit exceeding the  
 1089 noise threshold with a significance of  $2\sigma$ , creating a *topo-cluster*<sup>2</sup>. Next, these topo-clusters are

---

<sup>2</sup>A topological grouping of neighboring calorimeter cells based on their energy deposits

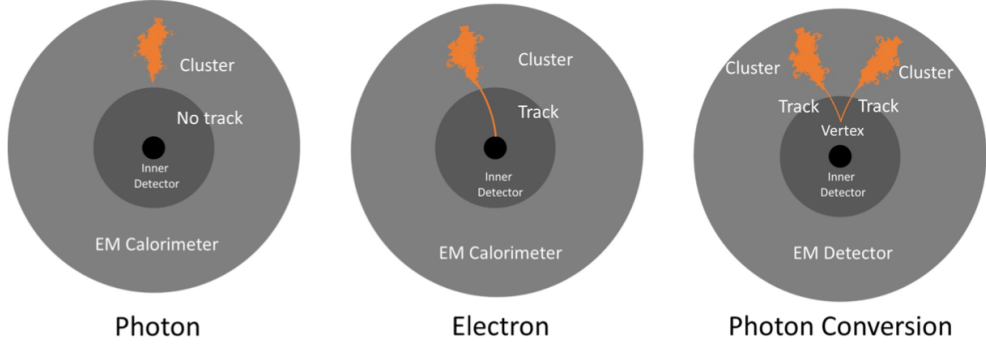


Figure 5.3: Three types of EM object candidates [49].

1090 matched to ID tracks, created as described in Section 5.1. The location of the topo-cluster defines  
 1091 a region of interest (ROI) in the ID, where additional modified track reconstruction algorithms are  
 1092 run in the case that no associated tracks are found. Any ID tracks associated to the topo-cluster  
 1093 are retrofitted to allow for additional energy loss due to bremsstrahlung. A converted photon track  
 1094 reconstruction algorithm is run to check for tracks coming from secondary vertices consistent with  
 1095 converted photons. The secondary vertices are constructed from two oppositely charged tracks  
 1096 consistent with a massless particle, or from one track without any hits in the innermost layer of the  
 1097 ID.

1098 For electron identification, the EM cluster is required to match ID tracks that originate from  
 1099 the primary vertex at the interaction point. For photon identification, the EM cluster can either be  
 1100 matched to tracks coming from a secondary vertex (converted photon), or matched to no tracks  
 1101 (unconverted photon). Figure 5.3 illustrates these three cases for EM object identification.

1102 *Superclusters* are built separately for photons and electrons, based on the combined topo-cluster  
 1103 and ID track information. First, the EM topo-clusters are tested to see if they meet the minimum  
 1104 requirements to become electron or photon seed clusters. For electrons, the cluster must have a  
 1105 minimum  $E_T$  of 1 GeV, and must be matched to a track with at least 4 hits in the silicon tracking  
 1106 detectors. For photons, the cluster must have an  $E_T$  greater than 1.5 GeV. If the seed cluster require-  
 1107 ments are met, the algorithm searches for satellite clusters, which can arise from bremsstrahlung  
 1108 radiation. If the satellite clusters pass the positional, energy and tracking requirements to be asso-

1109 ciated with the proto-cluster, they are combined into a supercluster.

1110 Electron and photon objects are identified from the superclusters after the energy calibration  
1111 is applied, which accounts for the energy resolution of each subdetector measurement. Because  
1112 photon and electron superclusters are built independently, some clusters can produce both a photon  
1113 and an electron. In this case an ambiguity resolution procedure is applied to determine if the  
1114 supercluster can be easily identified as only a photon (no tracks present) or only an electron (good  
1115 tracks pointing to the primary vertex). In some cases, the identity of the cluster is still ambiguous,  
1116 in which case both a photon and electron object are created for analysis and flagged as ambiguous.  
1117 Energy, shower shape, and other analysis variables are calculated from the supercluster and saved  
1118 with the electron or photon object.

### 1119 5.3 Muons

1120 Muons are identified through the tracks and energy deposits they leave in the ID, calorimeters,  
1121 and Muon Spectrometer (MS). Muons experience minimum ionizing loss, meaning they do not  
1122 deposit much of their energy in the calorimeters (recall Figure 5.1), and therefore reach the outer  
1123 regions of the detector where the MS is housed. Muon identification begins in the Muon Drift  
1124 Tube chambers by performing a straight line fit between the hits found in each layer, creating  
1125 *segments*. Segments in the middle layers are then used as seeds for the track building algorithm,  
1126 which searches for compatible combinations of segments based on their relative positions and  
1127 angles [50]. A  $\chi^2$  fit is performed on each track candidate. Based on the  $\chi^2$  criteria, hits are  
1128 removed or added such that the track contains as many hits as possible while satisfying the fit  
1129 criteria.

1130 The MS track candidates are combined with track information from the ID and calorimeters  
1131 according to various algorithms based on the information available from each subdetector. Four  
1132 different types of muons arise from the various reconstruction algorithms:

- 1133 • Combined muon: a muon track identified through independent track reconstruction in the  
1134 ID and MS, where the combined track is formed using a global refit that uses hit information

1135 from both detectors. Most muons are constructed through an outside-in procedure, in which  
1136 a muon track candidate is identified in the MS and then an associated track is found in the ID.  
1137 A complementary inside-out procedure is also implemented and identifies additional muons.

- 1138 • Segment-tagged muon: an ID track is identified as a muon if when extrapolated out to the  
1139 MS (following the inside-out global fit procedure) it is matched to at least one local MS  
1140 segment.
- 1141 • Calorimeter-tagged muon: an ID track is identified as a muon if it is matched to a calorimeter  
1142 energy deposit that is compatible with a minimum-ionizing particle. This muon identifica-  
1143 tion has the lowest purity, but it used in regions where the MS has only partial coverage due  
1144 to cabling and service access routes.
- 1145 • Extrapolated muons: the muon is reconstruction only from the MS track and a requirement  
1146 on compatibility with the primary interaction point. The muon track is required to cross at  
1147 least two layers of the MS, and three layers in the forward region. These muons are mainly  
1148 used to extend muon acceptance into the region  $2.5 < |\eta| < 2.7$  where ID track information  
1149 is not available.

1150 Figure 5.4 illustrates the four types of muon reconstruction. Overlap between reconstructed  
1151 muons using ID tracks is resolved by giving preference to combined muons, then segment tagged  
1152 muons, and finally calorimeter tagged muons. Overlap with extrapolated muons is resolved by  
1153 giving preference to the muon with a better fit quality and higher number of tracks.

1154 All muon track candidates are required to pass a series of quality selections to be identified in  
1155 the final muon collection. The primary qualities considered are the  $\chi^2$  goodness of fit for the global  
1156 track, the difference in  $p_T$  measurement between the ID and MS tracks, and the ratio between the  
1157 charge and momentum of the tracks. The quality requirements help reject hadrons, primarily from  
1158 kaon and pion decays. Muons candidates consistent with cosmic rays are also rejected.

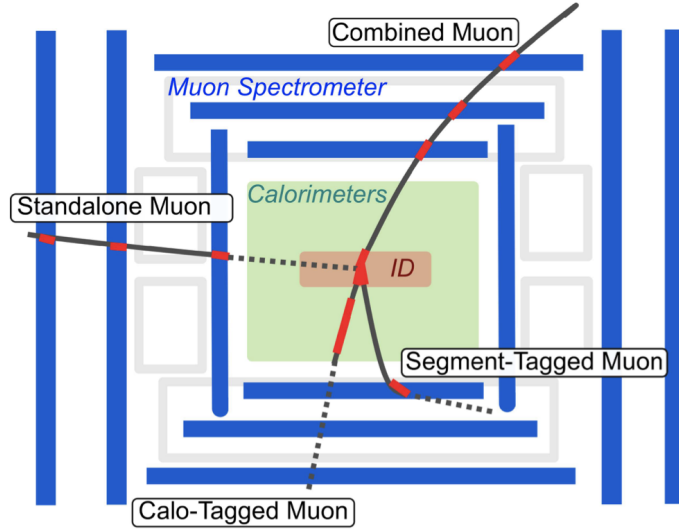


Figure 5.4: The four types of muon track candidates [51]. The red bands indicate where detector measurements for each muon track candidate are made. The dashed lines indicate the path of the muon through detectors where no measurement is made. Standalone muon is another term for an extrapolated muon.

## 1159 5.4 Jets

1160 The protons accelerated in the LHC are composed of quarks and gluons, and thus their colli-  
 1161 sions often result in the release of energetic quarks and gluons, collectively termed *partons*. The  
 1162 energetic partons can radiate additional gluons, and these gluons can pair produce quarks in a pro-  
 1163 cess called *fragmentation*. Fragmentation continues until the energy drops sufficiently that color  
 1164 conservation plays a dominant role. At that point, additional quarks and gluons are produced from  
 1165 vacuum to create neutral color states for the fragmented collection of partons. This process is  
 1166 known as *hadronization* [52]. The hadronized partons compose a collimated stream of particles,  
 1167 known as a *jet*, which is then observed in the detector. The full process that produces jets is known  
 1168 as a *parton shower*, and is illustrated in Figure 5.5.

1169 Jets are identified by the energy deposits they leave in the calorimeter, which are then matched  
 1170 to the tracks they leave in the ID. Jet reconstruction generally begins in the calorimeters, with  
 1171 the identification of *topo-clusters*. Then jet reconstruction algorithms combine calorimeter infor-  
 1172 mation with tracking information. There are a variety of jet collections depending on the exact

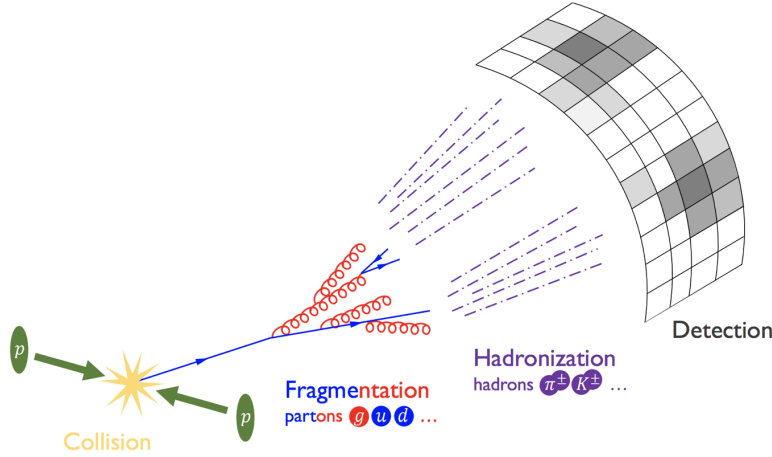


Figure 5.5: The fragmentation and hadronization processes undergone by a quark produced in a proton-proton collision [53].

1173 usage of calorimeter and tracking information in the reconstruction. Some common collections  
 1174 include particle flow jets (PFlow), track calo-cluster jets (TCC), EM topo-cluster jets (EMTopo),  
 1175 and unified flow object jets (UFO). Only particle flow jets will be discussed in greater detail due to  
 1176 their importance in this analysis. The following sections discuss jet identification in the calorime-  
 1177 ters, particle flow jet construction using the *anti- $k_t$  algorithm*, jet clustering and jet substructure  
 1178 characteristics.

#### 1179 5.4.1 Calorimeter Clusters

1180 Jets are first identified by the energy deposits they leave in the calorimeters. As for photons  
 1181 and electrons, the reconstruction of jets in ATLAS begins with the construction of topo-clusters,  
 1182 which are topologically-grouped noise-suppressed clusters of calorimeter cells [54]. The topo-  
 1183 cluster seed is a cell with an energy that exceeds the noise threshold for the cell with a significance  
 1184 of at least  $4\sigma$ . Any cells adjacent to the seed cell in three dimensions are added to the cluster if  
 1185 they have an energy deposit of at least  $2\sigma$ . This process is repeated, growing the cluster, until no  
 1186 adjacent cells exceeding the energy deposit threshold remain. As a final step, all adjacent cells are  
 1187 added to the topo-cluster, irrespective of their energy.

1188 The construction process for topo-clusters allows for the possibility that several independent

signatures are grouped into one topo-cluster. To correct for this, the topo-cluster is scanned for local maxima, defined by any cell with energy  $> 500$  MeV, and no neighboring cells with greater energy. If more than one local maximum is identified, the topo-cluster is split among the corresponding energy peaks [55]. In the event that one cell neighbors two or more local maxima, the cell is assigned to the two highest-energy clusters that it neighbors. This means each cell is shared at most once, between at most two post-splitting topo-clusters.

Two measurements for the total energy of the topo-cluster are considered. The raw, or electromagnetic (EM), scale simply considers the sum of energy from all cells in the topo-cluster. The local cell weighting (LCW) scale first classifies clusters as electromagnetic or hadronic, and then applies appropriate corrections for hadronic interactions in the jet energy calculation [54]. The corrections are derived from Monte Carlo simulations, and account for the weaker response of ATLAS calorimeters to hadronic interactions (ATLAS calorimeters are *non-compensating*<sup>3</sup>), and hadronic energy losses due to interactions with dead material [55].

#### 5.4.2 Particle Flow Algorithm

The calorimeters provide excellent jet energy resolution for high energy jets. However, the granularity of the hadronic calorimeter is restricted to  $0.1 \times 0.1$  in  $\eta \times \phi$ . Combining the information from the calorimeter with tracking information provides superior angular resolution and energy resolution. The particle flow (PFlow) algorithm is one of a handful of algorithms which can perform this task.

An overview of the process is given in Figure 5.6. Tracks from the ID which are selected for the PFlow algorithm are required to have at least 9 hits in the silicon detector, and missing pixel hits in places where a hit would be expected. Additionally, the tracks have  $p_T > 0.5$  GeV, and  $|\eta| < 2.5$ . The algorithm then attempts to match these tracks to EM scale calorimeter topo-clusters. This matching is performed using the distance metric

---

<sup>3</sup>The response of ATLAS calorimeters is different for EM showers and hadronic showers, since the calorimeter response to hadronic showers is energy dependent

$$\Delta R' = \sqrt{(\frac{\Delta\phi}{\sigma_\phi})^2 + (\frac{\Delta\eta}{\sigma_\eta})^2} \quad (5.1)$$

1213 where  $\sigma_\eta$  and  $\sigma_\phi$  represent the angular widths of the topo-clusters, and  $\Delta\eta$  and  $\Delta\phi$  represent  
 1214 the distance between the track (extrapolated to the second layer of the EM calorimeter) and the  
 1215 barycenter of the topo-cluster [56]. The topo-cluster closest to the track as measured by  $\Delta R'$  is  
 1216 considered matched to the track. If no topo-cluster is found within the cone size of  $\Delta R' = 1.64$ , it  
 1217 is assumed that particle which left the track did not form a topo-cluster in the calorimeter.

1218 The PFlow algorithm predicts the expected single topo-cluster energy for a given track, based  
 1219 on the track momentum and topo-cluster position. This value is then compared to the observed  
 1220 energy of the topo-cluster, and the probability that the particle energy was deposited in more than  
 1221 one topo-cluster is evaluated. If necessary, the algorithm adds more topo-clusters to the track/topo-  
 1222 cluster system, in order to account of the full shower energy of the track particle.

1223 To reduce the impact of double counting the energy of a given particle by including both its  
 1224 tracker and calorimeter energy measurements, the calorimeter energy measurements associated to a  
 1225 given track are subtracted from the total calorimeter measurement. If the expected energy deposited  
 1226 by the particle exceeds the topo-cluster energy, the full topo-cluster is removed. If the expected  
 1227 energy is less than the EM scale energy of all the considered topo-clusters, topo-cluster cells are  
 1228 removed one by one, until the full expected energy deposit of the particle has been removed from  
 1229 the calorimeter information. The resulting set of tracks and topo-clusters represent the event with  
 1230 no double-counting of energy between subdetectors [56]. This information is passed to the jet-  
 1231 finding algorithm.

### 1232 5.4.3 Jet Clustering

1233 When a parton decays in the detector, its energy deposits often result in multiple calorimeter  
 1234 clusters. For physics purposes, it is useful to combine clusters that likely resulted from an individ-  
 1235 ual parton decay, in order to reconstruct the parton. The process of grouping topo-clusters which  
 1236 were produced by the same parton decay is *jet clustering*.

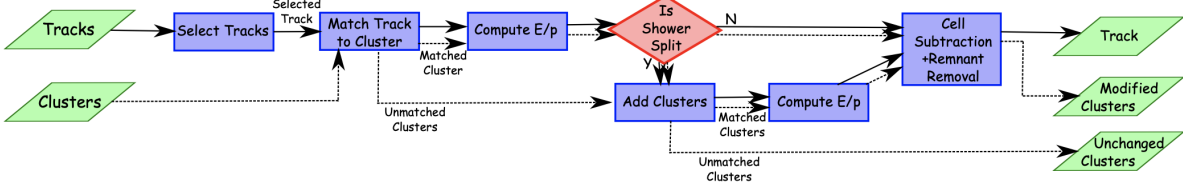


Figure 5.6: A flow chart illustrating the particle flow algorithm progression [56]. The solid lines indicate the progression of tracks through the algorithm, while the dotted lines indicate the progression of clusters. The process begins with track selection and continues until the energy associated with the tracks has been removed from the calorimeter. At the end charged particle tracks, unmodified topo-clusters, and the remnants of topo-clusters which have had part of their energy removed remain.

1237     The anti- $k_t$  algorithm [57] as provided by the FastJet library [58] is most commonly used for  
 1238     jet clustering in the ATLAS experiment, with varying reconstruction radius settings. The anti-  
 1239      $k_t$  algorithm is based on sequential recombination algorithms [59]. A sequential recombination  
 1240     considers the distance  $d_{ij}$  between objects  $i$  and  $j$  (particles or pseudojets), and the distance  $d_{iB}$   
 1241     between an object  $i$  and the beam line  $B$ . If  $d_{ij}$  between two objects is the smallest distance among  
 1242     those considered,  $i$  and  $j$  are combined into a pseudojet. The process continues until the smallest  
 1243     distance is  $d_{iB}$  at which point the object  $i$  is determined to be a jet and removed from the objects in  
 1244     consideration. The procedure is repeated with the remaining objects until there are none remaining  
 1245     [57].

1246     The anti- $k_t$  algorithm adopts this procedure, but modifies the distance measurements  $d_{ij}$  and  
 1247      $d_{iB}$  to consider the transverse momentum  $k_t$ :

$$d_{ij} = \min(k_{ti}^{2p}, k_{tj}^{2p}) \frac{\Delta_{ij}^2}{R^2}, \quad (5.2a)$$

$$d_{iB} = k_{ti}^{2p}. \quad (5.2b)$$

1248     The addition of the term  $p$  allows adjustments to algorithm which govern the relative power of  
 1249     the momentum versus the geometrical scale  $\Delta_{i,j}$ , which is defined as  $\Delta_{i,j} = (y_i - y_j)^2 + (\phi_i - \phi_j)^2$   
 1250     where  $y_i$  and  $\phi_i$  are respectively the rapidity and azimuth of particle  $i$  [57]. The radius parameter

1251  $R$  is chosen and determines the geometric cone size [59].

1252 In the case  $p = 1$  the inclusive  $k_t$  algorithm [59] is recovered, which is a standard sequential  
 1253 combination jet clustering algorithm. In the case  $p = 0$ , the Cambridge/Aachen sequential combi-  
 1254 nation algorithm [60] is recovered. The case  $p = -1$  gives rise to the anti- $k_t$  algorithm. The impact  
 1255 of this choice means that the distance  $d_{ij}$  between many soft particles is larger than between soft  
 1256 and hard particles. Therefore, soft particles tend to cluster with hard ones before they cluster with  
 1257 other soft particles. They key feature of this behavior is that soft particles do not modify the shape  
 1258 of the jets. This leads to the creation of circular conical jets, a desirable feature which sequen-  
 1259 tial combination algorithms and cone algorithms struggle to achieve. Figure 5.7 compares anti- $k_t$   
 1260 jet formation with the inclusive  $k_t$  and Cambridge/Aachen algorithms mentioned here, as well as  
 1261 the SIScone algorithm [61], which checks for sets of stable cones compatible with the observed  
 1262 radiation.

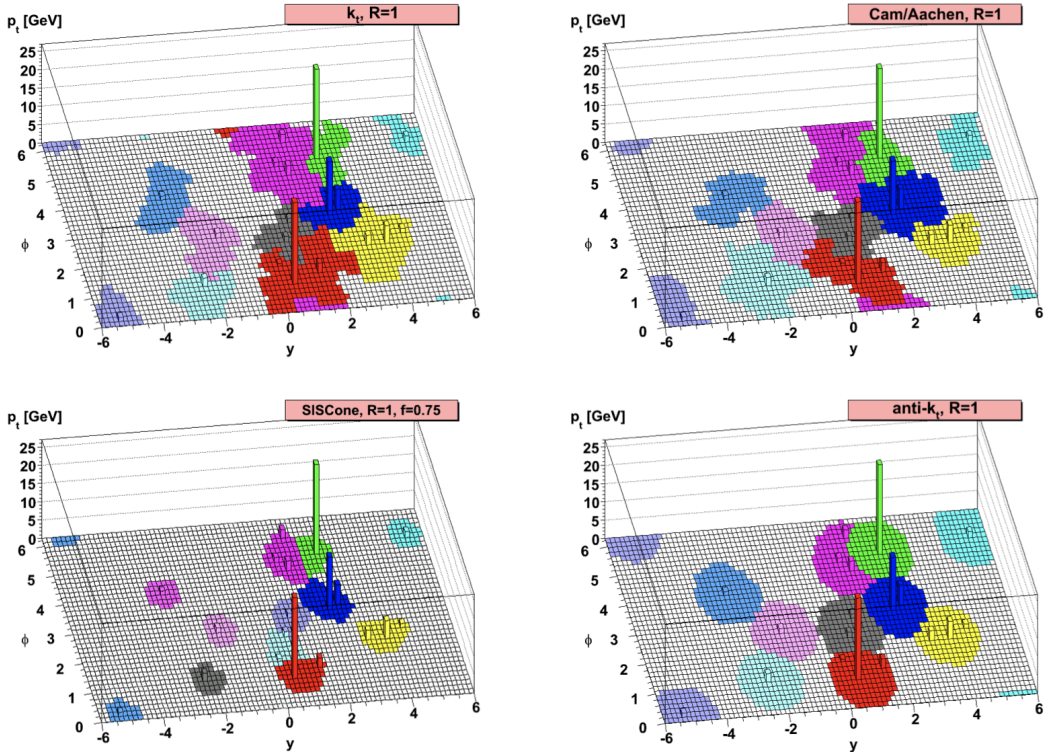


Figure 5.7: A comparison of jet clustering with four different jet algorithms. The anti- $k_t$  algorithm is observed to create the most conical jets, where the shape of the jet is immune to the presence of soft radiation [57].

1263 Any useful jet clustering algorithm must satisfy the requirements of infrared safety and collinear  
1264 (IRC) safety. Infrared safety implies that the resulting set of jets is unaltered by the presence of  
1265 additional soft particles in the list of seed clusters. As explained above, the anti- $k_t$  algorithm  
1266 is naturally infrared safe. Collinear safety requires that the final set of jets is not impacted by  
1267 collinear splitting of one of the jets. If the hardest particle  $p_1$  is split into a collinear pair ( $p_{1a}, p_{1b}$ )  
1268 (as is common in the fragmentation process for a hard parton), the jet clustering algorithm must  
1269 still recognize ( $p_{1a}, p_{1b}$ ) as the hardest jet in the collision. If another softer particle  $p_2$  with  
1270  $p_{t,1a}, p_{t,1b} < p_{t,2} < p_{t,1}$  is instead considered the hardest particle in the event, a different final  
1271 set of jets would be returned. Collinear safety is a requirement of perturbative QCD, to ensure  
1272 non-divergent higher-order calculations [62]. The anti- $k_t$  algorithm's tendency to cluster hard par-  
1273 ticles first ensures its collinear safety. By satisfying the IRC safety requirement, anti- $k_t$  jets can be  
1274 calculated using perturbative QCD, which improves comparisons with theory.

#### 1275 5.4.4 Ghost Track Association

1276 Once a collection of jets has been created, the jet objects can be studied at both the event-level  
1277 and the jet-level. In the event-level picture, the momentum, energy, and geometric orientation of  
1278 the jets within an event are considered. This yields important information about decay of any  
1279 resonant heavy objects, the total energy in the event, and the distribution of energy amongst the  
1280 jets. In the jet-level picture, the particle constituents of the jet are considered. The momentum,  
1281 energy, and geometric orientation of the associated particle tracks provides a low-level picture of  
1282 the jet, which can help determine if the properties of the jet are consistent with standard QCD, or  
1283 if new physics processes might be represented within the low-level patterns. Jet-level analysis is  
1284 also widely used in flavor tagging.

1285 For anti- $k_t$  jets with a radius parameter  $R = 0.4$ , one way of studying the jet-level picture is  
1286 through considering the ghost-associated tracks. Track association is the process of determining  
1287 which tracks should be considered associated with a given jet. In the ghost association algorithm,  
1288 the anti- $k_t$  clustering algorithm is used for the collection of tracks and calorimeter clusters [63].

1289 However, the tracks are considered to have infinitesimal momentum (*ghosts*), so their addition to  
1290 a jet object does not alter the four-momentum of the jet. This ensures the final jet collection is not  
1291 altered by the presence of the ghost tracks in the reclustering, but information about the associated  
1292 tracks for each reconstructed jet becomes available [64].

1293 Ghost tracks are of particular importance to this analysis, as a means of providing a low-level  
1294 picture of the shape of  $R = 0.4$  jets, and discriminating Standard Model QCD-like jets from dark  
1295 QCD-like jets.

## 1296 5.5 Missing Transverse Energy

1297 A simple principle leveraged in ATLAS physics analyses is checking for conservation of mo-  
1298 mentum among the products of any  $pp$  collisions. The initial state transverse momentum of any  
1299  $pp$  collision is always zero, so the transverse momentum of all final state particles should likewise  
1300 be zero. The missing transverse energy,  $E_T^{\text{miss}}$ , is determined by the magnitude of the negative  
1301 momentum vector sum of all final state objects resulting from the  $pp$  collision.

1302 Specifically, the objects considered in the  $E_T^{\text{miss}}$  calculation are photons, electrons, muons, jets,  
1303 and soft terms. The first four items comprise the hard components of the  $E_T^{\text{miss}}$  calculation, and  
1304 have been discussed previously in this chapter. The final item represents a collection of *soft terms*,  
1305 comprising any detector signals not associated to hard detector objects. These can be based on  
1306 unassociated tracks, or unassociated soft calorimeter clusters. Both are generally not used in the  
1307 same calculation to avoid double counting of soft terms. In this analysis the calorimeter cluster  
1308 soft terms are considered in the  $E_T^{\text{miss}}$  calculation.

1309  $E_T^{\text{miss}}$  can arise due to non-interacting Standard Model objects such as a neutrinos, fake sources  
1310 such as mis-reconstructed objects and dead detector regions, or in some theories, non-interacting  
1311 BSM objects such as a dark matter candidate particles. To understand the amount of  $E_T^{\text{miss}}$  at-  
1312 tributable to detector noise and mis-reconstruction,  $E_T^{\text{miss}}$  is studied in  $Z \rightarrow \mu\mu$  where little real  
1313  $E_T^{\text{miss}}$  is expected [65]. As Figure 5.8 illustrates, the resolution of  $E_T^{\text{miss}}$  generally decreases as  
1314  $E_T^{\text{miss}}$  increases, due to detector resolution effects. As  $E_T^{\text{miss}}$  is an important quantity for most dark

<sup>1315</sup> QCD analyses, limitations in the accuracy of the  $E_T^{\text{miss}}$  calculation must be considered.

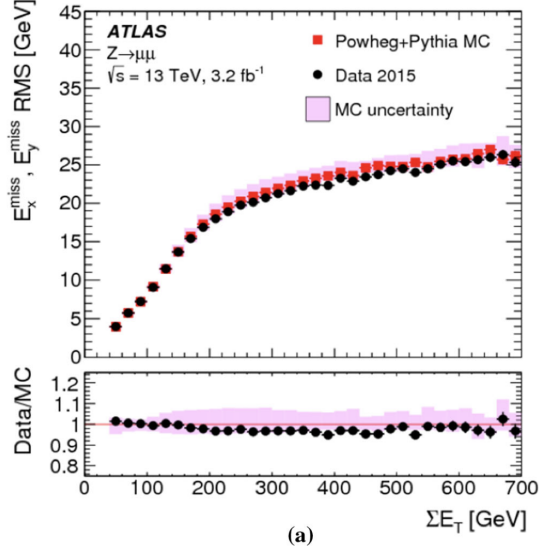


Figure 5.8: A comparison of MC simulation and data for  $Z \rightarrow \mu\mu$  events where real  $E_T^{\text{miss}} = 0$  [65]. The resolution of the missing energy in the transverse ( $x - y$ ) plane is observed to increase with increasing total  $\sum E_T$ .

1316

## **Part III**

1317

## **Search**

1318

1319

## Chapter 6: Monte Carlo and Data

1320     The search for semi-visible jets via s-channel production presented in the following chapters  
1321    is performed with an integrated luminosity of  $139 \text{ fb}^{-1}$  of proton-proton collision data collected  
1322    by the ATLAS detector during Run 2 (2015 - 2018). The full Run 2 dataset is used for the final  
1323    interpretation. Monte Carlo (MC) simulations of background processes and the semi-visible jet  
1324    signal process are used in the development of the analysis strategy, and in the final interpretation  
1325    to set limits on the observed cross-section of the signal model. This chapter will provide details  
1326    about the full Run 2 dataset, and the background MC simulations, and the signal MC simulations  
1327    used in this search.

1328    **6.1 Data**

1329     The  $139 \text{ fb}^{-1}$  integrated luminosity of proton-proton collision data used for physics analyses  
1330    are required to pass a set of data quality checks. In Run 2 94% of the  $p_T$  collisions delivered by  
1331    the LHC were successfully recorded by the ATLAS experiment, as illustrated in Figure 6.1. 95%  
1332    of the data recorded by the ATLAS experiment was marked as “good for physics”, resulting in  $139$   
1333     $\text{fb}^{-1}$  of integrated luminosity. Events are rejected if they are corrupted or incomplete, or if they  
1334    were recorded during a subsystem malfunction.

1335     Events for this analysis are further required to pass a single-jet trigger selection, where events  
1336    are required to have at least one jet with a  $p_T$  that exceeds a certain value. The lowest  $p_T$  un-  
1337    prescaled<sup>1</sup> single jet trigger threshold for each period is as follows:

1338       • 2015:  $p_T \geq 360 \text{ GeV}$

---

<sup>1</sup>An unprescaled trigger records every event that meets the trigger requirement. A prescaled trigger only records a fraction of events that meet the trigger requirement.

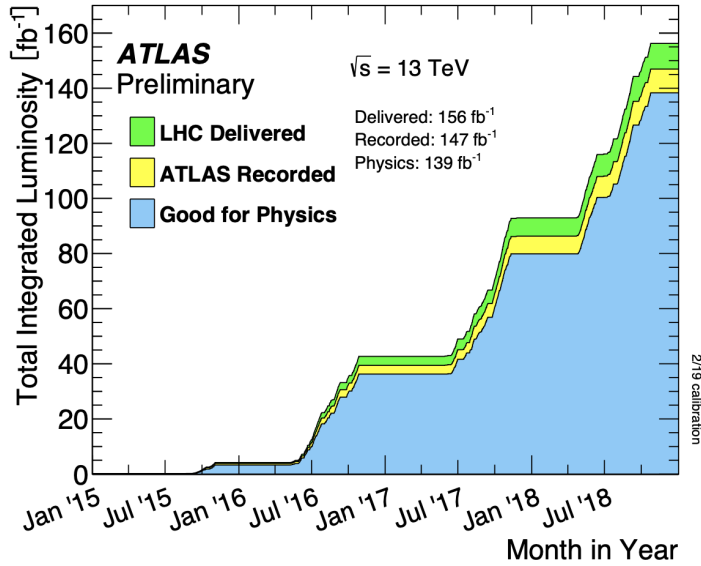


Figure 6.1: Integrated luminosity for the ATLAS experiment as a function of time during Run 2 [66]

- 2016 & 2017:  $p_T \geq 380$  GeV

- 2018:  $p_T \geq 420$  GeV

A post-trigger selection of *leading* jet  $p_T > 450$  GeV ensures these triggers are fully efficient, meaning that the jets are comfortably above the trigger threshold. The jet in the event with the highest  $p_T$  is termed the *leading jet* (or  $j_1$ ), while the jet with the second highest  $p_T$  is termed the *subleading jet* (or  $j_2$ ). The jet collection used is anti- $k_t$  EM particle flow jets with a radius parameter of  $R = 0.4$ , also referred to as small- $R$  jets.

Due to the variance in visible and invisible momenta due to the  $R_{inv}$  parameter of the signal model, many signals also have significant  $E_T^{\text{miss}}$ . The use of a  $E_T^{\text{miss}}$  trigger to select events was considered, and the single jet approach described here was found to preserve more signal events across the grid, particularly in the high resonance mass and low  $R_{inv}$  region of phase space. These studies are documented in Appendix A.

The data are subject to a blinding strategy throughout the analysis design so as to mitigate analyzer-induced bias. Blinded and unblinded region definitions are described further in Section 8.1.

1354 **6.2 Simulation**

1355 Simulated events are generated with a variety of Monte Carlo (MC) generator processes that  
1356 run in stages. The  $p p$  hard scatter physics process is simulated, and the final state particles are  
1357 subsequently showered and decayed. This full description of the event is then propagated through  
1358 a detailed detector simulation based on GEANT4 [67]. The MC simulation is weighted to match  
1359 the distribution of the average number of interactions per bunch crossing  $\mu$  observed in collision  
1360 data.

1361 All simulated samples included in this analysis were produced with three different MC cam-  
1362 paigns: `mc20a` corresponds to 2015-2016 data-taking conditions, `mc20d` to 2017, and `mc20e` to  
1363 2018. These three campaigns are weighted to the integrated luminosities of their respective data-  
1364 taking periods and combined to produce simulation for the entire Run 2 dataset. Simulated events  
1365 are reconstructed with the same algorithms run on collision data.

1366 **6.2.1 Simulated Backgrounds**

1367 Although the final background estimation is data-driven, background MC is studied for analysis  
1368 optimization and machine learning tool development.

1369 Dijet QCD is the dominant background process. QCD is simulated with PYTHIA8 [68], and  
1370 generated in approximate slices of  $p_T$ , to ensure high statistics across the momentum spectrum.  
1371 The slices are then reweighted using MC generated event weights to create a physical distribution.  
1372 Figure 6.2 illustrates the 8 momentum slices used in this analysis.

1373 Due to presence of  $E_T^{\text{miss}}$  in the SVJ signals, additional MC background processes are required  
1374 to create a full picture of the relevant background. The  $Z \rightarrow \nu\nu$  process contributes to the back-  
1375 ground due to its high missing energy. Leptonic W/Z decays and W/Z+jets are also included as  
1376 they can contribute both additional missing energy and significant hadronic activity. Single top  
1377 and  $t\bar{t}$  processes are also considered for their contribution to hadronic activity. After the analysis

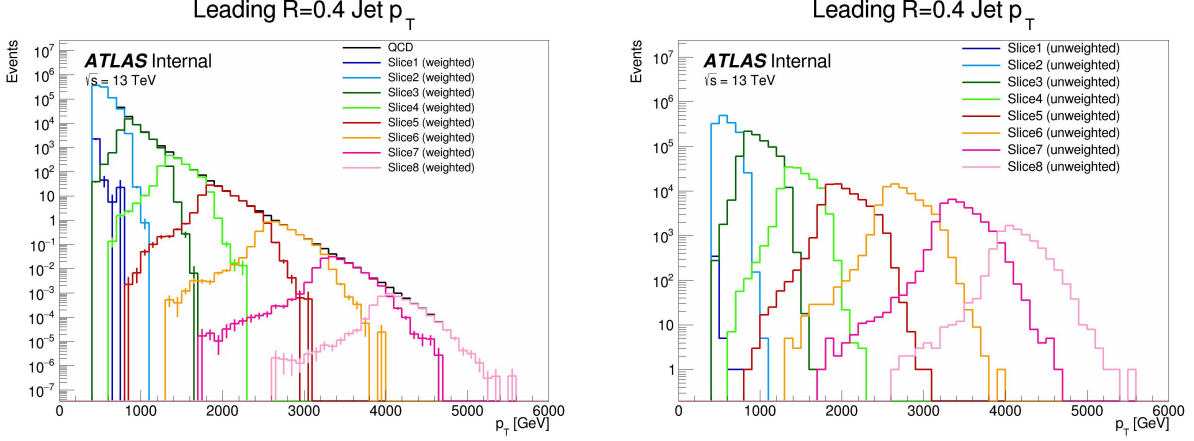


Figure 6.2: The transverse momentum slices of the QCD MC simulation, overlayed to show how they come together to create a smooth distribution (left) once weighted properly. The original unweighted distribution is shown on the right, illustrating the enhanced statistics for the high  $p_T$  range.

<sup>1378</sup> *preselection*<sup>2</sup> is applied to isolate events most relevant to the SVJ topology, the background compo-  
<sup>1379</sup> sition is 76% QCD, 12%  $W+jets$ , 8% top and  $t\bar{t}$  processes, and 4%  $Z \rightarrow vv$ . Figure 6.3 illustrates  
<sup>1380</sup> the background composition for the analysis. The lower panel in Figure 6.3 illustrates the ratio  
<sup>1381</sup> between data (black) and the combined MC processes (grey). While the agreement between data  
<sup>1382</sup> and MC is not perfect (ratio = 1.0 for all  $E_T^{\text{miss}}$  values), the difference is < 20% throughout the  
<sup>1383</sup> distribution. This is within tolerance for this analysis, since the final background estimation will  
<sup>1384</sup> be data driven, and background MC is only needed for approximate modeling. Analysis selections  
<sup>1385</sup> for high energy jets (discussed in Section 8.1) create some sculpting in the  $Z \rightarrow vv$  and  $W+jets$   
<sup>1386</sup> distributions; however, the total  $E_T^{\text{miss}}$  distribution is smoothly falling so this is not an issue.

### <sup>1387</sup> 6.2.2 Signal Simulation

<sup>1388</sup> The Hidden Valley (HV) signal model implementation is based on Ref [22]. The s-channel  
<sup>1389</sup> semi-visible jet model, which was described in Chapter 2, is governed by a number of parameters.  
<sup>1390</sup> The mass of the mediator  $m_{Z'}$  can be set, together with the couplings of the  $Z'$  to the visible and  
<sup>1391</sup> dark quarks  $g_q$  and  $g_{q_D}$ . The dark sector shower is governed by the number of dark colors  $N_{c_D}$ ,

<sup>2</sup>A preselection is a set of cuts on physical observables used to isolate a collection of events which are most likely to contain the desired signal. The preselection for this analysis will be discussed in Section 8.1

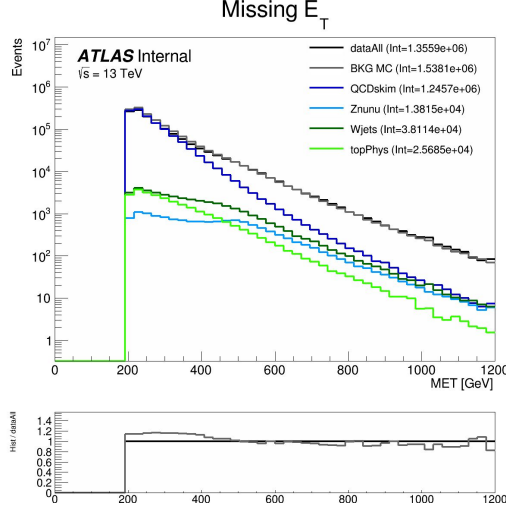


Figure 6.3: Background processes relevant to the SVJ signal.

1392 the number of dark flavors  $N_{f_D}$ , and the dark sector confinement scale  $\Lambda_D$ . There is also the  
 1393 characteristic scale of the dark hadrons  $m_{dark}$ , determined by the mass of the dark quarks  $m_{q_D}$ .  
 1394 The characteristic scale determines the mass of the dark hadrons, which can be pseudoscalars  $m_{\pi_D}$   
 1395 or vectors  $m_{\rho_D}$ . Finally, the average fraction of invisible particles in the final state jet is dictated  
 1396 by  $R_{inv}$ .

1397 The chosen parameters for this model were carefully selected in collaboration with theorists  
 1398 to be compatible with the new benchmarks established in the 2021 Snowmass process [21]. The  
 1399 signal generation allows for up to two initial state radiation jets, and uses a jet-matching scheme  
 1400 described in Ref. [69] and implemented in Ref. [68] to match jets to the original partons.

1401 The choices of fixed parameters for the Pythia8 HV model are summarized in Table 6.1. A  
 1402 detailed discussion of these parameters and their implications on the dark shower topology can be  
 1403 found in Ref. [21]. The mass choices for the dark quark and the dark hadrons are also summarized  
 1404 in Table 6.2.

1405 Note that the number of dark flavors differs from the Snowmass recommendation of  $N_{f_D} =$   
 1406 4. This change is minimal in impact because  $R_{inv}$  is set explicitly (rather than allowing it to  
 1407 arise naturally from the HV theory), and allows this ATLAS analysis result to remain comparable  
 1408 with the CMS semi-visible jets s-channel analysis [70] and the ATLAS semi-visible jets t-channel

Parameter	Value
$N_{c_D}$	3.0
$\Lambda_D$	10.0 GeV
$N_{f_D}$	2.0
$g_q$	0.25
$g_{q_D}$	0.5

Table 6.1: Fixed parameters in the Pythia8 HV model

Parameter	Value [GeV]
$m_{\pi_D}$	17.0
$m_{\rho_D}$	31.77
$m_{q_D}$	10.0

Table 6.2: Values for  $m_{dark}$

1409 analysis [71].

1410 The mediator mass  $m_{Z'}$  and the fraction of invisible particles in the final state  $R_{inv}$  vary, and  
 1411 are used to define the search grid.  $m_{Z'}$  varies between 2.0 TeV and 5.0 TeV, while  $R_{inv}$  varies from  
 1412 0.2 to 0.8.  $R_{inv}$  values of 0.2, 0.4, 0.6, and 0.8 are generated for each  $m_{Z'}$  mass point. Table 6.3  
 1413 illustrates the signal grid and the associated cross-section for each signal. There are a total of 24  
 1414 signal points (6  $Z'$  masses  $\times$  4  $R_{inv}$  settings) considered in this analysis.

1415 Samples are generated using MADGRAPH5 [72] version 2.9.9 interfaced to PYTHIA8.244P3 [68]  
 1416 for shower and hadronization with NNPDF23LO PDF [73] and the ATLAS A14 [74] to tune the  
 1417 underlying event data.

$m_{Z'}$ (GeV)	Cross section (fb)
2000	252
2500	74.2
3000	24.5
3500	8.83
4000	3.49
5000	0.757

Table 6.3: Mass points and cross sections of the SVJ search signal grid. The cross section is determined only by the  $Z'$  mass and is not impacted by the  $R_{inv}$ .

## Chapter 7: Machine Learning Tools

### 1420 7.1 Introduction

1421 The search for semi-visible jets presents an opportunity to use novel machine learning (ML)  
 1422 tools to uncover patterns in the behavior of dark QCD. The subtlety of the shower differences  
 1423 between dark QCD (signal) and SM QCD (background) motivates a complex model that can ac-  
 1424 cept high-dimensional low-level information, such as particle track information, to understand key  
 1425 differences between signal and background patterns. Additionally, the large number of theory pa-  
 1426 rameters which can be chosen arbitrarily and affect the shape of the dark QCD shower motivate  
 1427 exploring a data-driven machine learning approach, which could be sensitive to a wide variety of  
 1428 dark QCD behavior.

1429 To this end, two machine learning approaches are developed for this search, which are used  
 1430 in tandem. The first is a *supervised* ML method where the ML algorithm is built to maximize  
 1431 sensitivity to the specific SVJ signal models described in Section 6.2.2. Here, supervised refers to  
 1432 the use of full and correct *labels*<sup>1</sup> for all events considered during model training. The second is  
 1433 a semi-supervised method, where training of the model is data-driven (no signal hypothesis used  
 1434 during training) and labels are only partially provided during training. The semi-supervised ML  
 1435 algorithm broadens the discovery sensitivity of the search, and reduces the dependence on the exact  
 1436 theory parameters chosen for signal model simulation.

1437 The two different ML algorithms used in this approach will be explored in Section 7.2 and  
 1438 Section 7.3, along with their application in the SVJ analysis strategy. In the following Section 7.1.1,  
 1439 a brief overview of fundamental machine learning concepts is presented.

---

<sup>1</sup>In machine learning a label refers to the correct identification information for an input. In the case of the binary classifier algorithm discussed here, the label is either “signal” or “background”.

1440 7.1.1 Machine Learning Fundamentals

1441 The machine learning tools presented in this chapter depend on two basic *architectures*. An  
1442 ML architecture refers to the specific neural network design used to create an ML *algorithm* (or  
1443 *tool*).

1444 The first basic architecture is a *deep neural network* (DNN) [75]. Figure 7.1 illustrates the  
1445 concept. The hidden layers of a DNN allow the network to store information about the importance  
1446 of each input feature and the importance of correlations amongst the input features. The elements  
1447 of each layer are known as *nodes*. In a fully connected network like the one shown each node  
1448 receives input from every node in the previous layer, represented by the arrows in the diagram.  
1449 Each node input has an associated *weight* which is adjusted during training. The node combines  
1450 the inputs and their associated weights according to an *activation function*. The output of the  
1451 activation function becomes the value associated to the node, which is then used as input to the  
1452 subsequent layer.

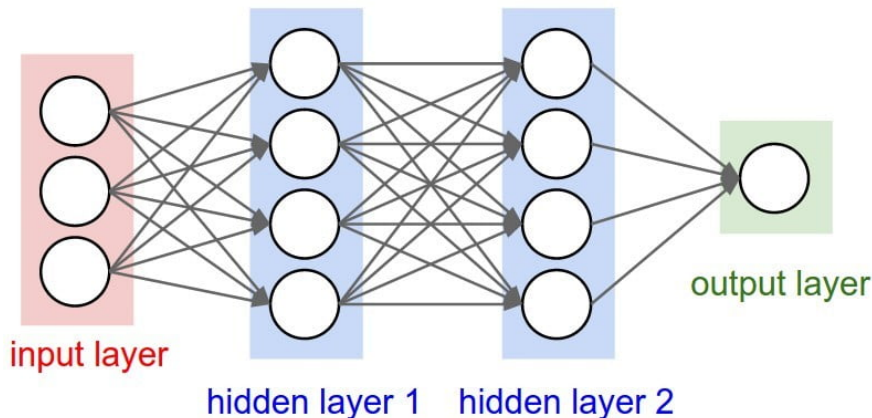


Figure 7.1: A diagram of a deep neural network architecture [76].

1453 A *loss function* measures the performance of the model. The *loss* calculated by the loss function  
1454 compares the output of the model to the correct response. In a *classifier* model the output layer  
1455 is the probability that the input fits a certain category, for example “signal” (1.0) or “background”  
1456 (0.0). This probability is called the *score*. The loss function calculates the accuracy of the scores.  
1457 For example a signal input that receives a score of 0.9 would result in a small loss, while the same

1458 event given a score of 0.1 would result in a large loss. Figure 7.2 illustrates a typical classifier  
1459 score response.

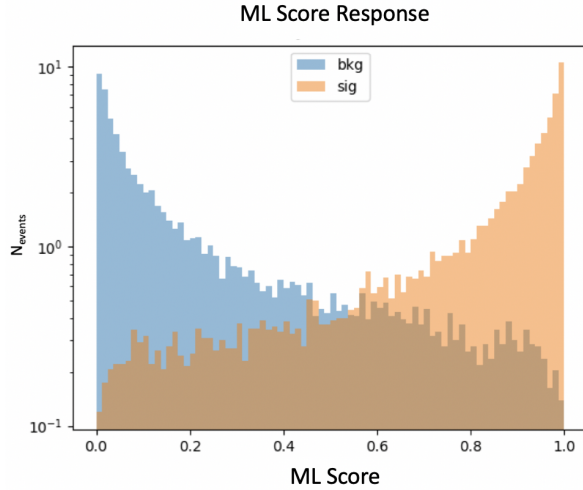


Figure 7.2: An example score distribution for a binary classifier. A higher score indicates a greater probability of being signal. Most signal events (orange) receive a high score while most background events (blue) receive a low score, indicating good classification.

1460 The network improves by training over many *epochs*, which refers to the process of the ML  
1461 algorithm evaluating all training events. After each epoch, the *optimizer* adjusts the weights to  
1462 reduce the loss. The *learning rate* determines how big of an adjustment the network is allowed  
1463 to make. During training, a set of events are set aside to use for *validation*. The purpose of  
1464 the validation data is to prevent *overtraining*. If a network is sufficiently large and complex, the  
1465 network could lose generality by perfectly learning (or “memorizing”) the correct response for  
1466 every training event. This would minimize the training loss, but could result in the network failing  
1467 to correctly classify events it hasn’t seen before. By evaluating the loss of the validation data the  
1468 user can determine if the network is overtrained; the training loss should not greatly exceed the  
1469 validation loss.

1470 ML algorithms are often evaluated through a *receiver operating characteristic* (ROC). The  
1471 ROC compares the true positive rate (correct classification) with the false positive rate (false clas-  
1472 sification). An example ROC curve is shown in Figure 7.3. If a classifier is performant, the  
1473 true positive rate will be larger than the false positive rate for all possible false positive rates. If

1474 the network has no classifying power, the true positive rate and false positive rate will be equal  
 1475 throughout. The *area under the curve* (AUC) is an important metric for evaluating the ROC. The  
 1476 AUC is the integral of the ROC curve. An AUC of 1.0 indicates perfect performance, while an  
 1477 AUC of 0.5 indicates that the network is no better than random guessing.

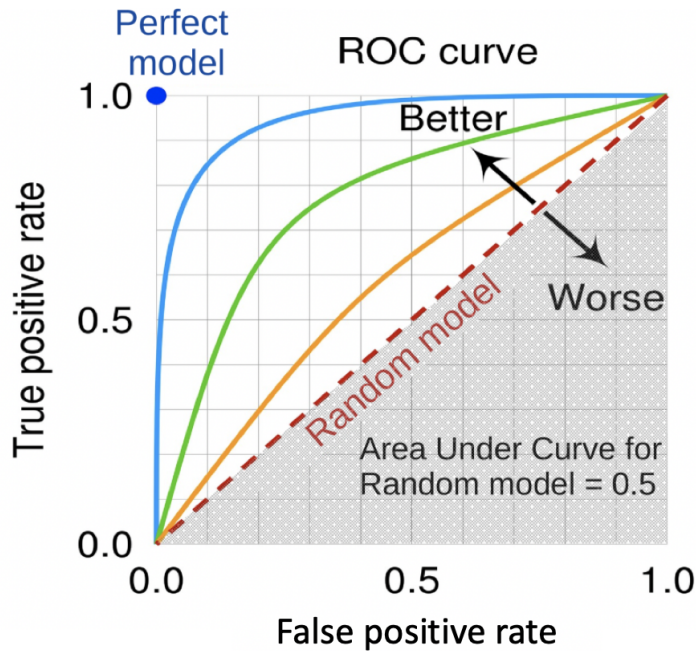


Figure 7.3: Several example ROC curves. The AUC is also illustrated [77].

1478 The second architecture that is important to this thesis is the *auto-encoder* (AE) [78]. Unlike  
 1479 a DNN, which is a supervised network that depends on the use of correct labels to determine  
 1480 the loss, the AE calculates loss by comparing the input and output layers. Figure 7.4 illustrates the  
 1481 concept. The network is designed to extract the most salient features of the input via dimensionality  
 1482 reduction. This is achieved by compressing the input to a lower dimensional *latent space*, and  
 1483 then attempting to reconstruct the original input from that latent space. The loss is calculated by  
 1484 comparing the output of the network with the input. While the goal of a classifier is to correctly  
 1485 categorize the inputs, the goal of the AE is to correctly reconstruct the inputs. This allows the AE  
 1486 to be used for *anomaly detection*. The kinds of events that are seen most often during training  
 1487 will be reconstructed well by the algorithm, and therefore have the smallest loss. Events which

1488 are anomalous or unusual in the training data will be more difficult for the AE to reconstruct, and  
 1489 therefore receive a larger loss. The loss can be used to create an *anomaly score*, which identifies  
 1490 unusual events with a higher anomaly score.

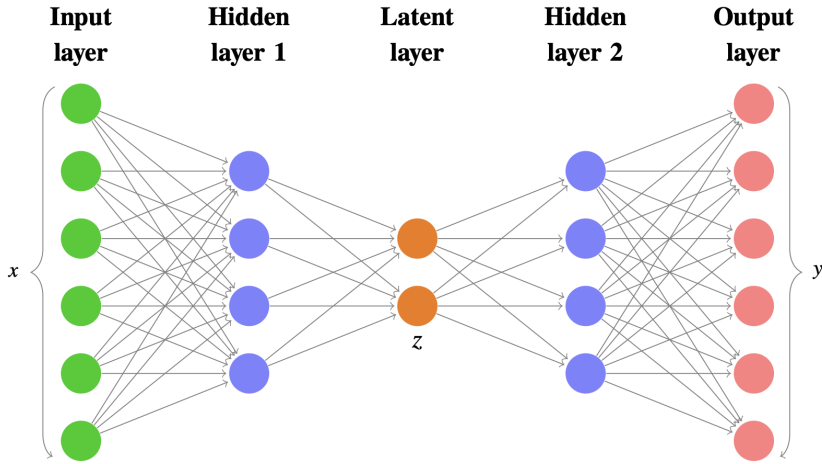


Figure 7.4: A diagram of auto-encoder architecture. The loss is computed as a difference (often the *mean squared error* or MSE) between the input  $x$  and the output  $y$  [79].

## 1491 7.2 Particle Flow Network (Supervised)

1492 The supervised machine learning approach maximizes discovery sensitivity for the SVJ signals  
 1493 considered in this thesis. The networks learns the features of the SVJ signals, allowing the network  
 1494 to be highly efficient in selecting events that resemble the SVJ signal.

### 1495 7.2.1 Architecture Fundamentals

1496 A Particle Flow Network (PFN) [80] architecture is selected for two reasons: *permutation in-*  
 1497 *variant input modeling* to best describe the events consisting of an unordered set of particles, and a  
 1498 *low-level input modeling* to take advantage of the ability of neural networks to uncover patterns in  
 1499 high-dimensional data. *Low-level* refers to using detector level information such as individual par-  
 1500 ticle tracks, rather than *high-level* information such as reconstructed jet objects. Low-level input  
 1501 modeling is chosen to capture the intricacies of dark QCD showers which may not express them-  
 1502 selves in high level objects, as explored in [22]. Permutation invariant input modeling is chosen as

1503 the most accurate representation of a set of particles. In previous work such as Ref. [79], ordered  
1504 input modeling has been observed to *bias* the performance of low-level modeling tools. In this  
1505 case bias means that the performance of the tool was observed to change substantially depending  
1506 on the input ordering; however, there is no physics motivation for choosing any particular order.

1507 The input to the PFN is a collection of particles and their associated physics information, such  
1508 as momentum and trajectory. Constructing the PFN involves the creation of new basis variables  $\Phi$   
1509 for each particle in the input event. This transformation is summarized as  $\vec{p}_i \rightarrow \vec{\Phi}_i$  where  $\vec{p}_i$  is the  
1510 physics information for the  $i$ th particle in the event, and  $\vec{\Phi}_i$  is that same information encoded into  
1511 the  $\Phi$  basis. Permutation invariance is enforced by summing over the  $\Phi$  basis for every particle in  
1512 the event to create a new permutation invariant event representation  $O$ . The creation of  $O$  from  $M$   
1513 particles  $\vec{p}$  with  $d$  physics features each can be expressed as:

$$O(\{\vec{p}_1, \dots, \vec{p}_M\}) = \sum_{i=1}^M \Phi_i(\vec{p}_i) \quad (7.1)$$

1514 where  $\Phi : \mathbb{R}^d \rightarrow \mathbb{R}^l$  is a per particle mapping, with  $l$  being the dimension of the new basis  $O$ .  
1515 Figure 7.5 gives a graphical representation of the use of summation in the PFN over per-particle  
1516 information to create a permutation-invariant event representation.

1517 The  $\Phi$  basis transformation is implemented via a deep neural network. The output of the  
1518 neural network is summed as indicated in Equation 7.1 to create the new permutation invariant  
1519 event representation  $O$ .  $O$  then becomes the input of a second deep neural network  $F$ .  $F$  is a  
1520 classifier network which separates signal and background events. Figure 7.6 provides an annotated  
1521 diagram of the PFN architecture as used in this analysis.

## 1522 7.2.2 Input Modeling, Scaling, and Rotation

1523 In this implementation, the particle input information comes from all tracks associated to the  
1524 leading and subleading jets. The track association method is Ghost association, as discussed in  
1525 Section 5.4.4. A single jet tagger strategy was also considered, but utilizing tracks from both  
1526 leading jets creates a more complete low-level picture of the event. The choice of the two leading

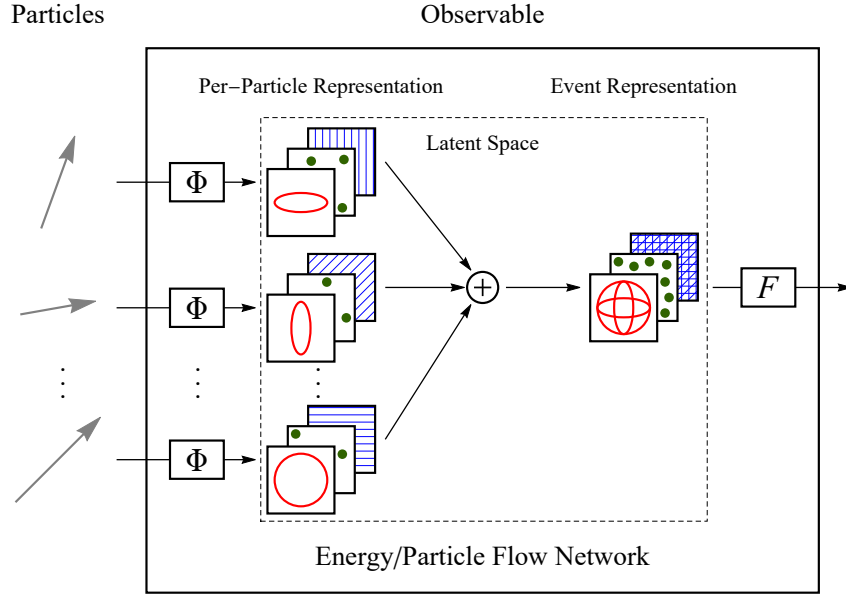


Figure 7.5: The Energy/Particle Flow Network concept, from Ref. [80]. The physics input information is represented as arrows on the left, for an arbitrary number of particles. The  $\Phi$  transformation converts these arrows to 3 graphs, indicating the  $\Phi$  basis dimension  $l$  is 3 in this example. The graphs are then summed for all particles to create  $O$ , or the event representation.

1527 jets is justified in Chapter 8. If we consider the dijet topology of semi-visible jets as illustrated  
 1528 in Figure 7.7, the advantage of modeling both leading jets simultaneously becomes clear. In the  
 1529 semi-visible jet model presented in [22],  $E_T^{\text{miss}}$  in the event is expected to arise due to an imbalance  
 1530 in the number of visible tracks of the two jets associated to the dark quark decay.

1531 Each track is described using six variables: the four-vector of the track ( $p_T$ ,  $\eta$ ,  $\phi$ , E), and the  
 1532 track displacement parameters  $d_0$  and  $z_0$ , where  $d_0$  measures displacement in the radial direction  
 1533 from the beamline and  $z_0$  measures displacement along the beamline from the primary interac-  
 1534 tion point. Figure 7.8 illustrates these coordinates. Up to 80 tracks per jet are allowed, which is  
 1535 a threshold chosen to generally include all the tracks in the jet, which leads to maximal perfor-  
 1536 mance. Figure 7.9 shows the track multiplicity in the leading and subleading jet for the signal and  
 1537 background samples used in training.

1538 These tracks (up to 160 total) are the input to the PFN. Referencing Equation 7.1, this corre-  
 1539 sponds to  $M = 160$  and  $d = 6$ . The two leading jets and their associated tracks are rotated so that  
 1540 the vector sum of the jets, or system average, is aligned with  $(\eta, \phi) = (0, 0)$ . The rotation can be

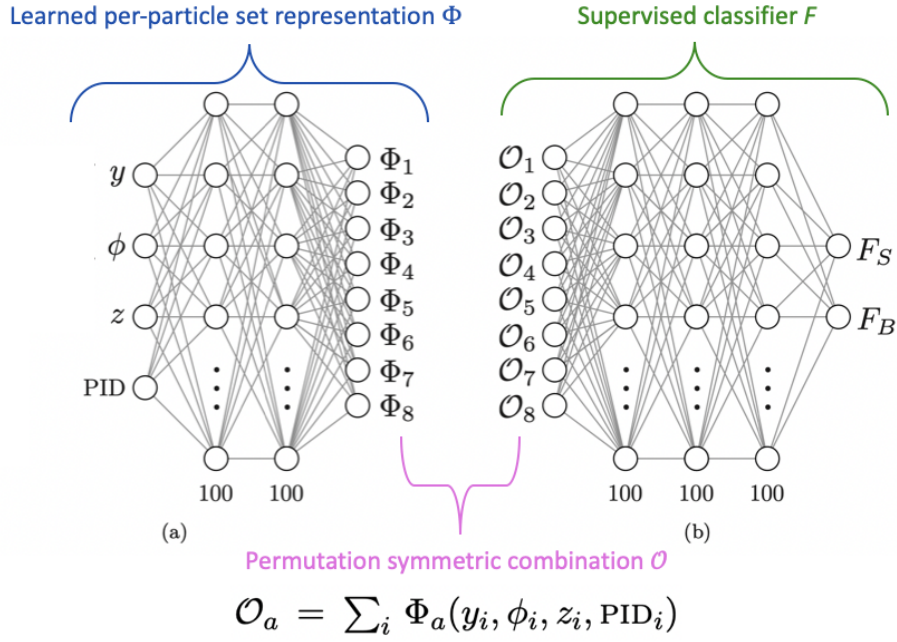


Figure 7.6: An annotated diagram of the PFN architecture.  $y$  and  $\phi$  represent geometric information for the input particles,  $z$  represents energy information, and PID encompasses any other particle ID information in the input. PID is presented in the diagram as a 1-dimensional input, but could represent multiple input dimensions.

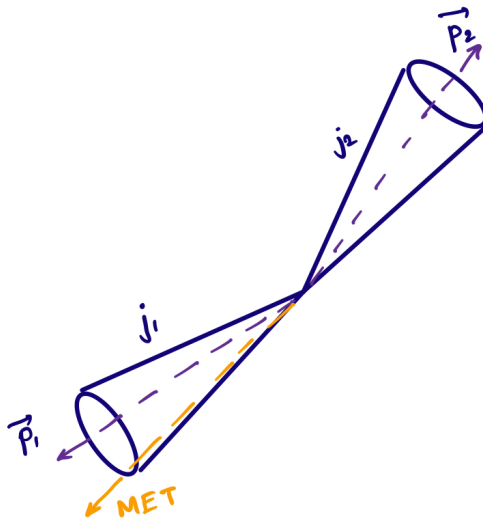


Figure 7.7: An illustration of the expected dijet behavior of semi-visible jets, where one jet is closely aligned with  $E_T^{\text{miss}}$ (MET). In the figure two jet cones  $j_1$  and  $j_2$  are illustrated, along with their associated momentum vectors  $\vec{p}_1$  and  $\vec{p}_2$ .

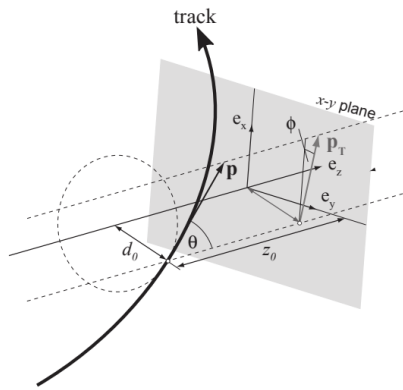


Figure 7.8: Illustration of track coordinates  $d_0$  and  $z_0$ .

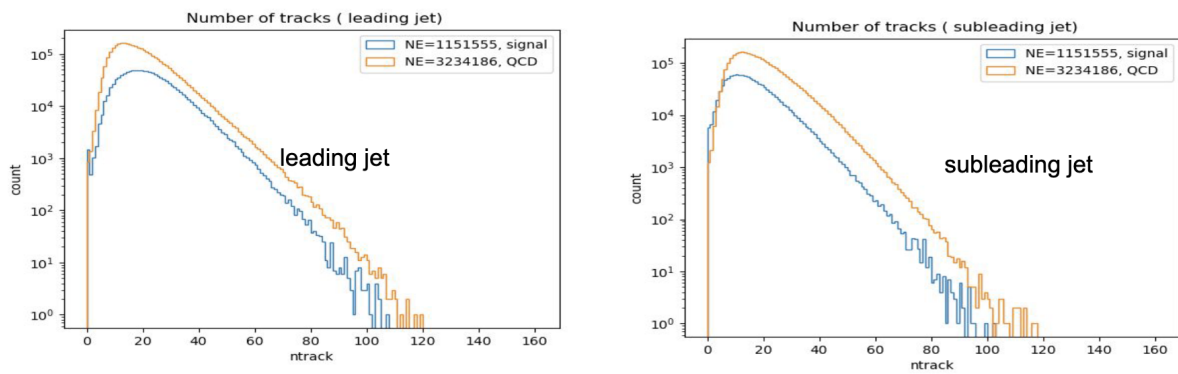


Figure 7.9: Distributions of the track multiplicity in the leading and subleading jets, comparing signal and background PFN training samples.

1541 summarized as

$$\eta'_i = \eta_i - \bar{\eta}, \phi'_i = \phi_i - \bar{\phi} \quad (7.2)$$

1542 where  $(\bar{\eta}, \bar{\phi})$  is the average angle of the dijet system,  $(\eta_i, \phi_i)$  are the original track coordinates,  
1543 and  $(\eta'_i, \phi'_i)$  are the rotated track coordinates. Figure 7.10 illustrates the rotation process. The  
1544 rotation ensures that the information used by the algorithm is the relative orientation of the jets  
1545 (and associated tracks) to each other, not their absolute position in the detector. Each track is  
1546 normalized to its relative fraction of the total dijet system energy and transverse momentum; this  
1547 enforces agnosticism to the total energy and transverse momentum of the event. The rotation and  
1548 scaling are motivated by the procedures described in Ref. [80] to improve the performance of the  
1549 PFN.

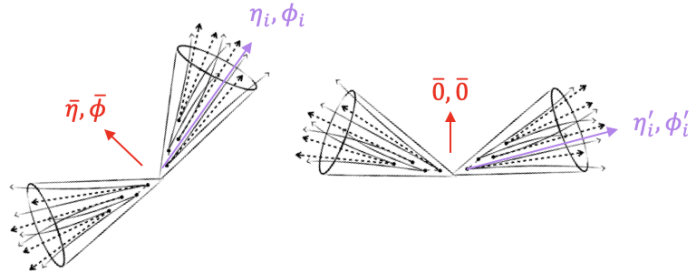


Figure 7.10: A diagram demonstrating how the two jet system is rotated in  $(\eta, \phi)$ . The jet cones and associated jet tracks are illustrated. The dashed tracks represent dark hadrons while the solid tracks represent SM hadrons. The system average  $(\bar{\eta}, \bar{\phi})$  is shown in red and an example track with coordinates  $(\eta_i, \phi_i)$  is shown in purple.

1550 Finally, each of the 6 track variables is scaled so that its range is [0,1]. This is a common  
1551 preprocessing step that ensures the input data is bounded over a similar range, so that arbitrarily  
1552 large values don't develop an outsized impact on the model. The track momentum and energy  
1553 normalization mentioned above naturally enforces that these values are restrained between [0,1].  
1554 The  $\eta$  and  $\phi$  values are naturally bounded, so for these values the  $\eta$  tracking range<sup>2</sup> of [-2.5, 2.5]  
1555 and the full  $\phi$  range  $[-\pi, \pi]$  are mapped to [0,1]. The displacement variables are restricted to [0,1]

<sup>2</sup>This range is dictated by the  $|\eta|$  coverage range of the Inner Detector, as shown in Table 4.1

1556 via the standard MINMAXSCALER [81] method which determines the minimum and maximum  
1557 values observed in training, and maps those boundaries to 0 and 1 respectively.

1558 Figure 7.11 shows the kinematics of each of 6 track variables for background and signal. Fig-  
1559 ure 7.12 shows each of the 6 track variables after scaling and rotation have been applied, demon-  
1560 strating the impact of these procedures, as well as the track level similarities and differences be-  
1561 tween the background SM QCD processes and the signal SVJ processes. Figure 7.13 illustrates  
1562 that the data is well modeled by the MC at track level.

1563 The  $\phi$  distribution is of note for its jagged appearance in QCD MC. This arises due to dead tile  
1564 calorimeter cells in certain  $\phi$  regions, the effects of which are seen in data and modeled in QCD  
1565 MC but not modeled in SVJ signal MC. Appendix B.5.2 contains more information about how the  
1566 issue was addressed in data. The distribution is not of concern for the PFN training because of  
1567 the rotation process, which replaces the information about absolute detector  $\phi$  measurements with  
1568 the relative  $\phi'$  measurement. This is illustrated in Figure 7.12, where it is observed that for both  
1569 signal and background the tracks are clustered back to back, centered at  $-\pi/2$  and  $\pi/2$  ( 0.25 and  
1570 0.75 after scaling). The only remaining difference is that the signal tracks are more likely to be  
1571 close to the system average  $\bar{\phi}$  than the background jet tracks. This is demonstrated by the excess of  
1572 signal events in the center of the  $\phi'$  plot. This orientation difference is a real feature of the signal  
1573 model, confirmed in Figure 8.2 which illustrates that signal jets are more likely to have low  $\Delta\phi$   
1574 than background jets.

## Kinematic Inputs

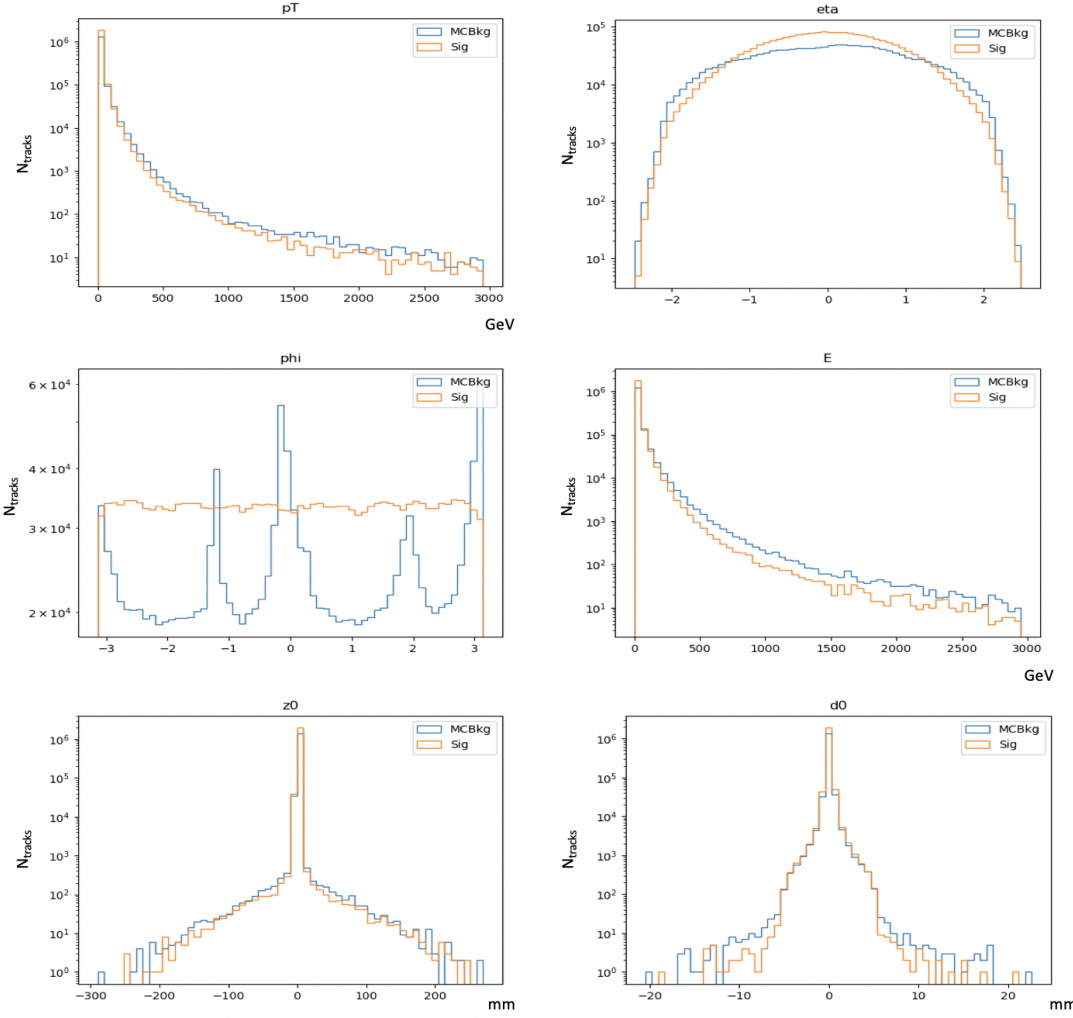


Figure 7.11: The 6 PFN track variables in background MC (blue) and signal MC (orange) before scaling and rotation. The track kinematics are largely similar, and the variation in the  $\phi$  distribution is explained in the text.

### Rotated & Scaled Inputs

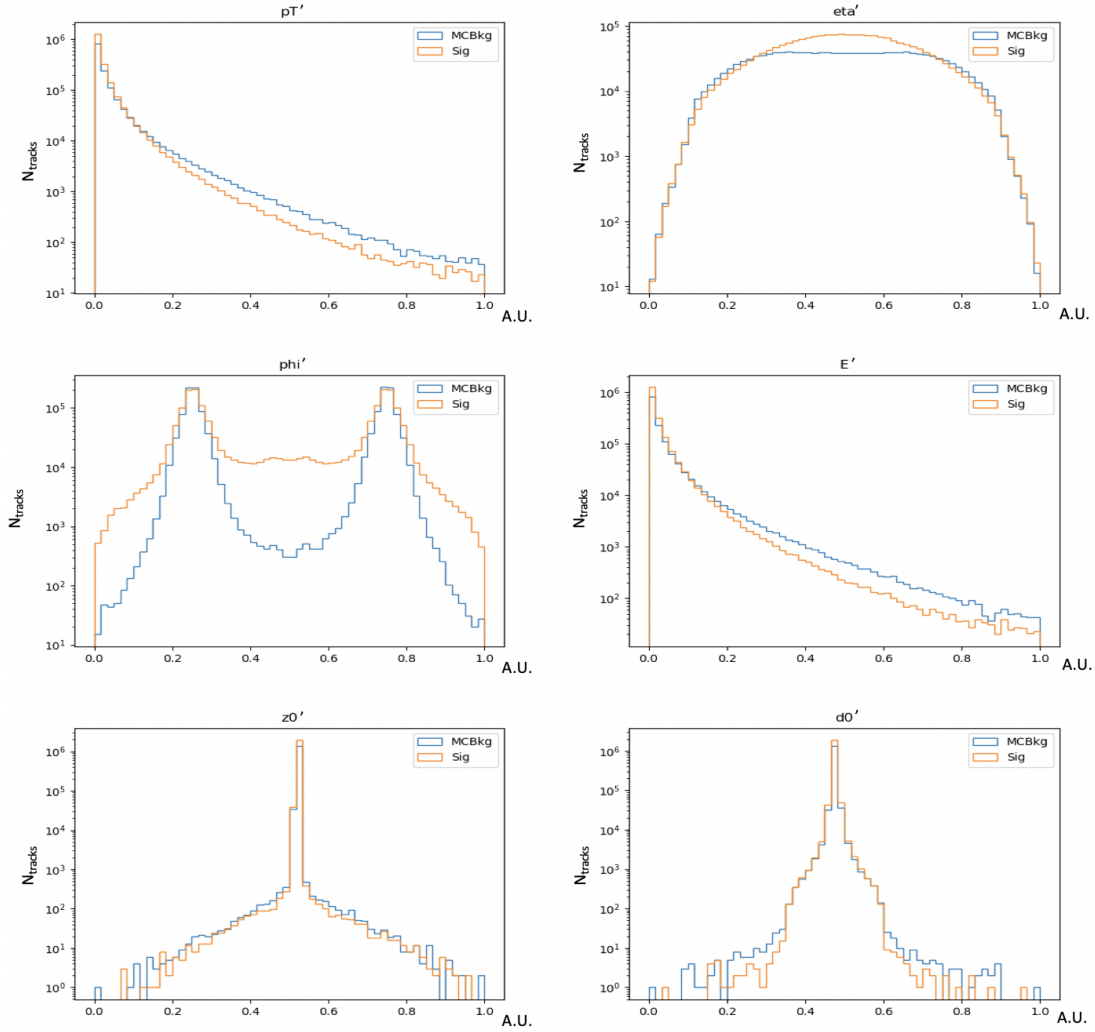


Figure 7.12: The 6 PFN track variables in background MC (blue) and signal MC (orange) after scaling and rotation. The  $\phi$  distribution is modified by the rotation procedure, as explained in the text.

### Rotated & Scaled Inputs

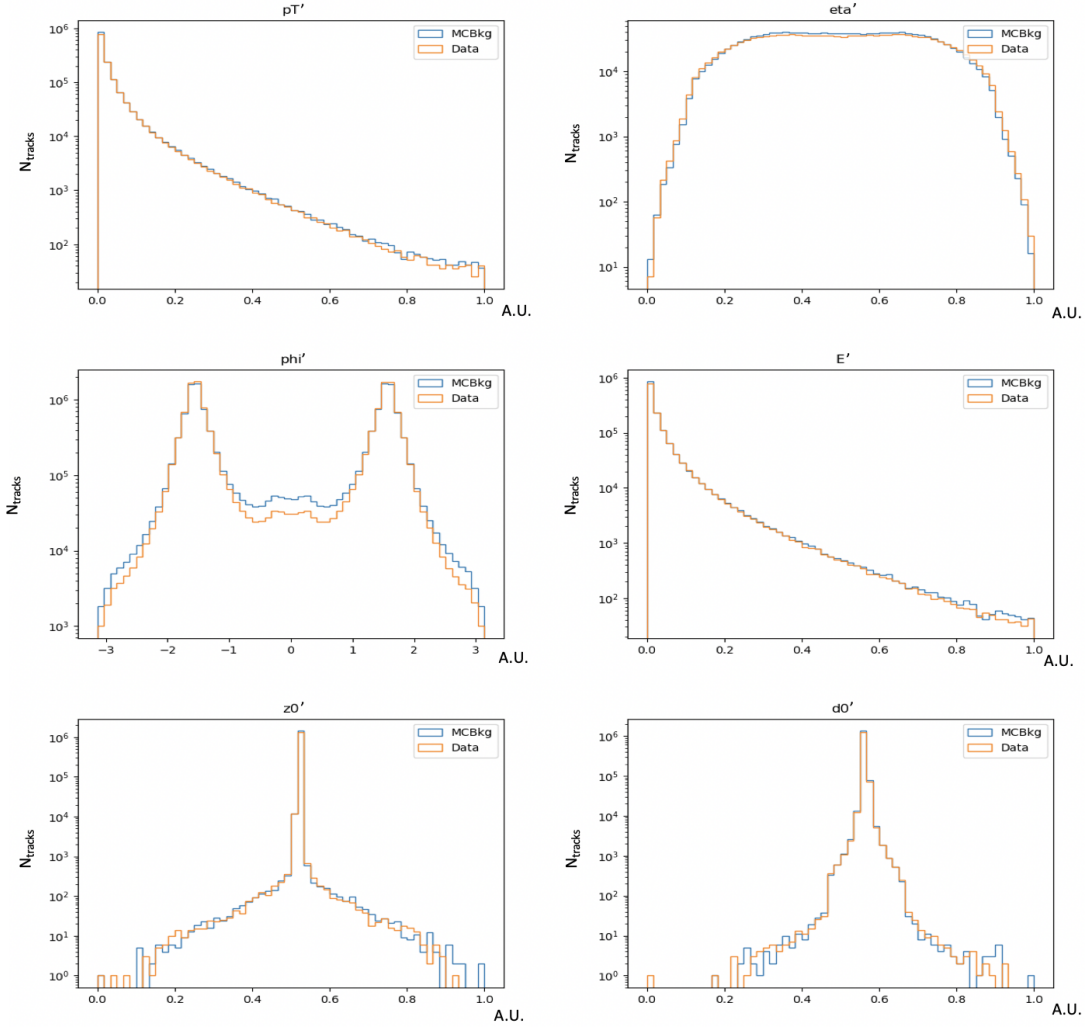


Figure 7.13: The 6 PFN track variables in background MC (blue) and data (orange), after the scaling and rotation procedure is applied. There is excellent modeling of the data by the MC within the track variables. The slight discrepancy in the  $\phi$  distribution due to the inaccuracies of modeling dead TileCal cells in the QCD MC is considered. The level of discrepancy is determined to be within tolerance given that the final result will be data driven and the QCD model is used in the PFN training only.

1575 7.2.3 Training

1576 As seen in Figure 7.6, two networks are defined and combined for the PFN architecture. In  
1577 our implementation the input layer has a dimension of 6, accounting for the 6 track variables de-  
1578 scribed in the previous section. The first network, termed the  $\Phi$  network, creates the per-particle  
1579 set representation as illustrated in Figure 7.5. The  $\Phi$  network has 2 hidden layers each of dimen-  
1580 sion 75, and an output later of dimension 64. These dimensions were chosen via an optimization  
1581 procedure which balanced network complexity (achieved with more dimensions) against training  
1582 time (achieved with fewer dimensions). The two hidden layers and  $\Phi$  output layer all use a RELU  
1583 activation function [81], following the work of Ref. [80].

1584 The input layer of the classifier  $F$  network is required to have the same dimension as the output  
1585 layer of the  $\Phi$  network, and therefore takes dimension 64. This network contains 3 hidden layers  
1586 with 75 nodes each, and again uses RELU activation [81]. The final layer is the binary classifier  
1587 result with dimension 2, which uses a SOFTMAX activation [81] that is well suited for classification.  
1588 The loss function for the complete PFN network is CATEGORICALCROSSENTROPY [81], which  
1589 is a standard loss function for DNN classifiers. The standard Adam optimizer [82] [81] is used  
1590 with a learning rate of 0.001. The learning rate was reduced from the nominal learning rate of 0.01  
1591 presented in Ref. [80] to prevent overtraining.

1592 The PFN is a supervised algorithm, and is therefore trained on a labeled mixture of signal  
1593 and background events. The signal input is an even mixture of all signal points considered in  
1594 this analysis. Although the full simulated background for this analysis is composed of several  
1595 SM processes as discussed in Section 6.2.1, QCD is the dominant background. Training with  
1596 a QCD-only background sample is determined to produce better results than training using the  
1597 full background mixture. Including MC backgrounds that are enriched in  $E_T^{\text{miss}}$  (recall Figure 6.3)  
1598 reduces the ability of the PFN to classify SVJ signals. This is illustrated in the comparison of  
1599 output classifier distributions in Figure 7.14. The signals used for training are the same in both  
1600 cases. When training with a QCD-only background, high  $E_T^{\text{miss}}$  data and MC is more likely to be

1601 classified as signal like; however the increased signal performance means that overall *sensitivity*<sup>3</sup>  
 1602 is higher with a QCD-only training. Additional studies on the optimal PFN training event mixture  
 1603 are available in Appendix B.2.

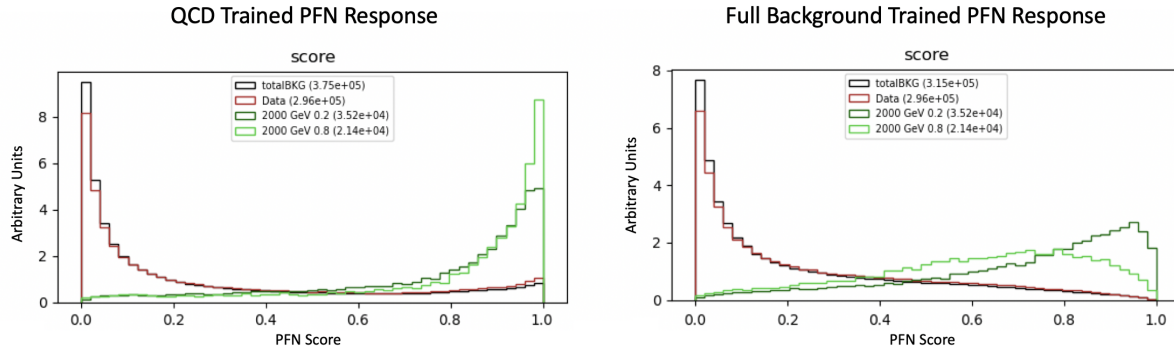


Figure 7.14: PFN score for full-background MC (black), data (red), and 2 representative signal points (green). The left plot is from a QCD-only training, while the right plot is from a full-background training. The histograms have been normalized to visualize the shapes better - the actual number of plotted events is shown in the legend. In the left plot we observe that both signal points are strongly classified as signal-like. In the right plot we observe less background contamination in the high score region, but worse signal classification. Both PFN trainings were tested for their effect on the analysis sensitivity and the QCD-only training was found to be favorable.

1604 500k QCD MC background events and 500k SVJ signal events are used to train the network.  
 1605 The network is trained for 100 epochs. 20% of the training events are used for training validation.  
 1606 Figure 7.15 shows the loss during training, which is stable and shows no indication of overtraining,  
 1607 and the final score that provides signal-background discrimination.

1608 Optimization studies were performed on the PFN, varying the number of training epochs, num-  
 1609 ber of training events, learning rate, number of nodes, and dimension of the  $\Phi$  basis. A summary  
 1610 of these studies is presented in Appendix B.2. The model presented here represents an optimal  
 1611 choice across these parameters.

#### 1612 7.2.4 Performance

1613 The performance of the PFN is assessed via the AUC for each SVJ signal point. Although the  
 1614 PFN is trained against QCD MC only, the performance is evaluated using data as the background

---

<sup>3</sup>Sensitivity is a measure of the ability of an analysis to detect the signal, discussed further in Section 8.1

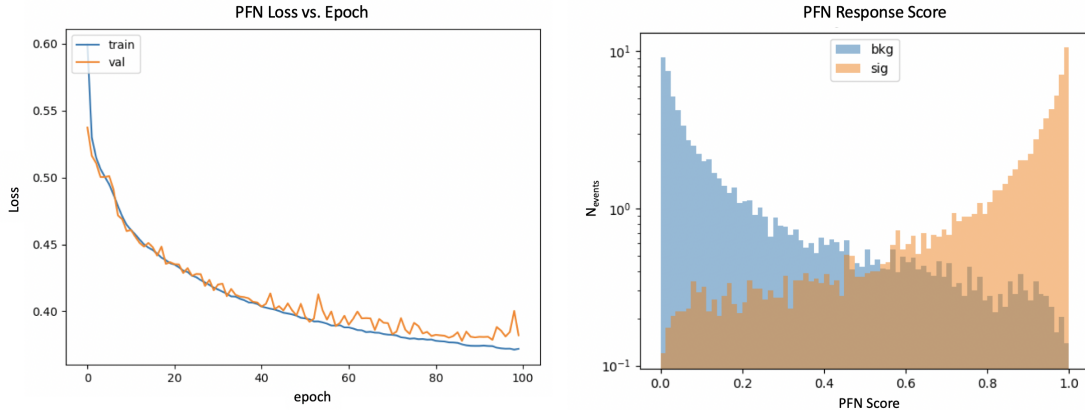


Figure 7.15: PFN architecture loss during training as a function of epoch (left) and the evaluated score for signal and background training samples (right). The loss vs. epoch plot shows that the network is not overtrained. The score plot shows a good separation between signal and background.

1615 sample, since the ultimate task of the PFN is to separate SVJ signals from data, which is dominated  
 1616 by SM processes.

1617 Figure 7.16 shows the ROC curve of one such signal point, illustrating a smooth response.  
 1618 Figure 7.17 shows the AUC of the PFN across the SVJ signal grid, demonstrating that  $AUC > 0.5$   
 1619 is satisfied for all SVJ signals.

1620 Figure 7.18 shows the output score distribution for data and four signals, illustrating the range  
 1621 of scores received by data events in comparison to signal events. As expected, most data events re-  
 1622 ceive a background-like score (close to 0.0), indicating that the data is dominated by SM processes  
 1623 consistent with the background. Most signal events receive a signal-like score (close to 1.0). An  
 1624 optimization procedure determined that a selection of **PFN score > 0.6** can improve signal sensitiv-  
 1625 ity across the grid. The optimization procedure considered the cut that would maximize sensitivity  
 1626 as measured by  $s/\sqrt{b}$ , where  $s$  the number of signal events accepted and  $b$  is the number of back-  
 1627 ground events selected. This score selection is incorporated into the analysis design described in  
 1628 Chapter 8.

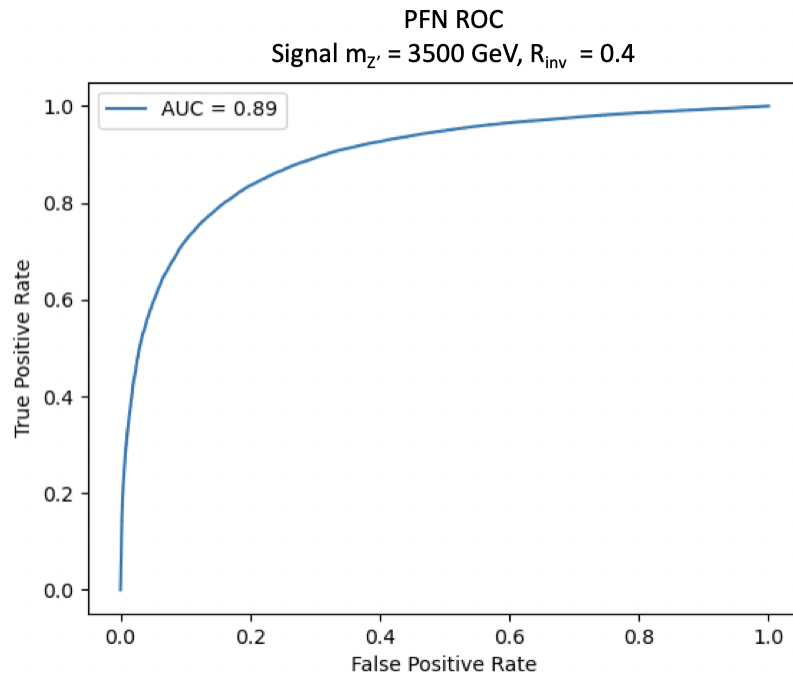


Figure 7.16: ROC for the PFN, using SVJ signal events (true positive) and data (false positive).

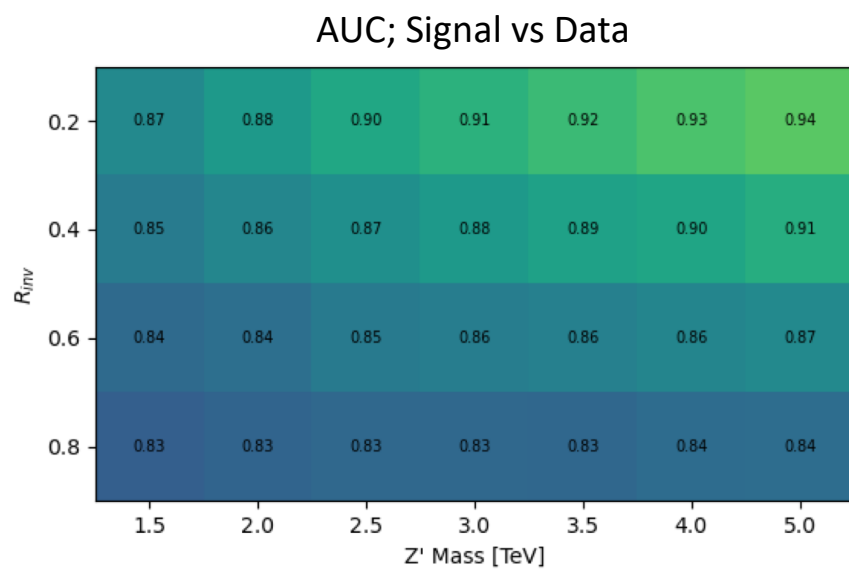


Figure 7.17: AUC for the PFN, shown for each signal in the SVJ grid.

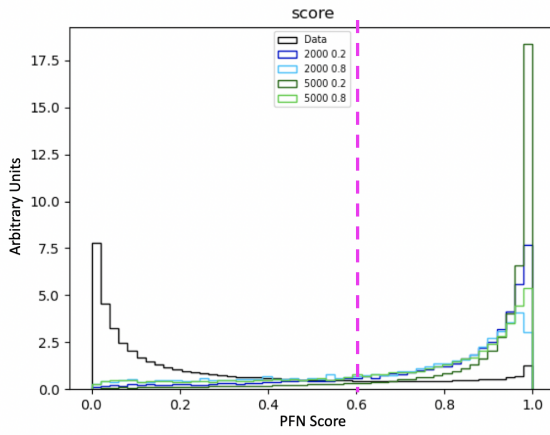


Figure 7.18: Illustration of the PFN score selection, showing the separation between data (black) and 4 signal points (blue and green). The legend information takes the form “ $m_{Z'} R_{inv}$ ” for the signal. The PFN score selection value is shown by the pink line. Only events with a score  $> 0.6$  will be accepted for use in the analysis. We see that most background (data) is rejected, while most signal is accepted.

1629    **7.3 ANTELOPE (Semi-supervised)**

1630    The semi-supervised machine learning approach broadens the discovery potential of the search  
1631    through the use of data-driven training, where no signal model is provided. While broad sensitivity  
1632    is a general goal of LHC searches, it is particularly motivated in the case of dark QCD models,  
1633    which can lead to widely varying topologies depending on the values of model parameters.

1634    **7.3.1 Architecture Fundamentals**

1635    The model-independent search region of this analysis is implemented with a novel ML ap-  
1636    proach that builds on the PFN architecture to construct a tool that is capable of performing low-  
1637    level anomaly detection with permutation-invariant inputs. This tool, referred to as **ANomaly**  
1638    **deTEction on particLe flOw latent sPacE (ANTELOPE)**, is a custom solution designed for this  
1639    analysis.

1640    Figure 7.19 provides a diagram of the ANTELOPE architecture. ANTELOPE uses the trained  
1641    PFN network described in the previous section to generate a permutation invariant event represen-  
1642    tation  $\mathcal{O}$  from track level inputs. The  $\mathcal{O}$  basis is used as the input for a *variational autoencoder*  
1643    (VAE). A VAE is a common variation of a standard AE; the AE becomes *variational* if the la-  
1644    tent space is constructed through Gaussian sampling rather than a vector of weights, as described  
1645    further in Ref. [83]. VAEs have been used in previous ATLAS searches to model low-level par-  
1646    ticle information, such as the search presented in Ref. [84] which used the recurrent architecture  
1647    described in Ref. [79]. One of the limitations of a recurrent architecture is the need to order the  
1648    low-level inputs, which affects the performance of the tool. Jet track information is intrinsically un-  
1649    ordered, and therefore a permutation invariant approach removes this element of arbitrary decision  
1650    making from the modeling process.

1651    The input to ANTELOPE architecture is the same 6 track variables for the leading two jets, as  
1652    presented in Section 7.2.2. The track information is encoded to the PFN  $\mathcal{O}$  event representation  
1653    using the pre-trained  $\Phi$  neural network (trained according to the steps outline in Section 7.2.3). The

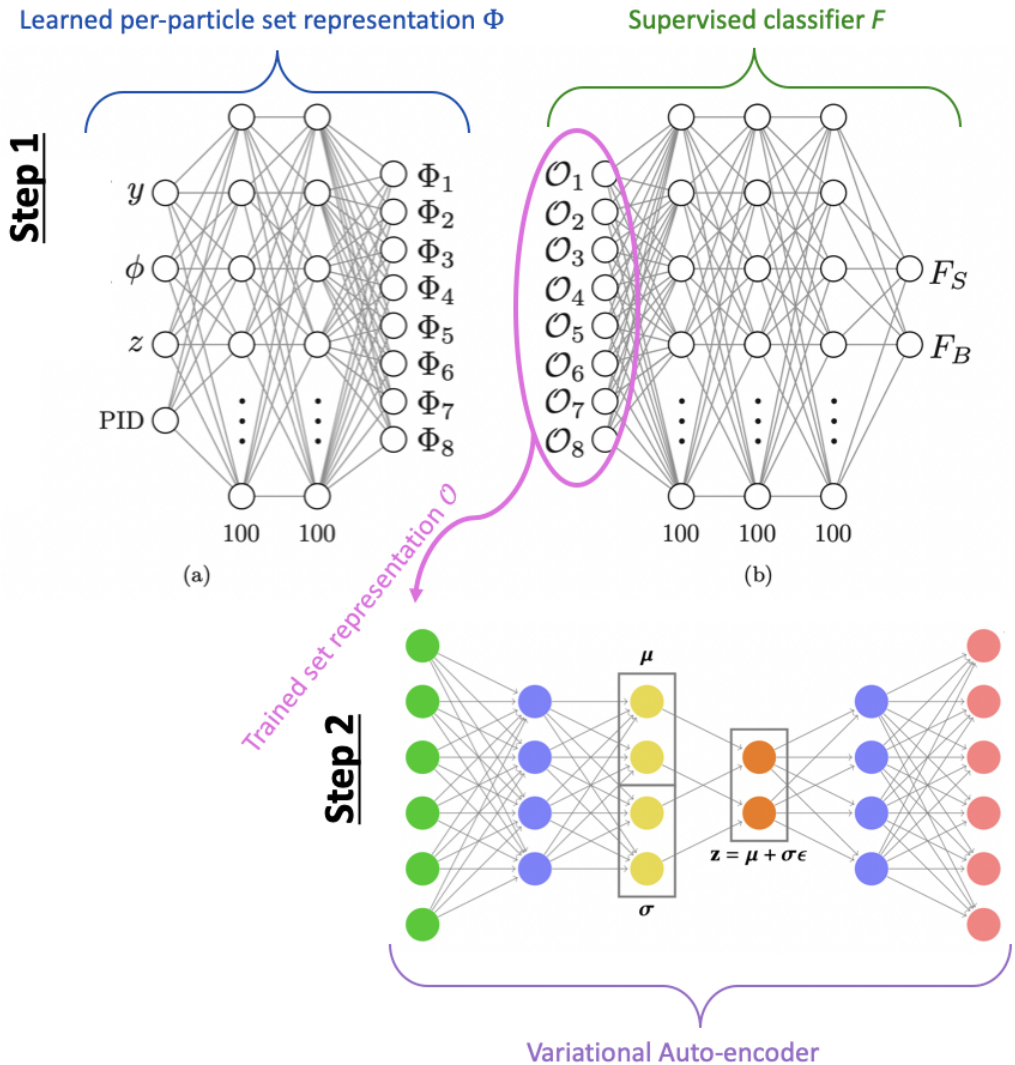


Figure 7.19: An annotated diagram of the ANTELOPE architecture. Step 1 illustrates the PFN which is fully trained before its use in the ANTELOPE network. Step 2 illustrates the variational auto-encoder. The Gaussian sampling of the latent space is shown, illustrating how the VAE differs from the AE shown in Figure 7.4.

1654 VAE is then trained in an *unsupervised* way using inputs encoded to  $\mathcal{O}$  from data events only. Here  
 1655 *unsupervised* means that the VAE is given no knowledge of the signal model during training. There  
 1656 is implicit knowledge of the signal model in the  $\mathcal{O}$  encoding, so the full ANTELOPE network is  
 1657 considered semi-supervised, while the VAE component is unsupervised. A visual example of the  
 1658  $\mathcal{O}$  input to the VAE portion of the ANTELOPE is given in Figure 7.20.

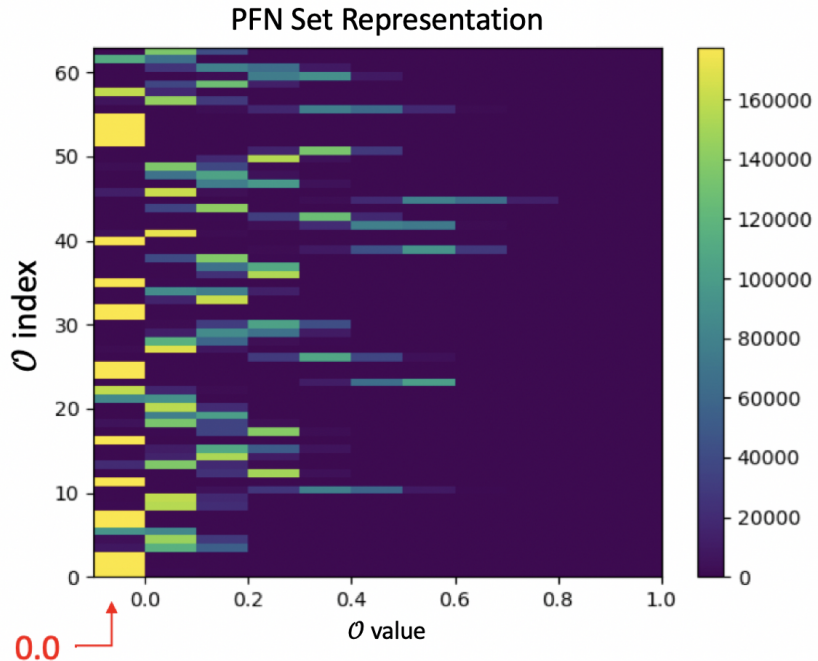


Figure 7.20: A visual representation of the 64 PFN  $\mathcal{O}$  which create the input for the VAE component of ANTELOPE. The plot is 2D histogram of the PFN  $\mathcal{O}$  index (0-63) versus the value assumed by that index. Many entries have a  $\mathcal{O}$  value of exactly 0.0. To visually separate these from entries with a small but non-zero  $\mathcal{O}$  value, any entries with value = 0.0 are moved to value = -0.01 (leftmost column) for the purpose of the plot only.

1659 The VAE is trained to minimize the reconstruction error, or the difference between its input and  
 1660 output layer. This pushes it to uncover patterns in the data, which is predominantly composed of  
 1661 SM processes. Any rare events in the data which present patterns inconsistent with the majority of  
 1662 the data will receive a higher reconstruction error. This error is used to create the anomaly score.

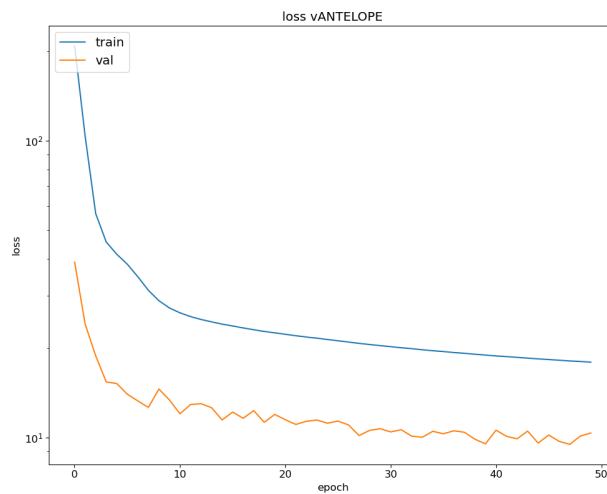
1663 7.3.2 Training

1664 The VAE stage of the ANTELOPE network is trained over 500k data events. The input di-  
1665 mensionality of the VAE has to match the encoded  $\Phi$  dimension of the PFN, in this case 64. The  
1666 encoding portion of the VAE has a hidden layer with 32 nodes, and a latent space dimension of 12.  
1667 The decoding portion has another hidden layer of 32 nodes, and the output layer has a dimension  
1668 of 64 to match the input layer. All layers use a RELU activation [81] except for the output layer  
1669 which uses a SIGMOID activation [81], to restrict the output between 0 and 1. As in the PFN, the  
1670 Adam optimizer [82] [81] is used.

1671 The network is trained for 50 epochs, with a learning rate of 0.00001. The VAE was observed  
1672 to need a very small learning rate to effectively minimize the loss. The loss  $\mathcal{L}$  is the sum of two  
1673 terms, the mean-squared error (MSE) of input-output reconstruction, and the Kullback-Leibler  
1674 divergence (KLD).

$$\mathcal{L} = \sum_i L_i = \sum_i |\Phi_i^2 - \Phi'_{i,i}|^2 + \lambda D_{\text{KL}} \quad (7.3)$$

1675 Figure 7.21 shows the loss during training. The validation events are seen to have a lower loss  
than the training events, indicating there is no issue with overtraining.



1676 Figure 7.21: ANTELOPE architecture loss during training as a function of epoch.

1677 7.3.3 Performance

1678 As with the PFN, the ANTELOPE performance is assessed via the ROC and AUC. Figure 7.22  
 1679 shows the anomaly score and an example ROC curve. The anomaly score is calculated from the  
 1680 loss as defined in 7.3. The score is produced by applying a sigmoid function to the loss to restrict  
 1681 its output between 0.0 and 1.0:

$$a = \frac{1}{1 + e^{-\mathcal{L}}} \quad (7.4)$$

1682 where  $a$  is the anomaly score and  $\mathcal{L}$  is the VAE loss. Because the loss is always positive, the  
 1683 sigmoid transformation effectively restricts the anomaly score range between 0.5 and 1.0. The  
 1684 anomaly score is observed to range between 0.6 and 1.0, as the reconstruction loss is always non-  
 1685 zero. Following a similar sensitivity optimization as presented for the PFN score selection in  
 1686 Section 7.2.4, a selection of **anomaly score > 0.7** is chosen for use in the analysis.

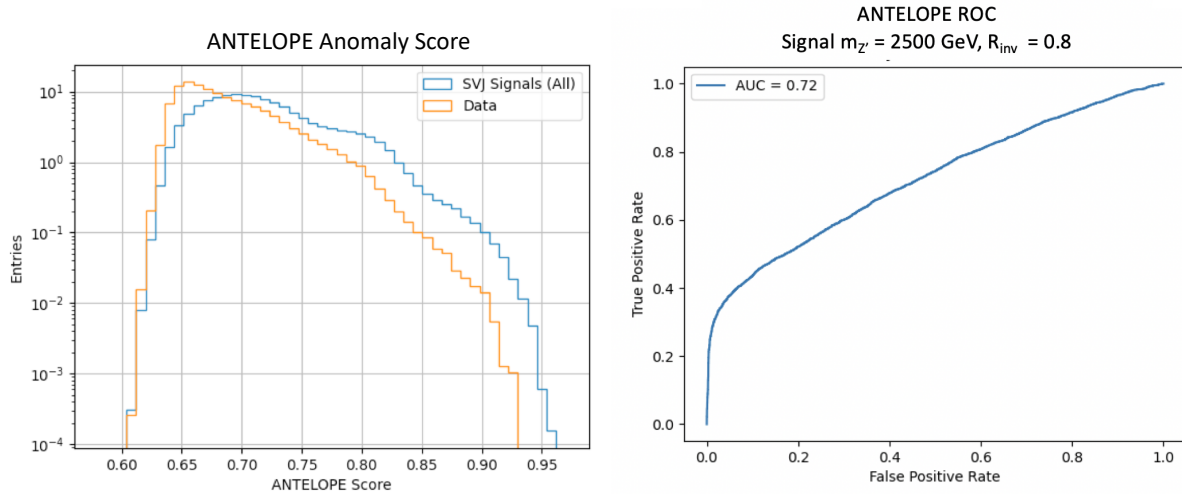


Figure 7.22: Anomaly score distribution (left), comparing all data (orange) and all SVJ signals (blue). The signals have a small but consistently higher score than the data, indicating that they are tagged as more anomalous by ANTELOPE. A ROC curve for an example signal point is also shown (right).

1687 Figure 7.23 shows the AUC of the ANTELOPE across the SVJ signal grid, demonstrating  
 1688 discrimination capability across varying SVJ signal models. Compared to the supervised PFN

1689 method, the ANTELOPE is not as performant (as expected due to the absence of signal model in  
 1690 training). However, the network is seen provide separation between signal and background for all  
 1691 signal points, as evidenced by  $AUC > 0.5$  across the signal grid.

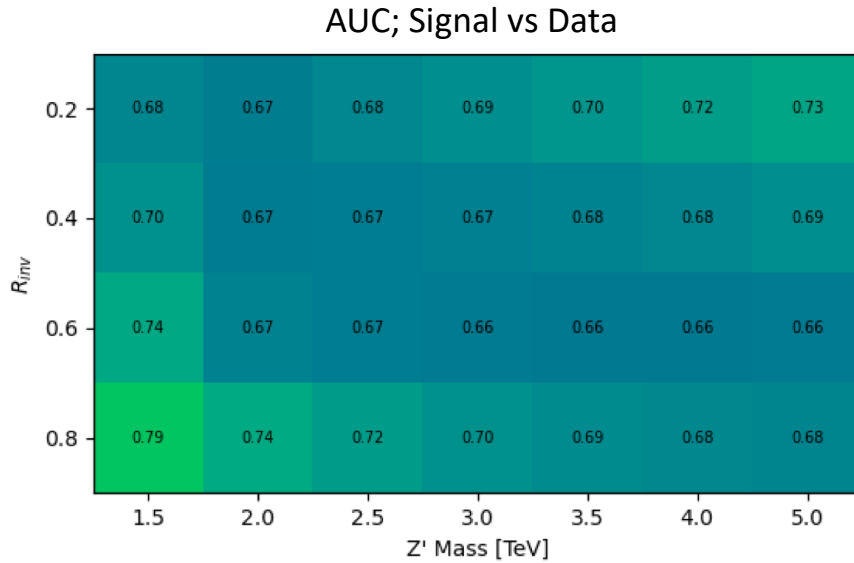


Figure 7.23: AUC from the ANTELOPE score for each signal in the SVJ grid.

1692 **Model Independence** The unsupervised component of training the ANTELOPE network is ex-  
 1693 pected to give it a more generalized sensitivity to new physics with  $E_T^{\text{miss}}$  and jet activity, beyond  
 1694 the scope of the SVJ grid. To assess this, alternative signal models are evaluated with the trained  
 1695 ANTELOPE network.

1696 The following alternate signal models were considered:

- 1697 •  $Z' \rightarrow t\bar{t}$
- 1698 •  $W' \rightarrow WZ$
- 1699 • Gluino pair production  $\rightarrow R\text{-hadron} + \text{LSP}$  ( $E_T^{\text{miss}}$ ) with gluino masses 2000/3000 GeV, LSP  
 1700 mass 100 GeV, and lifetime 0.03 ns (LSP = *lightest supersymmetric particle*)
- 1701 • Emerging jets s-channel with mass 1000 GeV and lifetime 1ns

1702     Figure 7.24 shows the distribution of these signals in the PFN score and the ANTELOPE  
 1703     anomaly score. The benefit of the ANTELOPE in enhancing model independence is clearly seen  
 1704     through the boost in performance for certain non-SVJ signal models. The gluino and emerging  
 1705     jet signals in particular are marked as highly anomalous by the ANTELOPE, but are marked as  
 1706     evenly background-like and signal-like by the PFN. This observation demonstrates that the use  
 1707     of the ANTELOPE network in this analysis has the potential to expand our sensitivity to include  
 1708     alternate signal models that could be marked as highly anomalous with the anomaly score.

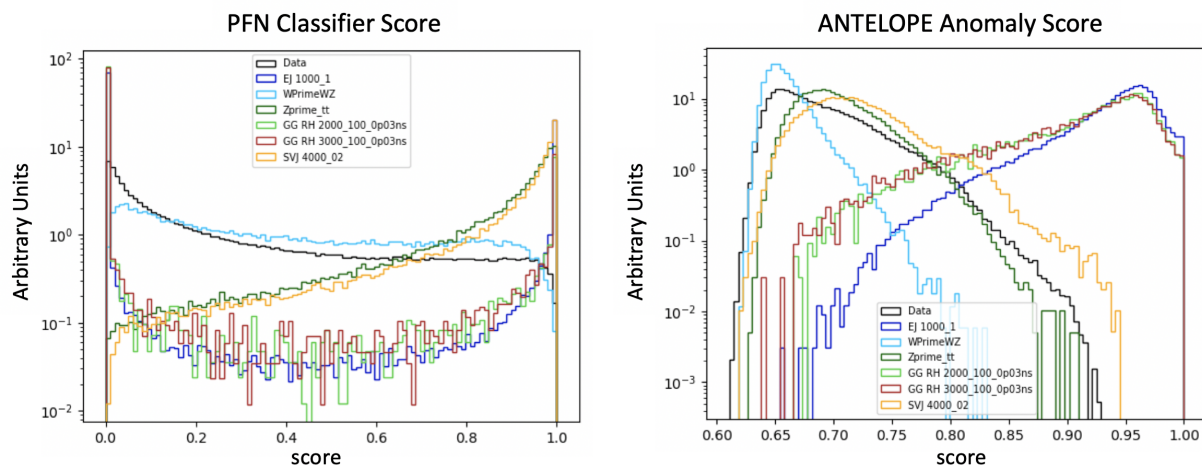


Figure 7.24: Comparing data and the alternate signal models for the PFN score (left) and ANTELOPE score (right). The emerging jet signal (dark blue) and gluino R-hadron signals (red, light green) are an example of the advantage of the model-independent ANTELOPE approach. These signals have a bimodal shape in PFN score but are clearly tagged with a high anomaly score by the ANTELOPE.

1709

1710

## Chapter 8: Analysis Strategy

1711 This chapter will present the strategies used to isolate ATLAS data events most consistent with  
1712 the SVJ model and to estimate the relevant background. The data and MC samples discussed in  
1713 Chapter 6 are studied to create the analysis strategy, and the ML scores discussed in Chapter 7  
1714 are used to isolate the most signal like events. A *preselection* selects events consistent with the  
1715 SVJ topology based on basic features of the jets and  $E_T^{\text{miss}}$ . Preselected events are then split into  
1716 a *control region* (CR), *validation region* (VR), and *signal region* (SR). The CR is used to estimate  
1717 the estimate the background and the VR is used to validate that estimation. The SR is blinded  
1718 during the development of the analysis strategy, and only unblinded to make the final measurements  
1719 presented in Chapter 9. The final result is a polynomial fit of the *transverse mass* ( $m_T$ ) spectrum  
1720 in the SR. The preselection, region definitions, and polynomial fit will be discussed in detail in the  
1721 following sections.

1722 **8.1 Preselection**

1723 The preselection isolates the phase space of events that most closely match the SVJ signal  
1724 topology. Each cut was determined to reduce the background and enhance signal sensitivity. The  
1725 list of preselection cuts and the motivation behind each cut are as follows. Here “jets” refer to  
1726 anti- $k_t$  R=0.4 jets, as discussed in Chapter 5.

- 1727
- At least 2 jets; in order to reconstruct the resonance mass

1728

  - Leading jet ( $j_1$ )  $p_T > 450$  GeV; to ensure the trigger is fully efficient

1729

  - Subleading jet ( $j_2$ )  $p_T > 150$  GeV; to mitigate the presence of non-collision background  
(Appendix B.5.1)

- 1731 •  $|\eta_{j1,j2}| < 2.1$ ; to ensure jets are fully within the tracker
- 1732 •  $\Delta Y < 2.8$  (difference in rapidity between  $j_1$  and  $j_2$ ); to ensure central production associated  
1733 with the hard scatter
- 1734 •  $E_T^{\text{miss}} > 200 \text{ GeV}$ ; to restrict the phase space to events with possible dark particles
- 1735 •  $m_T > 1.2 \text{ TeV}$ , to ensure a smoothly falling  $m_T$  distribution for fitting (Section 8.4)
- 1736 • At least 3 tracks for each of the two leading jets  $j_1$  and  $j_2$ ; to have adequate information  
1737 about the shape of the jet for the ML tools
- 1738 •  $\Delta\Phi(j_1, j_2) > 0.8$ ; to mitigate the presence of non-collision background (Appendix B.5.1).

Table 8.1 shows the impact of these cuts in sequence for data and signal.

Data			Signals - All		
Cut	Statistics	Rel. Efficiency	Cut	Statistics	Rel. Efficiency
Initial	1.71E+10		Init	6.66E+05	
Trigger	3.45E+08	0.02	Trigger	2.83E+05	0.42
N. jets $\geq 2$	2.84E+08	0.82	N. jets $\geq 2$	2.80E+05	0.99
Leading Jet Pt $> 450 \text{ GeV}$	1.49E+08	0.52	Leading Jet Pt $> 450 \text{ GeV}$	2.21E+05	0.79
Lead Jet Eta $< 2.1$	1.42E+08	0.95	Lead Jet Eta $< 2.1$	2.19E+05	0.99
Subleading Jet Eta $< 2.1$	1.33E+08	0.94	Subleading Jet Eta $< 2.1$	2.12E+05	0.97
$dY < 2.8$	1.29E+08	0.96	$dY < 2.8$	2.11E+05	0.99
MET $> 200 \text{ GeV}$	7.07E+05	0.01	MET $> 200 \text{ GeV}$	1.13E+05	0.54
$m_T > 1200 \text{ GeV}$	5.38E+05	0.76	$m_T > 1200 \text{ GeV}$	7.94E+04	0.70
Jet2 pT $> 150 \text{ GeV}$	5.03E+05	0.93	Jet2 pT $> 150 \text{ GeV}$	6.14E+04	0.77
$d\Phi(j_1, j_2) > 0.8$	4.97E+05	0.99	$d\Phi(j_1, j_2) > 0.8$	5.83E+04	0.95

Table 8.1: Preselection cuts for data (left) and signal (right).

1739

1740 With the exception of the cuts necessary to reduce the non-collision background, all cuts were  
1741 verified to enhance signal sensitivity by improving  $s/\sqrt{b}$ , a standard estimate of discovery sensi-  
1742 tivity, where  $s$  is the number of signal events and  $b$  is the number of background events. The cuts  
1743 on  $\Delta Y$  and  $E_T^{\text{miss}}$  were optimized to enhance  $s/\sqrt{b}$ , and the other cuts were informed by the physics  
1744 motivations provided above.

1745 Vets are applied to reject any events where an error for a subdetector is flagged. To reject  
1746 non-collision backgrounds (NCB), such as calorimeter noise, beam halo interactions, or cosmic

rays, the standard ATLAS event cleaning procedure is applied. As this analysis is very dependent on  $E_T^{\text{miss}}$  associated to jets, the TIGHT [85]event cleaning working point is applied. Tight cleaning requires jets to pass a stricter set of quality requirements compared to the LOOSE [85] cleaning option. Due to the alignment between jets and  $E_T^{\text{miss}}$  for SVJ events, it was found that two additional cuts (indicated above) are needed to remove NCB. The process for selecting these cuts is presented in Appendix B.5.1.

The leading and subleading jets in each event are considered the dark quark candidates from the  $Z' \rightarrow q_D q_D$  decay. They are therefore the two jets of greatest interest in the event, and used in the computation of key analysis variables. This choice was determined through studies of the dark quark trajectory in simulation which determined that the leading and subleading jets are most often aligned with the dark quark, and therefore most likely to capture the dark quark hadronization. This study can be found in Appendix C.

Figure 8.1 and Figure 8.2 show the distribution of signal and background MC in several key analysis variables after preselection is applied.

## 8.2 SVJ Fit and Discovery Analysis Strategies

As was introduced in Chapter 7 this analysis is interested in achieving dual goals: to make the best possible measurement of the SVJ signal model generated for this analysis, and to broadly search for any signals consistent with dark QCD behavior and inconsistent with a Standard-Model-only background hypothesis. To this end, two parallel analysis strategies are developed.

The SVJ Fit strategy uses the supervised PFN ML score in defining the signal region. Recall, the PFN is trained over simulated MC background and a combination of all MC SVJ signals. This gives this ML tool high sensitivity to the particular nuances of the SVJ shower predicted by the modeled theory. In addition to using the supervised ML tool, the SVJ Fit analysis strategy sets limits on the expected cross-section of each signal point in the SVJ signal grid. To achieve this, the shape of the SVJ signals are considered in the final fit, as will be elaborated on Section 8.5.1. The combination of the supervised PFN ML score and the signal-shape sensitive fitting strategy allows

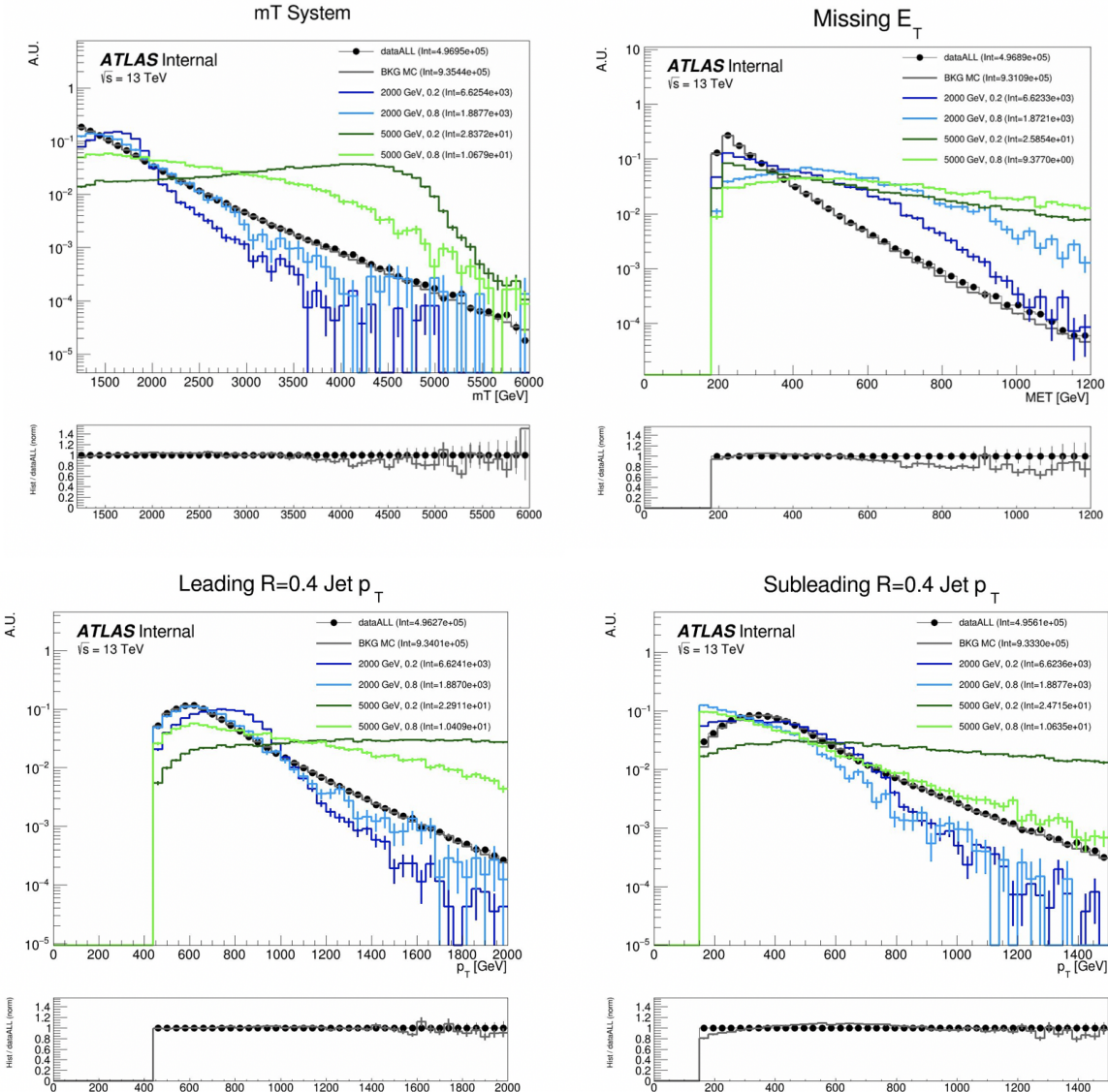


Figure 8.1: Energy and momentum analysis variables at preselection, for data, all background MC and representative signal models.  $m_T$  is the key fit variable, and this plot illustrates the smoothly falling background in comparison to the resonant shape of the signals.  $m_T$  is further illustrated in Figure 8.8.

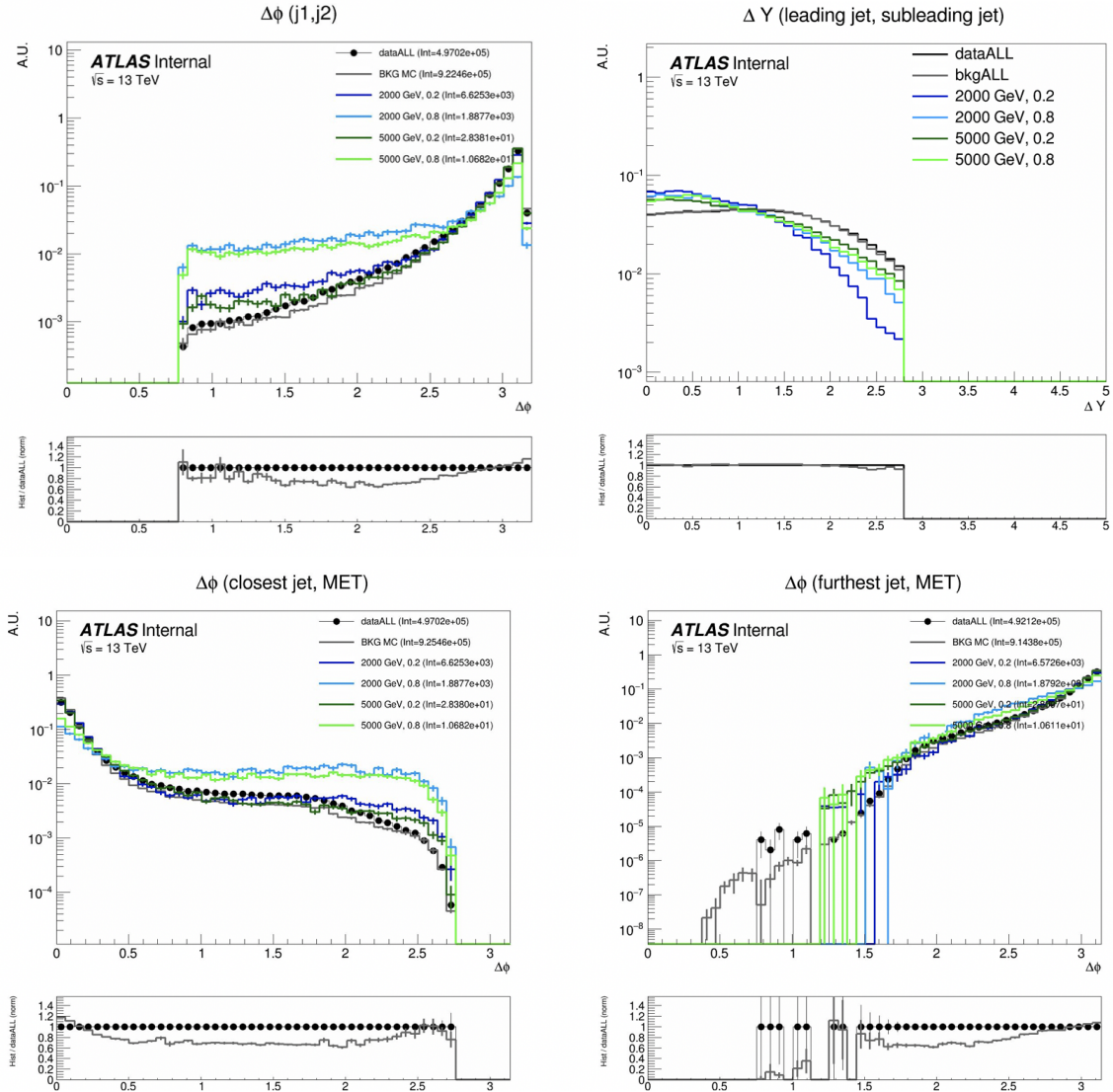


Figure 8.2: Orientation analysis variables at preselection, for data, all background MC and representative signal models. While  $\Delta\phi(E_T^{\text{miss}}, j)$  variables are not used explicitly in the analysis flow, they help create a picture of the event.

for the greatest possible sensitivity to the modeled signal process, thus allowing the analysis the best chance at discovery of this model, or enabling the analysis to set the best possible limits on the observed cross-section.

In contrast, the Discovery analysis strategy attempts to design a more general search, which could be sensitive to SVJs, but also to other possible hidden valley dark QCD models, such as fully dark jets or emerging jets [21]. The Discovery analysis strategy uses the semi-supervised ANTELOPE ML score in defining the signal region. Recall, the ANTELOPE is trained over ATLAS data only, with no explicit knowledge of the SVJ signal behavior. The Discovery fit strategy is also signal model agnostic, by employing a bump hunt [86] strategy, which searches a smoothly falling template for any bumps inconsistent with a background only hypothesis. Therefore any signal which could present a resonant signature in  $m_T$  could show up as an excess in this strategy.

The details of both strategies will be explored in the follow sections which detail the design of the signal regions and fit strategies. A diagram demonstrating the analysis flows can be seen in

Figure 8.3. Details on each selection and region can be found in the following subsections.

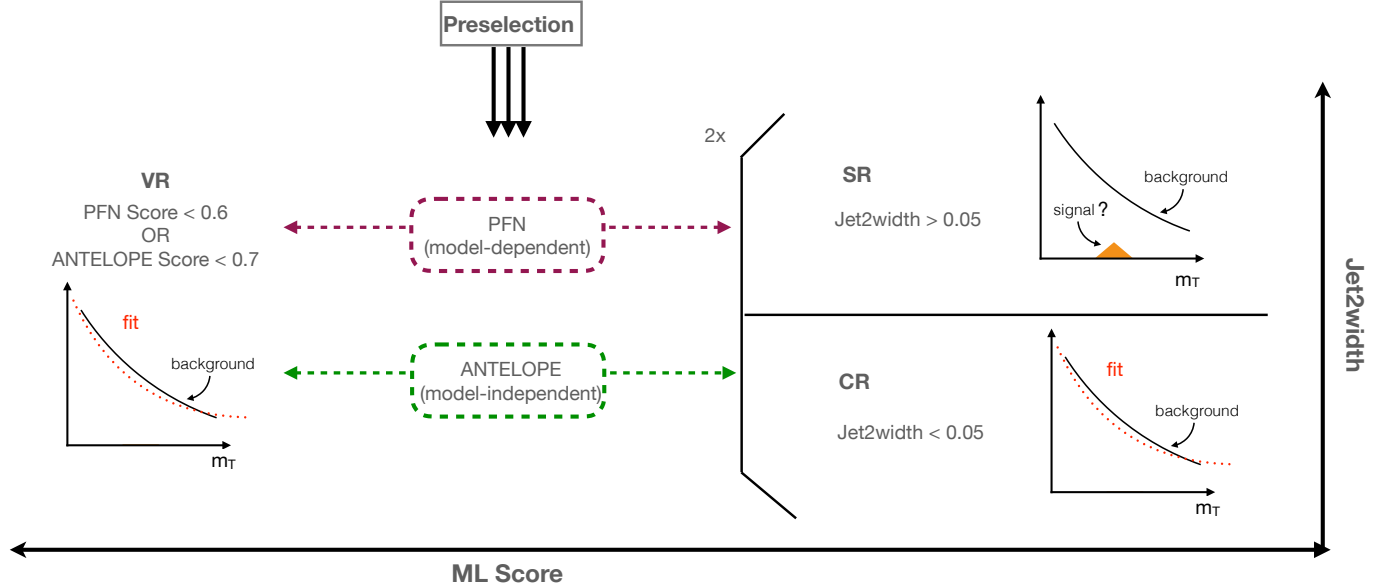


Figure 8.3: Flow of analysis selections, regions, and background estimation/validation fitting strategy. TODO: diagram needs to be corrected

1787 **8.3 Analysis Regions**

1788 **8.3.1 Control and Validation Regions**

1789 The final background estimation will come from a polynomial fit to the  $m_T$  distribution in the  
1790 signal region. The control and validation regions are needed to develop and test this fit in data.

1791 To define the CR selection, a variable is needed that isolates background from all signals across  
1792 the  $(R_{inv}, m_Z)$  grid, which is challenging due to the varying nature of the signal models in quantities  
1793 such as  $E_T^{\text{miss}}$  and  $p_T$  balance, as illustrated in Figure 8.1. The variable *jet width* is chosen, which  
1794 is the calorimeter measurement of the width of a small-R jet as defined by the distance between  
1795 the cluster and the jet axis scaled by the jet energy [87]. Figure 8.4 shows this variable specifically  
1796 for the subleading jet width, in data, background MC and signal at preselection. The leading jet  
1797 width, which was determined to be less useful for isolating signal from background is also shown.  
1798 The subleading jet is more likely to be the jet aligned with MET, which is why the signal jet width  
1799 is consistently wider in the subleading jet, but not the leading jet. A selection of  $\text{width}_{j2} < 0.05$  is  
1800 chosen for the CR, with the VR and SR therefore having a selection of  $\text{width}_{j2} \geq 0.05$ .

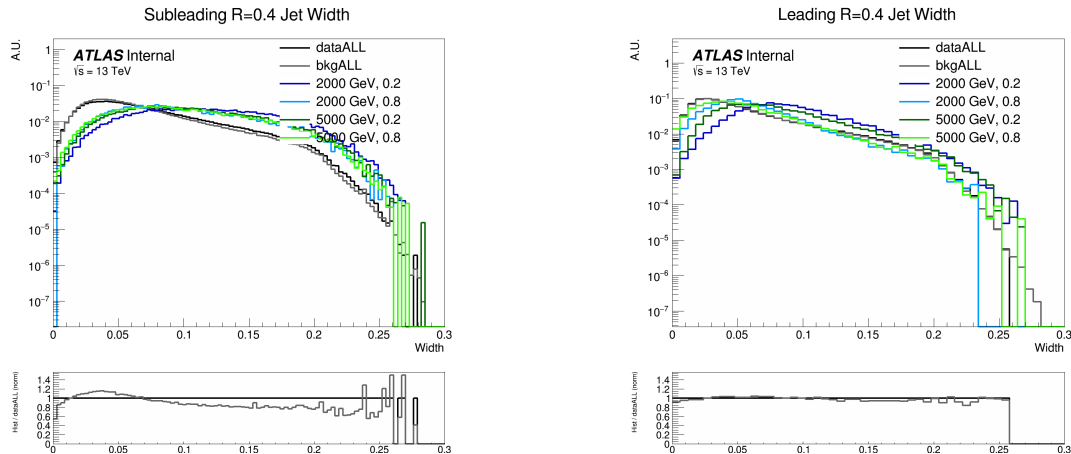


Figure 8.4: Distributions of the subleading jet width  $\text{width}_{j2}$  (left) and leading jet width  $\text{width}_{j1}$  (right) in data, background MC and signals at preselection. All SVJ signals are seen to be wider than the background in  $\text{width}_{j2}$ . The same is not true for  $\text{width}_{j1}$ , where some signals are observed to closely match the background.

1801 While the CR was used to develop the polynomial strategy, and is the primary region used in

many of the fit studies, a validation region is used as an additional check of the estimation strategy  
 in data. The VR is defined using the region of events with low ML score by either the PFN or  
 ANTELOPE networks. Here the analysis strategy splits into the two parallel strategies presented  
 in Section 8.2: the SVJ fit strategy and the Discovery strategy. A selection of [PFN score  $\leq 0.6$   
 $\& \text{width}_{j2} \geq 0.05$ ] defines the SVJ Fit VR, while [ANTELOPE score  $\leq 0.7$  & width $_{j2} \geq 0.05$ ]  
 defines the discovery VR.

There are therefore three variables that are crucial to the analysis strategy: width $_{j2}$ , ML score,  
 and  $m_T$ . Figure 8.5 shows the correlations of all three variables to one another. Any outstanding  
 correlations are shown in Figure 8.6 to not sculpt the  $m_T$  distribution and only affect its slope,  
 making these variables trustworthy for extrapolation across background/signal regions and final  
 fitting procedures.

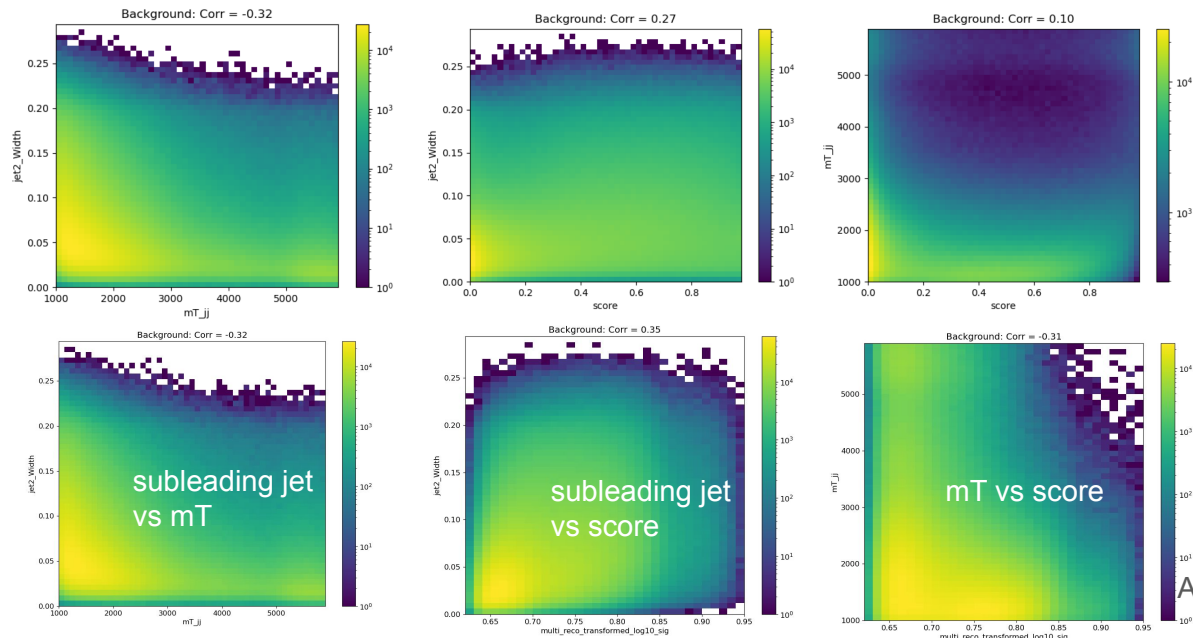


Figure 8.5: 2D plots revealing correlations between width $_{j2}$  and  $m_T$  (left), width $_{j2}$  and ML score (middle), and  $m_T$  with ML score (right). For the top row, the ML score is the PFN score, and for the bottom three, the ML score is the ANTELOPE score. Minimal correlations are observed and are shown to not sculpt  $m_T$ , validating these variables for analysis region construction and statistical treatment.

The most important variable for shape robustness across the CR, VR, and SR is  $m_T$ , as this  
 is the variable that is fit for the statistical results. Figure 8.6 shows the distribution of  $m_T$  across

1815 the CR, VR, and SR, for both the PFN (supervised) and ANTELOPE (semi-supervised) strategies.  
 1816 Some slope is observed in the ratio of the CR to the VR/SR shapes; however, the chosen back-  
 1817 ground estimation strategy of polynomial fitting is expected to accommodate this slope. Further,  
 1818 the ability of the background polynomial to fit both tail shapes will flex the fit framework in a  
 1819 way that will generate higher confidence in the final ability to fit the SR. No significant bumps or  
 sculpting are observed.

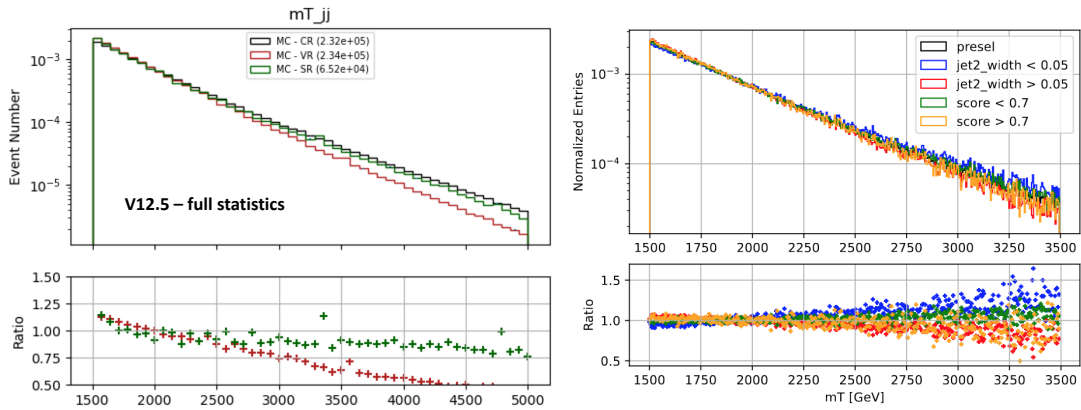


Figure 8.6:  $m_T$  in simulation across the CR, VR, and SR for both PFN (left) and ANTELOPE (right) selections.

1820

### 1821 8.3.2 Signal Region

1822 A selection of PFN score  $> 0.6$  in the SVJ Fit region and ANTELOPE score  $> 0.7$  in the  
 1823 Discovery region is made to provide the primary signal-to-background enrichment, as motivated  
 1824 by Section 7.2. These values are determined to maximize  $s/\sqrt{b}$  in each region. The additional  
 1825 selection of  $\text{width}_{j2} \geq 0.05$  orthogonalizes the SR to the CR. Note that the PFN and ANTELOPE  
 1826 regions are not orthogonal; this is because the two analysis flows serve different purposes, their  
 1827 statistical treatments are different, and they will not be combined.

1828 A summary of the SR, CR, and VR definitions can be seen in Figure 8.7, along with the relative  
 1829 data statistics in each region.

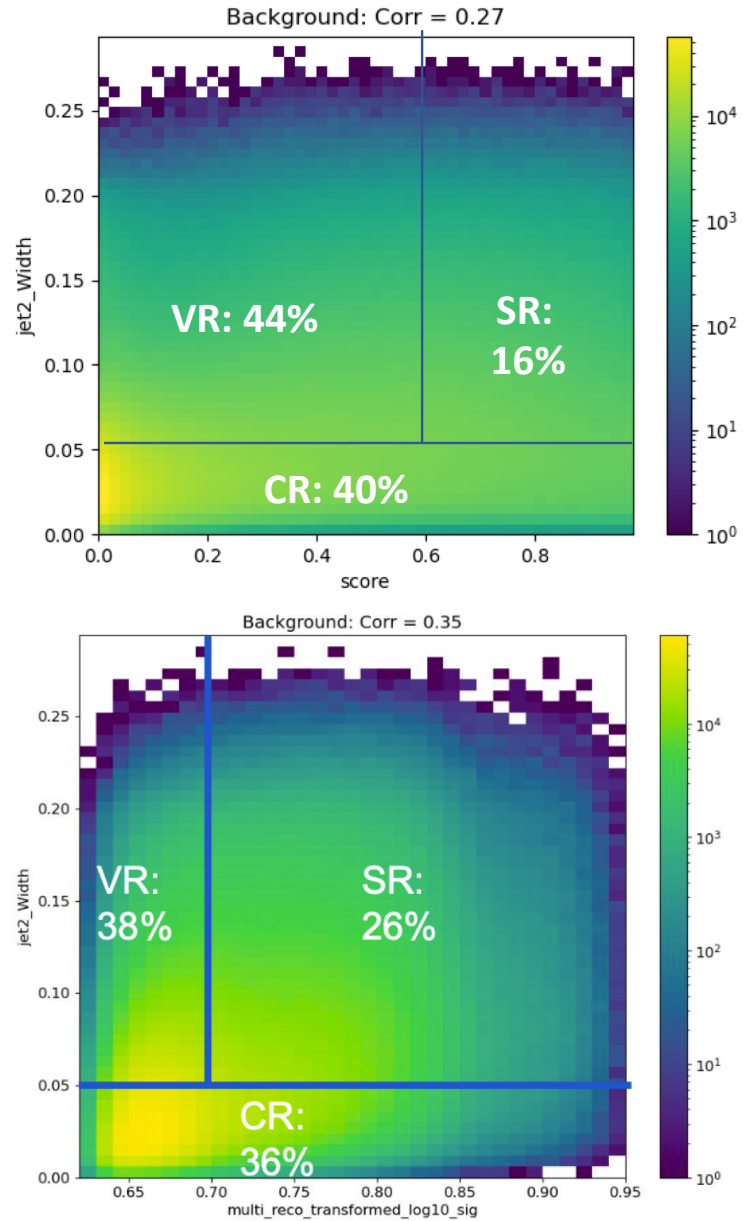


Figure 8.7: Definition of CR, VR, and SR regions using  $\text{width}_{j2}$  and the ML score, along with the population of each region in data statistics. The SVJ Fit region is shown on top with the PFN score on the x-axis, and Discovery region is shown on the bottom, with the ANTELOPE score on the x-axis.

## 1830 8.4 Background Estimation

1831 The transverse mass  $m_T$  is chosen as the search variable due to the potential for the SVJ signal  
 1832 to create a resonant shape around the mass of the  $Z'$ .  $m_T$  is the total transverse mass of the two  
 1833 leading jets and the  $E_T^{\text{miss}}$ , expressed in Equation 8.1 as:

$$m_T^2 = [E_{T,jj} + E_T^{\text{miss}}]^2 - [\vec{p}_{T,jj} + \vec{p}_T^{\text{miss}}]^2 \quad (8.1)$$

1834 where  $E_{T,jj}$  is the transverse energy of the dijet system. We take  $E_{T,jj} = m_{jj}^2 + |\vec{p}_{T,jj}|^2$ , where  
 1835  $m_{jj}^2$  is the invariant mass of the two leading jets, and  $\vec{p}_{T,jj}$  is the vector sum of the  $p_T$  of the two  
 1836 leading jets.  $m_T$  is selected as the search variable in place of simpler invariant mass  $m_{jj}$  because  
 1837 substantial energy from the  $Z'$  decay is captured in the  $E_T^{\text{miss}}$ . Therefore incorporating  $E_T^{\text{miss}}$  into  
 1838  $m_T$  improves the resonance around the mass of the  $Z'$ .

Figure 8.8 illustrates the resonance in  $m_T$  of the SVJ signals.

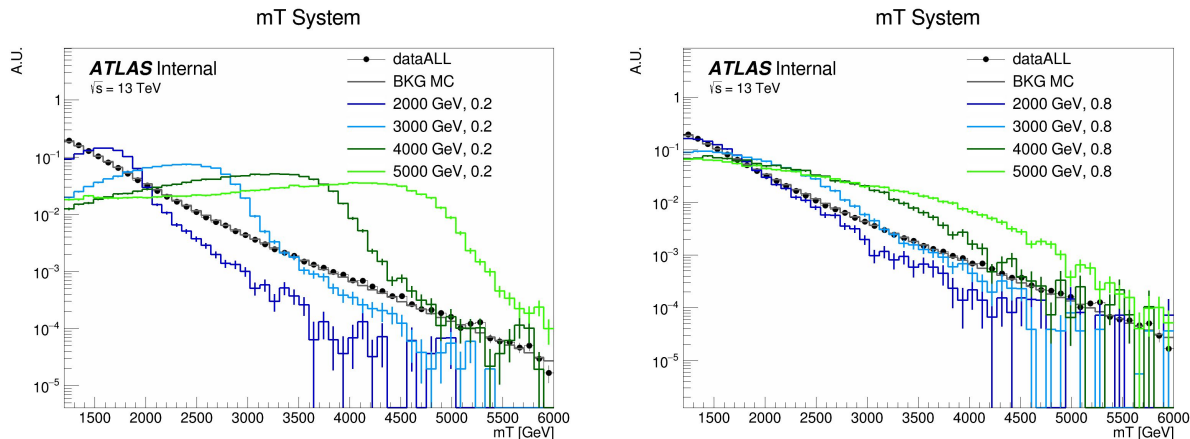


Figure 8.8: The resonant shape of the SVJ signals in  $m_T$ , in contrast to the smoothly falling  $m_T$  background. The high  $R_{\text{inv}}$  signals (right) boast a wider shape, making them more difficult to detect, while the low  $R_{\text{inv}}$  signals (left) produce a more narrow resonance in  $m_T$ .

1839  
 1840 The SM background in the SR is predominantly composed of QCD events, and due to the poor  
 1841 modeling of QCD at high energies by MC, it is estimated in a fully data-driven way. An empirical  
 1842 functional form is used for the background shape of  $m_T$ . The ability of this function to model  
 1843 the background behavior is tested both the CR and the VR for each analysis strategy. The shape

1844 parameters are left free in all the fits.

1845 The fits are performed for  $1500 \text{ GeV} < m_T < 6000 \text{ GeV}$ . The polynomial chosen is a standard

1846 5-parameter function used in several similar dijet search analyses such as [88] [89] [70] and shown

1847 in Equation 8.2:

$$f(x) = p_1(1 - x)^{p_2}x^{p_3+p_4\ln x+p_5\ln^2 x} \quad (8.2)$$

1848 Here  $x = m_{jj}/\sqrt{s}$  and the  $p_i$  are free parameters. The fit function is required to be fully positive, and

1849 the  $m_T$  distribution is fit to 90 even-width bins. The resulting fit shape is used as the background

1850 estimation for both the SVJ Fit strategy and the Discovery strategy. Validation of the fit and its

1851 ability to both model the background and detect signal are shown in Section 8.5. Higher order

1852 polynomials were also considered, but an F-test was performed and the five parameter function

1853 was determined to be adequate and optimal for capturing the shape of the background.

## 1854 **8.5 Fit Strategy and Validation**

1855 The steps taken to validate the fitting approach for both the SVJ Fit strategy and the Discovery

1856 strategy will be outlined in the following sections. The signal region fits which comprise the final

1857 result will be presented in Chapter 9.

### 1858 **8.5.1 SVJ Fit Strategy**

1859 The ability of the five parameter fit function to capture the shape of the background is studied

1860 extensively, using data from the CR and VR. Signal injection tests are performed to determine the

1861 ability of the fit to recover and quantify any SVJ signal excess. Estimates of the expected sensitivity

1862 and the ability to set upper limits on the cross-section of the signal process are also verified.

### 1863 **Background Only Fits**

1864 Three validations are used for the background fit polynomial: MC across all analysis regions,

1865 data in the CR and VR, and pseudo-data in the CR and VR.

1866      Figure 8.9 shows the ability of this polynomial to fit the smoothly falling  $m_T$  background in  
 1867    simulation across all 3 analysis regions (CR, VR, SR). The  $m_T$  spectrum is fit in 90 even bins.  
 1868    These distributions are obtained by downsampling the MC statistics to match the relevant statis-  
 1869    tics of the data region, in accordance with the MC weights. The high background-only  $p$ -value  
 indicates a good fit.

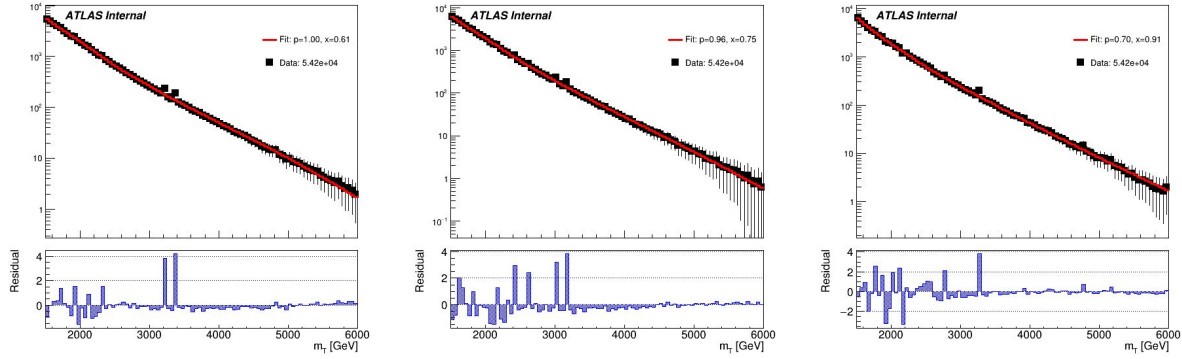


Figure 8.9: Background-only  $m_T$  fits using representative MC in the CR (left), VR (middle), and SR (right).

1870  
 1871    A slight sinusoidal pattern in the residuals may be observed. This arises due to the “stitching”  
 1872    of the  $p_T$  slices for the QCD MC (as shown in Figure 6.2), which is picked up by the fit. For this  
 1873    reason, fitting to MC is only checked to verify that the differences in the slope of  $m_T$  between the  
 1874    three regions (as shown in Figure 8.6) do not pose a problem for the fitting strategy.

1875    The nature of the functional fitting method allows it to easily adapt to changes in slope of a  
 1876    smoothly falling distribution. Thus validation of the fit can be performed in data using the CR and  
 1877    the VR distributions to model the expected behavior in the SR. Figure 8.10 shows the a successful  
 1878    fit performed on the full statistics CR and VR regions.

1879    Table 8.2 shows the post-fit values of the fit parameters and their uncertainties for each fit.  
 1880    To further validate the fit stability of the fit against potential statistical fluctuations, *pseudo-data*  
 1881    (also known as *toy datasets*) are created from the CR data distribution. The pseudo-data is created  
 1882    following an *Asimov* prescription [90], using a template to generate a set of toys representing  
 1883    different possible statistical fluctuations. When studied as a group, the performance of the pseudo-  
 1884    data collection represents the range of possible behavior for an unknown distribution (the SR data

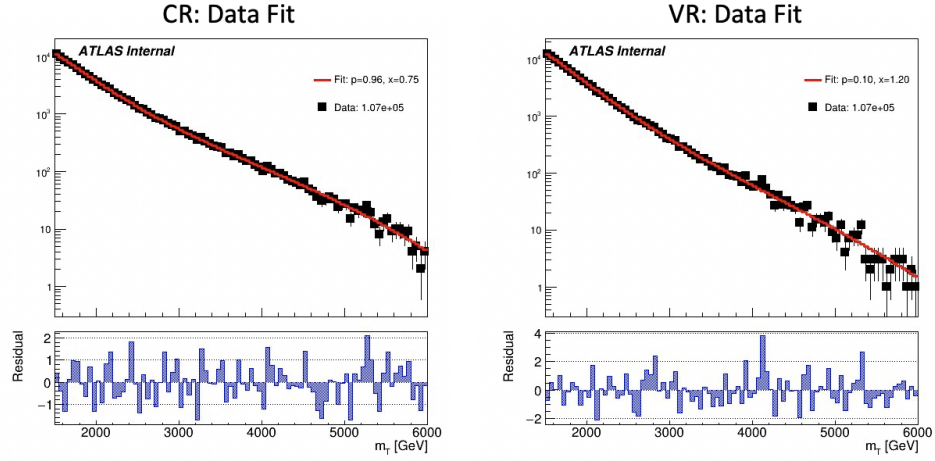


Figure 8.10: Background-only  $m_T$  fits using data in the full statistics CR and VR regions.

Parameter	CR		VR	
	Value	Error	Value	Error
p1	1.0716e+05	4.64e+02	1.0686e+05	4.63e+02
p2	4.2479e+01	2.97e+00	3.4279e+01	3.71e+00
p3	5.3888e+01	3.81e+00	4.0798e+01	4.50e+00
p4	2.3804e+01	1.47e+00	1.9424e+01	1.71e+00
p5	3.6683e+00	2.18e-01	3.1583e+00	2.51e-01

Table 8.2: Post-fit parameters for the PFN CR and VR.  $p1$  can also be considered  $N_{bkg}$  or the normalization factor.

1885 in this case), given its statistical uncertainties.

1886 The template used to generate the pseudo-data is a *smoothed* and *scaled* version of the CR.

1887 The smoothing applied follows the procedure for functional decomposition described in Ref. [91].

Figure 8.11 shows the impact of smoothing on the source data distribution in the CR.

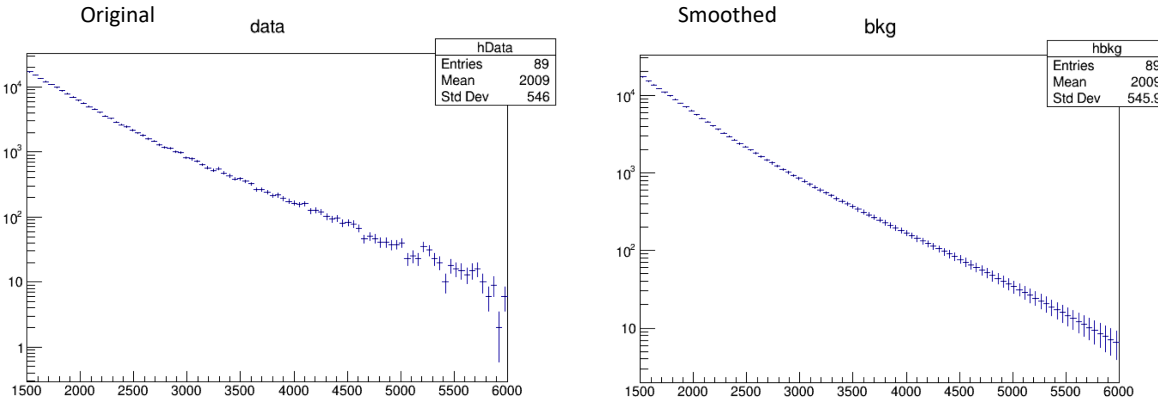


Figure 8.11:  $m_T$  distribution in the data CR, before (left) and after (right) smoothing.

1888

1889 The scaling adjusts the statistics of the smoothed template to the expected statistics of the SR.

1890 Recall Figure 8.7, which illustrates that the statistics of the CR and the VR are almost 3x the

1891 expected statistics of the SR. The polynomial fitting strategy is sensitive to the statistics of the

1892 fitted template, so its performance can very substantially depending on the statistical power of the

1893 fitted distribution. To mitigate this, the smoothed template is scaled to the expected statistics of

1894 the SR. Toys are then generated from the smoothed distribution, by varying each bin within its

1895 statistical uncertainty according to a Poisson distribution. Each toy has the same statistical power

1896 as the SR, within statistical uncertainty.

1897 Figure 8.12 shows example fits to three such toy datasets. Figure 8.13 shows the resulting

1898 p-values after an ensemble of 100 Asimov pseudo-datasets are each individually fit. This test

1899 determines the likelihood of exceptionally good (high p-value) or poor (low p-value) fits due to

1900 randoms statistical fluctuations in the data. A flat distribution is observed, indicating good statisti-

1901 cal behavior.

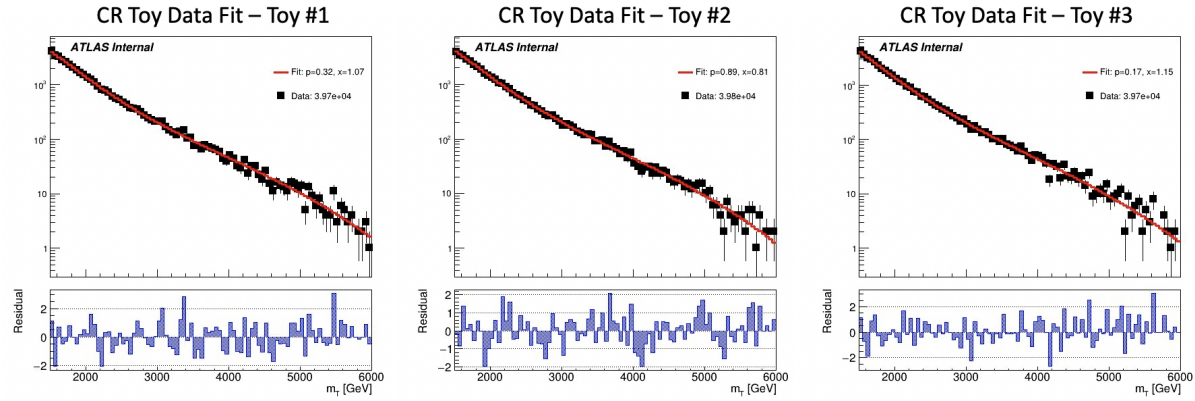


Figure 8.12: Background-only  $m_T$  fits using pseudo-data from the CR template.

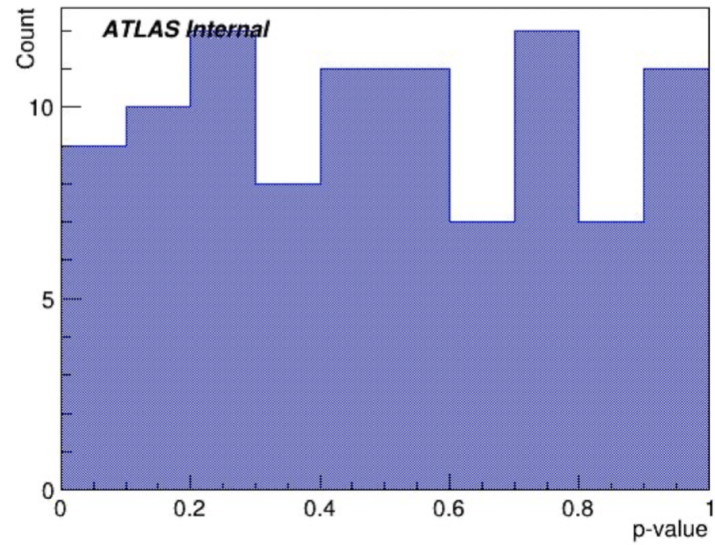


Figure 8.13:  $p$ -value histograms from 100 fits to Asimov data in the CR.

1902 **Signal + Background Fits**

1903 Figure 8.14 shows an example of an injected signal into the exclusion region  $m_T$  spectrum, and  
the ability of the fit framework to accurately fit the number of signal events.

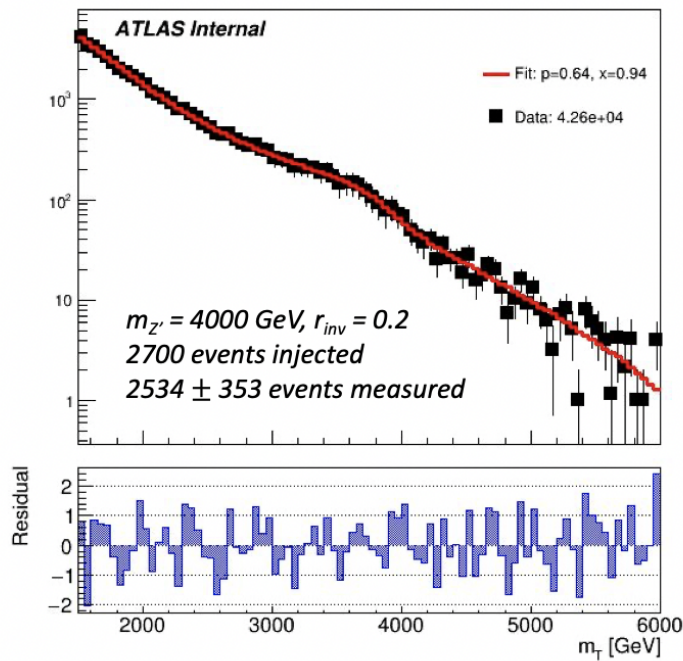


Figure 8.14: Example S+B fit on a background  $m_T$  spectrum with injected signal from the point ( $4000 \text{ GeV}$ ,  $R_{inv}=0.2$ ).

1904  
1905 Signal injection tests demonstrate the a linear relationship between the amount of signal in-  
1906 jected and the amount of signal measured by the fit. The signal injection tests are performed in  
1907 Asimov datasets to counter the impact of statistical fluctuations in any given template. 50 Asimov  
1908 trials are run for all signal points across  $Z'$  mass and  $R_{inv}$ .

1909 Figure 8.15 provides the results of these tests. The uncertainty of the measurement varies  
1910 according to the  $Z'$  mass, due to the larger relative background for lower mass points. However,  
1911 a strong linear relationship between amount of signal injected and amount of signal measured is  
1912 observed for all signal points, which is the key feature.

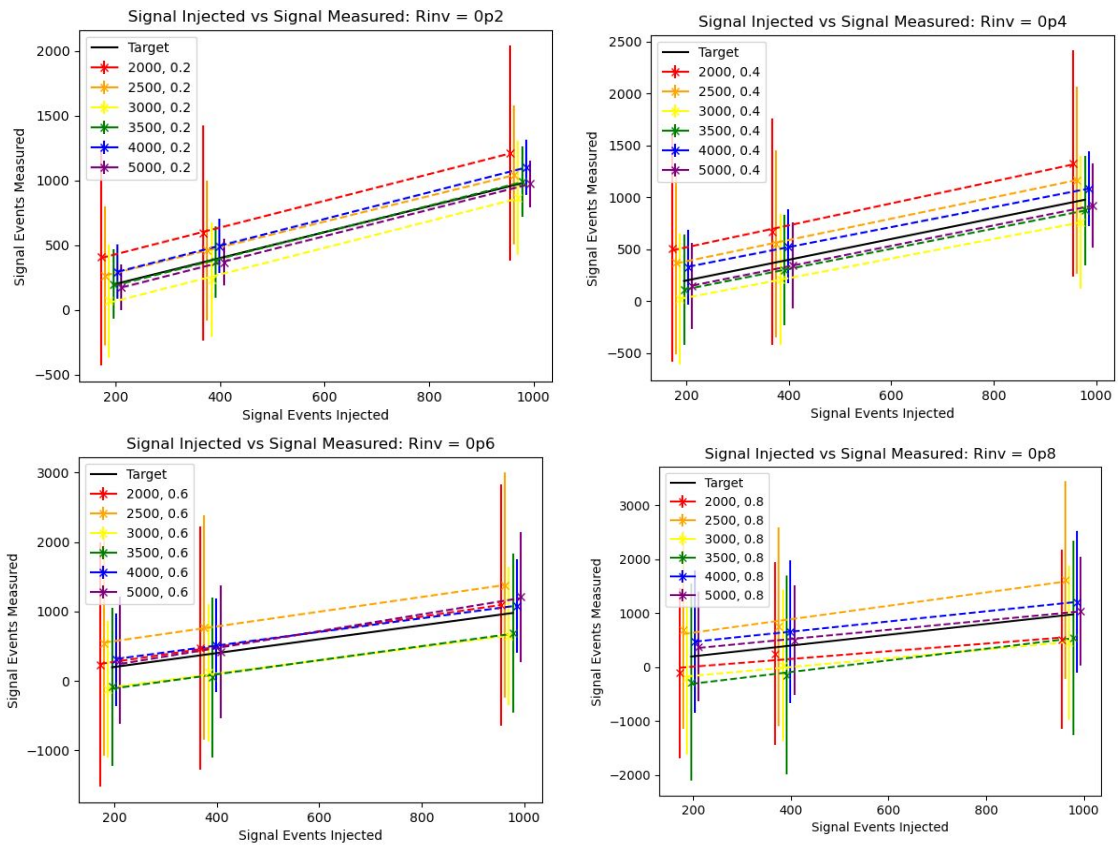


Figure 8.15: Measured signal at a variety of injected values ( $1x$ ,  $2x$ , and  $5x\sqrt{b}$ ), for all signal points in the grid,  $R_{inv}=0.2$  (top left),  $0.4$  (top right),  $0.6$  (bottom left), and  $0.8$  (bottom right).

## 1913 Expected Sensitivity

1914 Limits on the signal process are obtained by determining the cross section of the signal that can  
 1915 be excluded to 95% confidence. Figure 8.16 shows the expected limits obtained from an average  
 1916 of 50 Asimov data fits. The limits shown do not include systematics uncertainties in the fit, the  
 1917 impacts of which are discussed in Chapter 9.

1918 Considerable exclusion power is predicted for low  $R_{inv}$  signal points and lower mass points.  
 1919 Higher  $R_{inv}$  points present more difficulty due to the very broad signal bump. Higher  $Z'$  mass  
 1920 points are more difficult to exclude due to the low theory cross-sections.

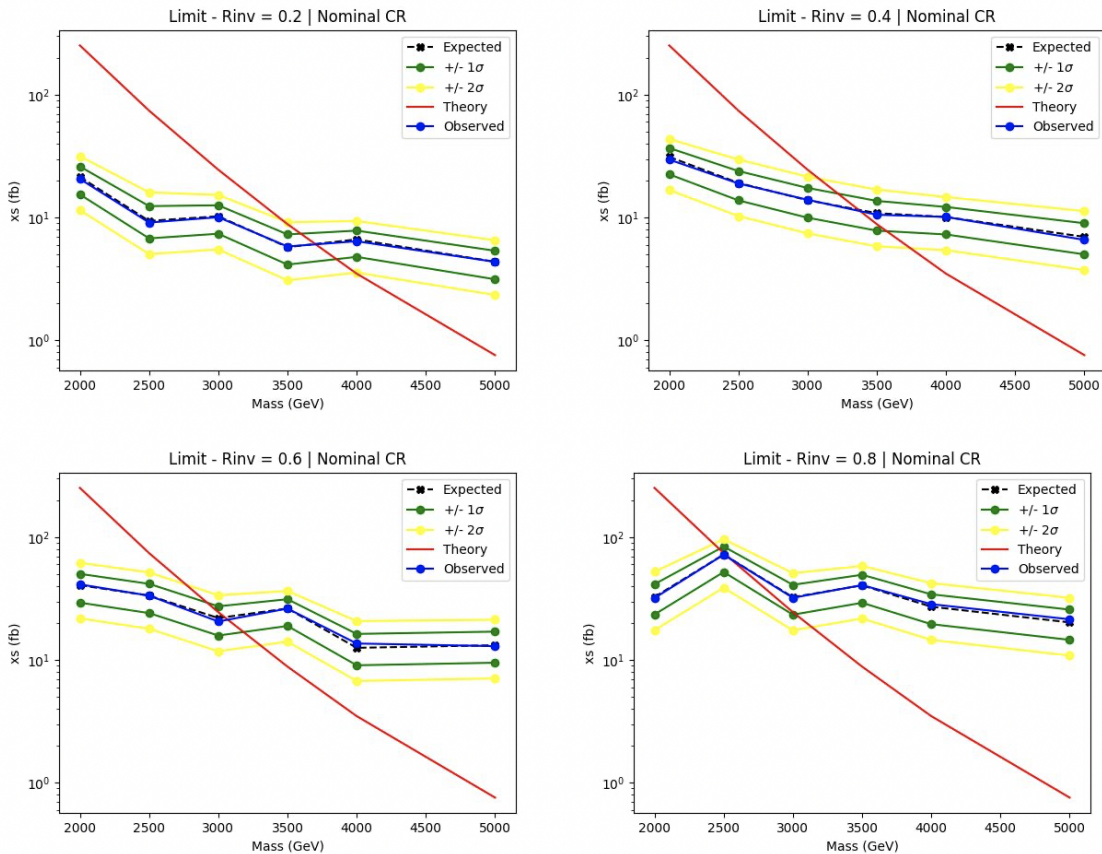


Figure 8.16: 95% C.L. upper limits for signal models across  $Z'$  mass, for four different  $R_{inv}$  fractions, from the CR region (without systematics). TODO - ATLAS style

1921 The ability of the fit to identify a significant excess is tested by calculating the limits on  
 1922 signal injected toys.  $2\sigma$  and  $5\sigma$  of signal is injected for each signal point into 50 Asimov data

1923 toys. Figure 8.17 demonstrates the impact of this signal injection on the limit for  $R_{inv} = 0.2$ .  
 1924 The observed limit rises as more signal is injected, indicating the ability of the fit to identify a  
 1925 significant signal excess.

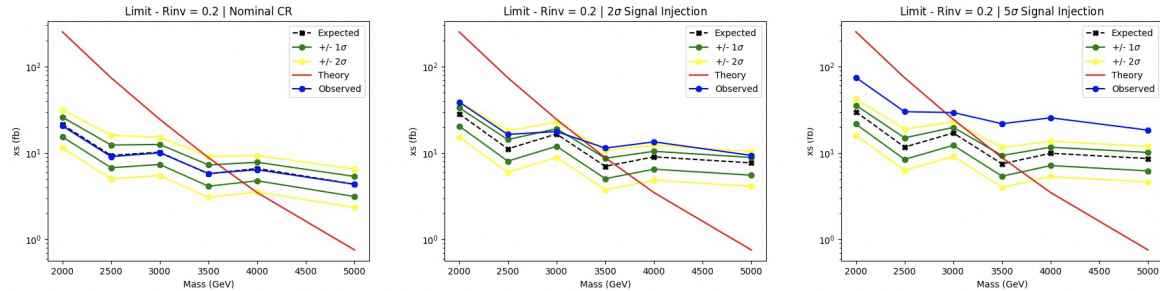


Figure 8.17: 95% C.L. upper limits and observed limit for signal models across  $Z'$  mass, with varying amounts of signal injected. TODO - ATLAS style

### 1926 8.5.2 Discovery Strategy

1927 Model-independent fits for the discovery region are performed using PYBUMPHUNTER [86].  
 1928 The strategy consists of comparing the data in a given  $m_T$  spectrum of interest to a background  
 1929 estimation derived by performing the polynomial fit and sampling from the post-fit function into a  
 1930 histogram.

1931 The polynomial fit is done to an  $m_T$  distribution with 180 bins (25 GeV wide), half the width  
 1932 of the fits in the SVJ Fit region (50 GeV wide). The narrower bins allow for rebinning based on  
 1933 the *signal mass resolution* of the SVJ signals. The binning strategy is outlined in Appendix D.1.

1934 Figure 8.18 shows the fit and residuals with of the polynomial with the narrower binning in the  
 1935 CR and the Discovery VR data. Table 8.3 shows the post-fit values of the fit parameters and their  
 1936 uncertainties for the CR and VR. These results indicate good ability of the 5-parameter polynomial  
 1937 to model the ANTELOPE selected data.

1938 The studies shown in Section 8.5.1 validate the robustness of the background polynomial fit.  
 1939 The narrower bins are the only difference for polynomial fitting between the SVJ Fit and Discovery  
 1940 Fit strategies, and they are not observed to reduce the quality or consistency of the fit.

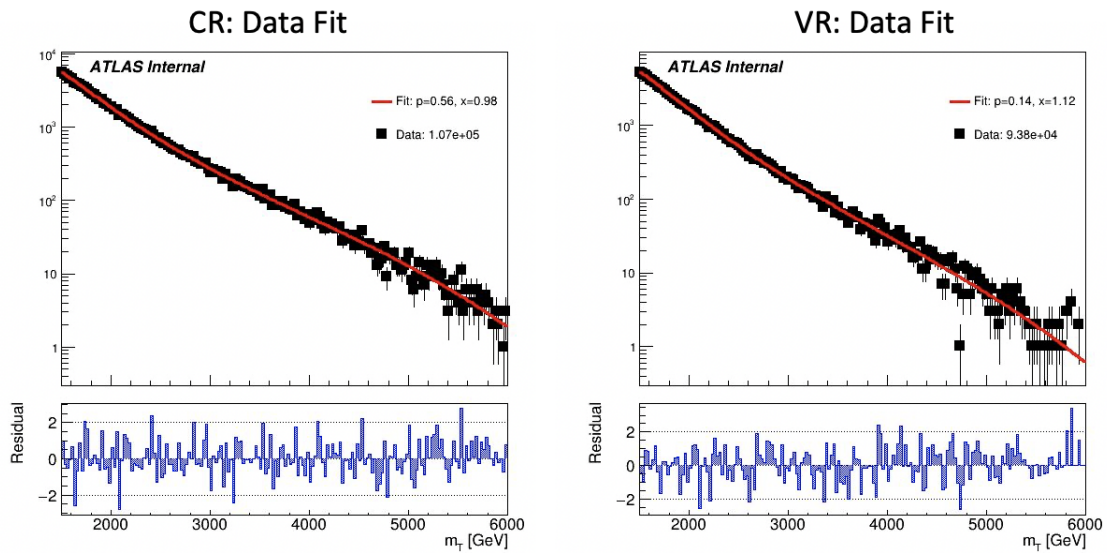


Figure 8.18: Post-fit function and residuals for the ANTELOPE CR and VR.

Parameter	CR		VR	
	Value	Error	Value	Error
p1	1.0709e+05	4.65e+02	9.3776e+04	4.34e+02
p2	4.5945e+01	3.03e+00	4.5787e+01	3.78e+00
p3	5.8566e+01	3.88e+00	5.6014e+01	4.58e+00
p4	2.5593e+01	1.50e+00	2.4914e+01	1.73e+00
p5	3.9196e+00	2.22e-01	3.8809e+00	2.53e-01

Table 8.3: Post-fit parameters for the ANTELOPE CR and VR.

1941 **BumpHunter Fits**

1942 The signal mass resolution binning strategy described in Appendix D.1 creates a monotonically  
 1943 increasing set of bins. While the SVJ signals help inform the binning, the binning is still broadly  
 1944 applicable to a variety of potential signal models. The mass resolution of any resonant signal  
 1945 generally widens as the mass of the mediator particle increases. A similar strategy and binning  
 1946 was used in the generic heavy resonance search presented in Ref. [84]. The resulting set of 15 bins  
 1947 to be used in the BumpHunter fits varies in width from 100 GeV at the  $m_T$  core to 925 GV in the  
 1948  $m_T$  tail.

1949 Figure 8.19 shows the result of running BumpHunter over the rebinned CR and VR  $m_T$  spectra.  
 1950 The background estimation is given by polynomial fit function. The high p-values ( $>0.01$ ) indicate  
 good agreement with the background estimation.

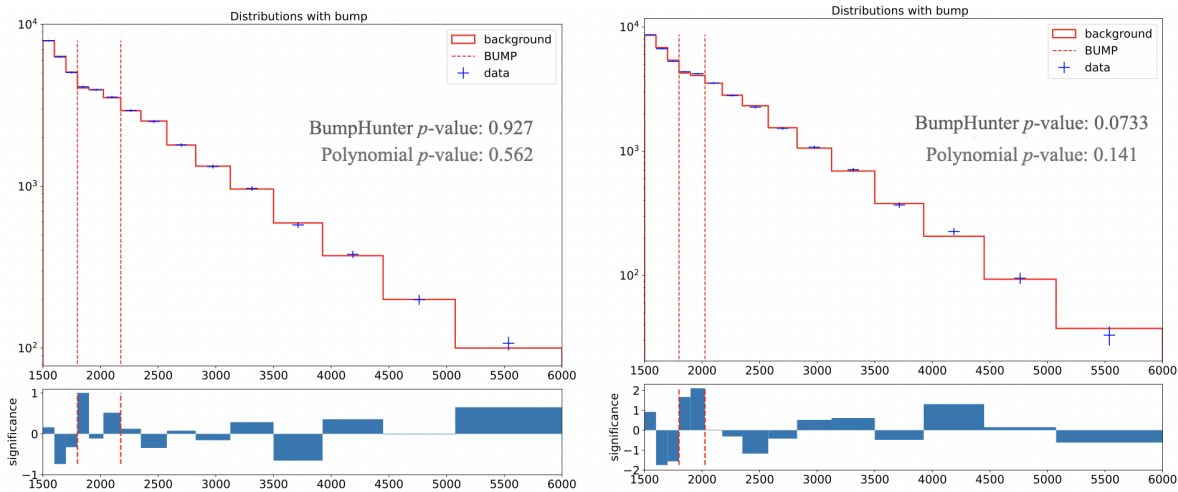


Figure 8.19: BumpHunter fits on the ANTELOPE  $m_T$  spectra for both the CR (left) and VR (right). In a signal-depleted region, good agreement with the background estimation is observed.

1951  
 1952 Figure 8.20 shows BumpHunter p-values over 100 Asimov trials, where each toy is scaled to  
 1953 the statistics of the SR. The agreement is generally very good, as the p-values trend towards higher  
 1954 values. No fits with a *spurious signal* are found. A spurious signal would be indicated by a fit with  
 1955 a p-value  $< 0.01$ , indicating a bump of at least  $2\sigma$  significance.

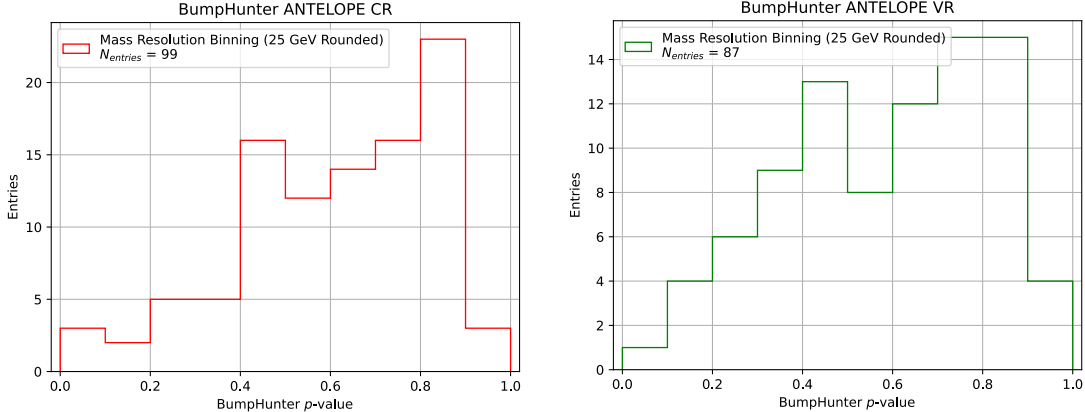


Figure 8.20: BumpHunter p-values extracted for 100 Asimov toys for both the ANTELOPE CR (left) and VR (right).

### 1956    BumpHunter Signal Injection

1957    To explore a model independent signal hypothesis, signal injection tests in the ANTELOPE re-  
 1958    gion are done with generic Gaussian shapes. Two Gaussian models are built with a mean ranging  
 1959    from 2000 GeV to 5000 GeV and a standard deviation equal to 10 or 20% the mean value. Fig-  
 1960    ure 8.21 illustrates an injected Gaussian and its effect on the  $m_T$  distribution. The 20% gaussian  
 1961    represents the widest possible signals we might be sensitive to with a BH strategy, while the 10%  
 1962    injection represents a narrower signal peak.

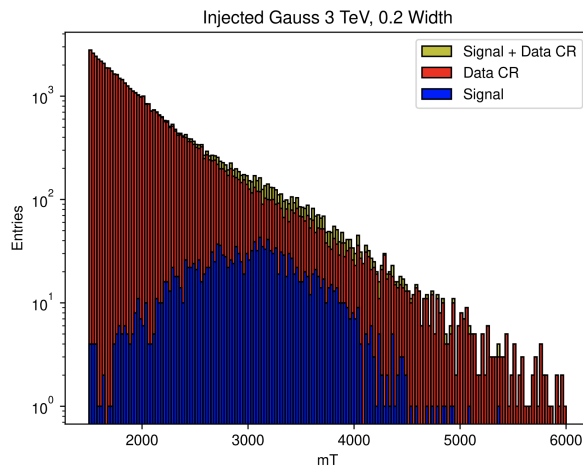


Figure 8.21: Example injected gaussian signal.

1963    An estimated  $5\sigma$  of signal is injected for these tests. The estimate is derived from the polyno-

1964 mial fitting framework, and is therefore an underestimate, as the flexibility of the polynomial fit  
1965 absorbs some of the signal. Therefore we do not expect to measure  $5\sigma$  significance with the BH  
1966 approach, but rather hope to see that some level of signal (at least  $\geq 2\sigma$  significance) is observed  
1967 by the BumpHunter framework.

1968 Results are obtained by averaging over 100 toys for each injection. Figure 8.22 shows the  
1969 resulting max local significance (in an  $m_T$  bin) and the location of the determined bump, indicating  
1970 a good response of the BumpHunter framework for detecting generic  $m_T$  resonances at the right  
1971 location. Only the 5000 GeV 20% width point is not properly identified by the framework. While  
1972 some sensitivity is lost due to the flexible nature of the fitting framework, the ability to identify a  
1973 bump with substantial local significance in the correct location is observed. Figure 8.23 shows an  
1974 example of the identified bump.

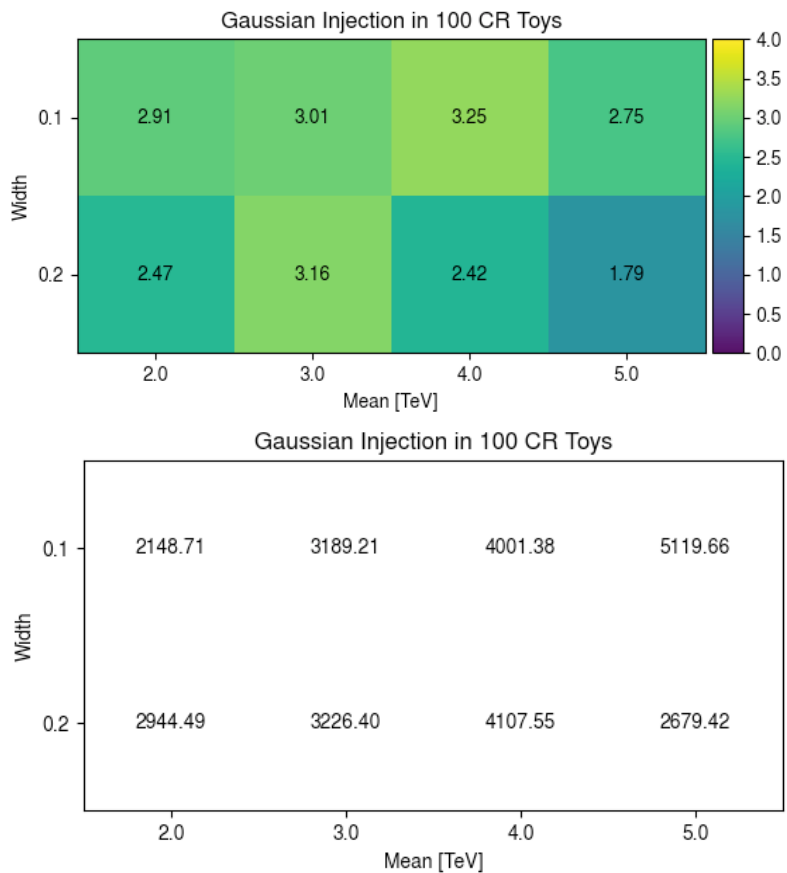


Figure 8.22: Response of the BumpHunter framework to signal injection of  $5\sigma$  significance to the model-dependent polynomial fit framework. The local significance (top) and bump location (bottom) are shown.

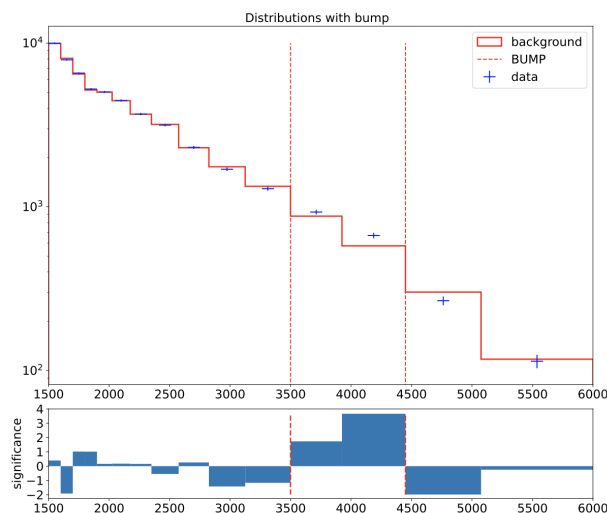


Figure 8.23: Example BH response to gaussian signal injection at 4000 GeV with width of 10%.

1975

1976

## Chapter 9: Results

1977 The final results of this analysis are the polynomial fit to the  $m_T$  distribution in the SVJ Fit  
1978 SR, and the BumpHunter evaluation of the  $m_T$  distribution in the Discovery SR. In the SVJ Fit  
1979 region, systematic uncertainties are evaluated on the signal model, and *limits*<sup>1</sup> on the observed  $Z'$   
1980 production cross-section are set.

### 1981 9.1 SVJ Fit Result

1982 Figure 9.1 shows the unblinded  $m_T$  spectrum in the SVJ Fit SR with a background-only fit. The  
1983 fit is successful and has a p-value of 0.265, indicating the data is compatible with the background  
1984 hypothesis. Table 9.1 gives the values and uncertainties for the five parameters of the polynomial  
fit.

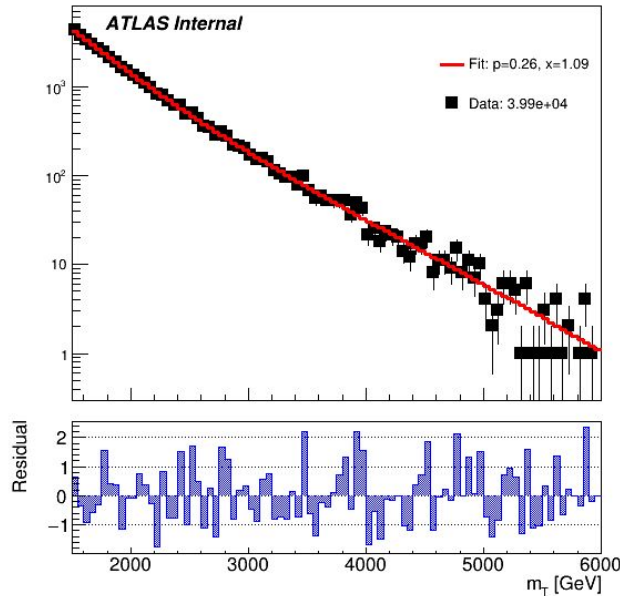


Figure 9.1:  $m_T$  in the unblinded SVJ Fit SR with a background-only fit (p-value = 0.265).

1985

---

<sup>1</sup>A limit is an upper bound of the branching ratio of a signal process

Parameter	SR	
	Value	Error
p1	3.9952e+04	2.83e+02
p2	1.8517e+01	9.08e-01
p3	1.4883e+01	4.43e-01
p4	8.0513e+00	1.21e-01
p5	1.3469e+00	3.62e-02

Table 9.1: Post-fit parameters for the PFN SR.  $p1$  can also be considered  $N_{bkg}$  or the normalization factor.

### 1986 9.1.1 Systematics

1987 As is typically done in dijet resonance searches using a polynomial fit [92], the systematic un-  
 1988 certainties in this analysis are applied only to the signal and not to the background. This is because  
 1989 the background expectation is determined entirely from the data in the SR via the polynomial fit.  
 1990 Therefore the only uncertainty on the background is the statistical uncertainty, which is reflected  
 1991 in the uncertainty associated to each of the five freely floating parameters determined in the fit.

1992 A variety of systematics on the signal shape and yield are considered. The most significant of  
 1993 these is the *spurious signal* systematic, which quantifies the level of signal observed in the absence  
 1994 of signal injection. Experimental uncertainties on the luminosity and jet reconstruction are studied.  
 1995 Finally, uncertainties on the MC simulation of the SVJ theory model are also considered.

### 1996 Spurious Signal

1997 The spurious signal uncertainty is assessed following the prescription in Ref.[89]. In this pro-  
 1998 cedure, the spurious signal is defined using pseudo-data experiments, which are drawn from a  
 1999 smoothed template as described in Section 8.5.1. A spurious signal uncertainty is included in the  
 2000 fit as a *yield* uncertainty on each signal point.

2001 The spurious signal  $\mu_{\text{spur}}$  is quantified for each signal as the mean number of signal events fitted  
 2002 across 100 signal-free pseudo-data experiments. To determine if the amount of spurious signal is

tolerable, the threshold  $\mu_{\text{spur}}/\sigma_{\text{spur}} < 0.5$  is used [89].  $\sigma_{\text{spur}}$  for each signal point is the standard deviation on the number of fitted signal events across the 100 pseudo-data experiments. Figure 9.2 gives examples of these pseudo-data experiments, revealing Gaussian distributions from which the mean and standard deviation used for this measurement are taken.

Figure 9.3 shows the  $\mu_{\text{spur}}/\sigma_{\text{spur}}$  metric. The requirement for  $\mu_{\text{spur}}/\sigma_{\text{spur}} < 0.5$  is easily satisfied across the signal grid.

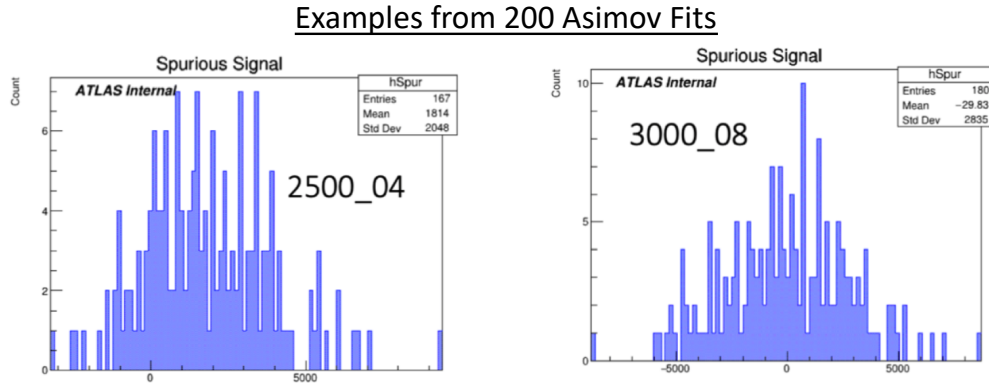


Figure 9.2: Example spurious signal fits, indicating a Gaussian distribution around the mean of spurious signal events.

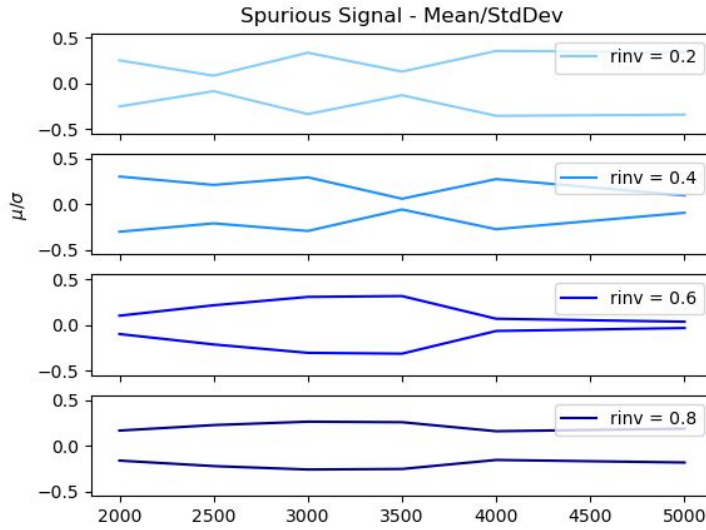


Figure 9.3: Spurious signal as a function of resonance mass. The requirement  $\mu/\sigma < 0.5$  is satisfied for all signal points, where  $\mu$  is the mean number of spurious signal events and  $\sigma$  is the standard deviation of the number of spurious signal events from 100 pseudo-data experiments.

Uncertainty	Effect on Yield [%]
Luminosity	0.83
JES	0.04 - 1.39
JER	0.01 - 0.64

Table 9.2: Summary of Experimental Uncertainties and their impact on the yield of MC signal events.

## 2009    **Experimental Uncertainties**

2010       The main experimental uncertainties are on the recorded luminosity, *jet energy scale*, and *jet*  
 2011      *energy resolution*. The jet energy scale (JES) corrects for the non-compensating calorimeter re-  
 2012      sponse and jet energy losses in passive detector material [93]. The jet energy resolution (JER)  
 2013      applies a correction based on the ratio between a jet’s true energy and its reconstructed energy,  
 2014      as determined in simulation. Systematics uncertainties on the JES and JER processes must be  
 2015      considered for any analysis using reconstructed jets.

2016       A flat yield uncertainty of 0.83% is applied for all signals, corresponding to the uncertainty  
 2017      reported on the luminosity measurement by the LUCID detector [94].

2018       The JES and JER uncertainties are evaluated on each signal point for their impact on both the  
 2019      yield and shape of the  $m_T$  distribution. Table 9.2 summarizes the range impact on the yield for  
 2020      each uncertainty. The impact of these uncertainties on the signal yield is generally negligible in  
 2021      comparison to the spurious signal systematic, which ranges from 4.2% in the case of the lowest  
 2022       $Z'$  mass points to >100% in the case of the highest  $Z'$  mass points. In the 2000 GeV  $Z'$  mass  
 2023      case (which has the lowest relative spurious signal uncertainty), the maximum yield difference due  
 2024      to experimental uncertainty is 0.53%, or almost an order of magnitude reduced compared to the  
 2025      spurious signal uncertainty.

2026       The impact of the JES and JER uncertainties on the shape of the  $m_T$  distribution is also consid-  
 2027      ered. An example individual JES variation is shown in Figure 9.4, illustrating the minimal impact  
 2028      of this uncertainty on the shape of  $m_T$ .

2029       To make a conservative estimate of their impact on the shape, all shape uncertainty sources  
 2030      are summed in quadrature, bin-by-bin. This results in a maximum “up” variation and a maximum

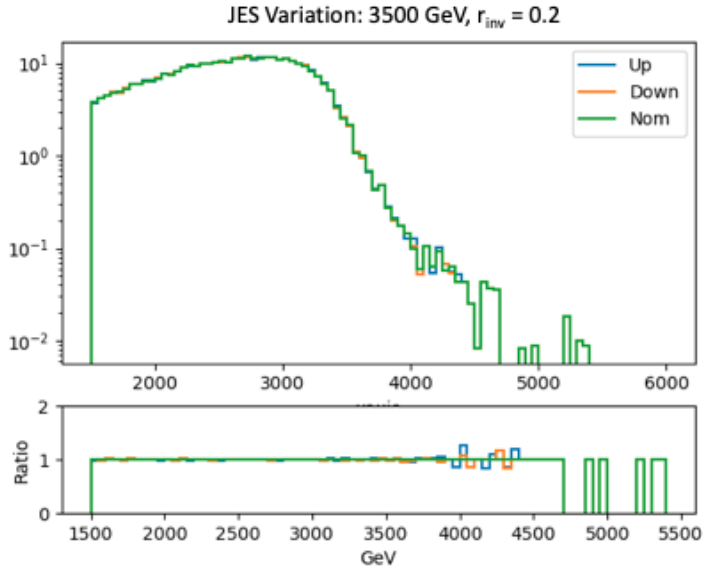


Figure 9.4:  $m_T$  of the 3500 GeV  $Z'$ ,  $R_{inv} = 0.2$  signal point, shown with an example JES variation. The nominal shape (“Nom”),  $1\sigma$  up (“Up”), and  $1\sigma$  down (“down”) variations are shown. The variation is seen to have a negligible impact on the signal shape.

2031 “down” variation. The the impact of these maximal shape variations on the  $Z'$  production cross-  
 2032 section limit is evaluated, and uncertainty on this limit is propagated to the final limit bands. The  
 2033 impact is generally seen to be quite small, changing the limit variation by 0.2 fb at most. An  
 2034 example of the variations summed in quadrature is shown in Figure 9.5.

### 2035 Theory Uncertainty

2036 Uncertainty on the parameters of the signal model are also considered. The primary theory  
 2037 uncertainty source is the tuning of the parton shower in PYTHIA8 [95]. Jet structure and extra  
 2038 jet production within the event depend on the modeling of initial state radiation (ISR), final state  
 2039 radiation (FSR) and behavior of multiple parton interactions (MPI) within an event. A variety of  
 2040 MC generation tuning parameters govern the behavior of ISR, FSR and MPI in the signal genera-  
 2041 tion. Ref [96] describes how these parameters are condensed into 10 variations which capture the  
 2042 maximal range of impact for these tuning parameters.

2043 The 10 variations (representing 5 up/down variation pairs) are evaluated for the SVJ signal  
 2044 shapes. Figure 9.6 provides a look at the effect of these variations on the SVJ  $m_T$  signal shape.

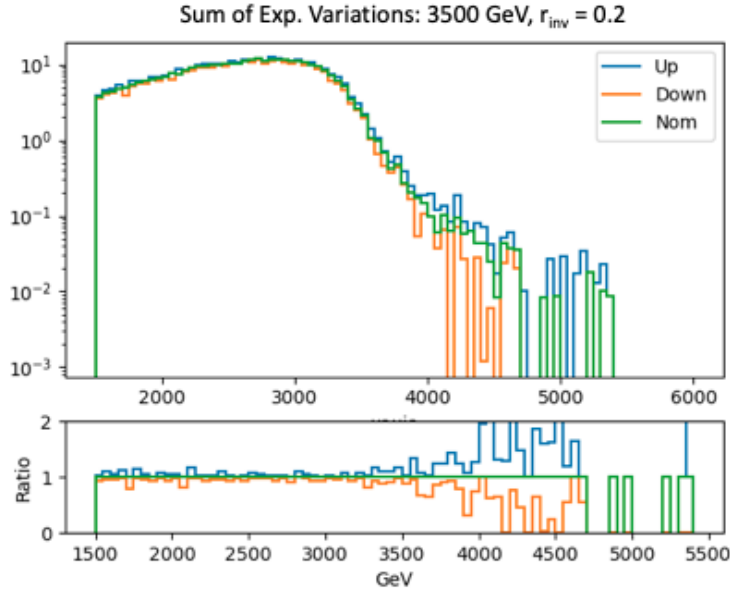


Figure 9.5:  $m_T$  of the 3500 GeV  $Z'$ ,  $R_{inv} = 0.2$  signal point, shown with the sum in quadrature of all JES and JER variations. The nominal shape (“Nom”),  $1\sigma$  up (“Up”), and  $1\sigma$  down (“down”) variations are shown.

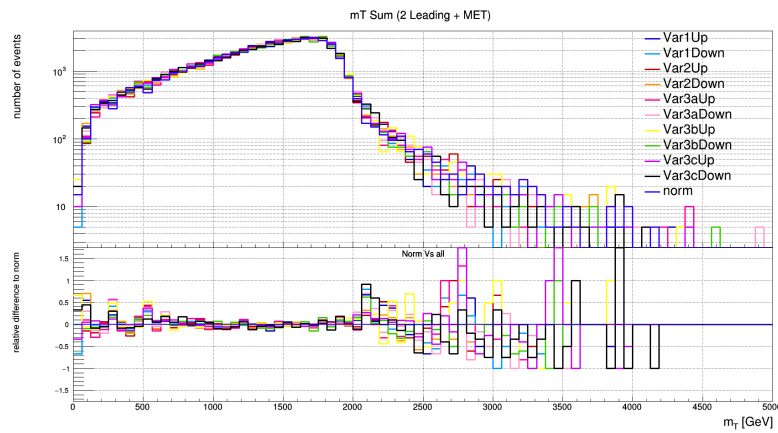


Figure 9.6: Signal distribution of  $m_T$ , varying the ISR, FSR and MPI configuration.

2045 All 10 variations are determined to be flat within uncertainty, and thus the systematic is con-  
2046 sidered for its impact on the signal yield. The variation in the signal yield is at most 5% (TODO  
2047 - determine exactly), which is incorporated into the fitted systematics. The spurious signal uncer-  
2048 tainty is dominant for all but the lowest mass signal points.

2049 **9.1.2 Interpretation**

2050 Using a modified frequentist approach [97], *exclusion limits* at the 95% confident level (CL)  
2051 are derived. Exclusion limits refer to determining the maximum (or *limiting*) signal cross-section  
2052 compatible with the observed data spectrum, such that any theory resulting in a signal cross-section  
2053 above the limit is excluded with 95% confidence. The limit is determined from a maximum like-  
2054 lihood test statistic [98], which determines the likelihood of observing the given data spectrum  
2055 using the background hypothesis, signal hypothesis, and uncertainty parameters. Compatibility  
2056 of the signal model with the observed distribution is tested by generating pseudo-data based on  
2057 the background estimation and including varying amounts of signal. Through analysis of these  
2058 pseudo-data experiments, the maximum number of signals events that is compatible with the ob-  
2059 served data distribution can be determined. The 95% confidence level is enforced by dictating that  
2060 the number of signal events must be compatible with the observed data within  $2\sigma$  of uncertainty.

2061 The final limits on the  $Z'$  cross section after the implementation of the systematic uncertainties  
2062 are shown in Figure 9.7. Exclusion of the theoretical model is observed for the 2000 GeV  $Z'$   
2063 mass point for all  $R_{inv}$  values. We are unable to exclude the highest mass points due to their low  
2064 theoretical cross section, and relatively high spurious signal uncertainty. The most mass points are  
2065 excluded for  $R_{inv} = 0.2$ , which excludes  $Z'$  masses up to 3500 GeV.

2066 **9.2 Discovery Result**

2067 Figure 9.8 shows the unblinded  $m_T$  spectrum in the Discovery SR with a background-only fit,  
2068 and the resulting BumpHunter test. The polynomial fit is successful and has a B-only p-value  
2069 of 0.74, indicating the data is compatible with the background hypothesis. The BumpHunter test

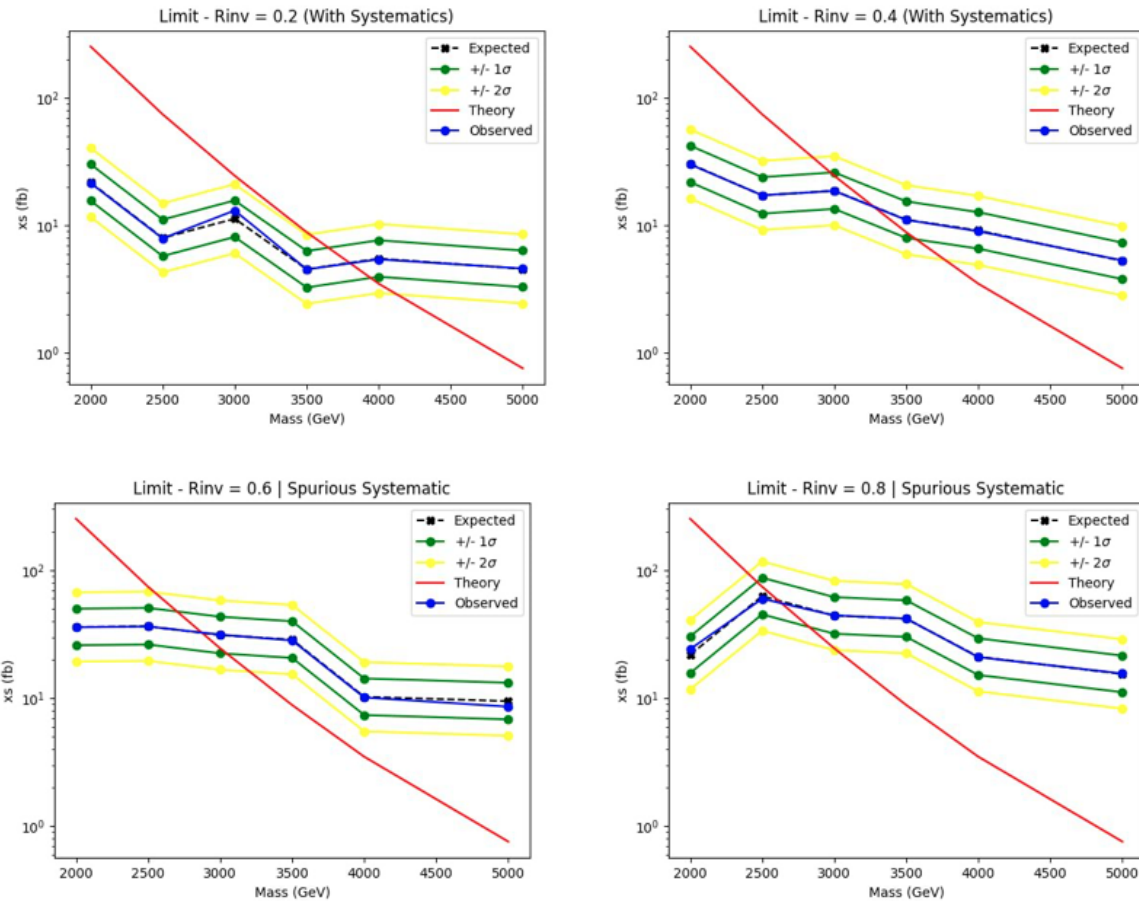


Figure 9.7: Expected and observed 95% CL limits in the unblinded SR, as a function of  $Z'$  masses for  $R_{inv}=0.2$  (top left), 0.4 (top right), 0.6 (bottom left), 0.8 (bottom right); no systematics.

2070 gives a p-value of 0.8098, indicating no significant excess. The maximum local significance is  
 $0.877\sigma$ .

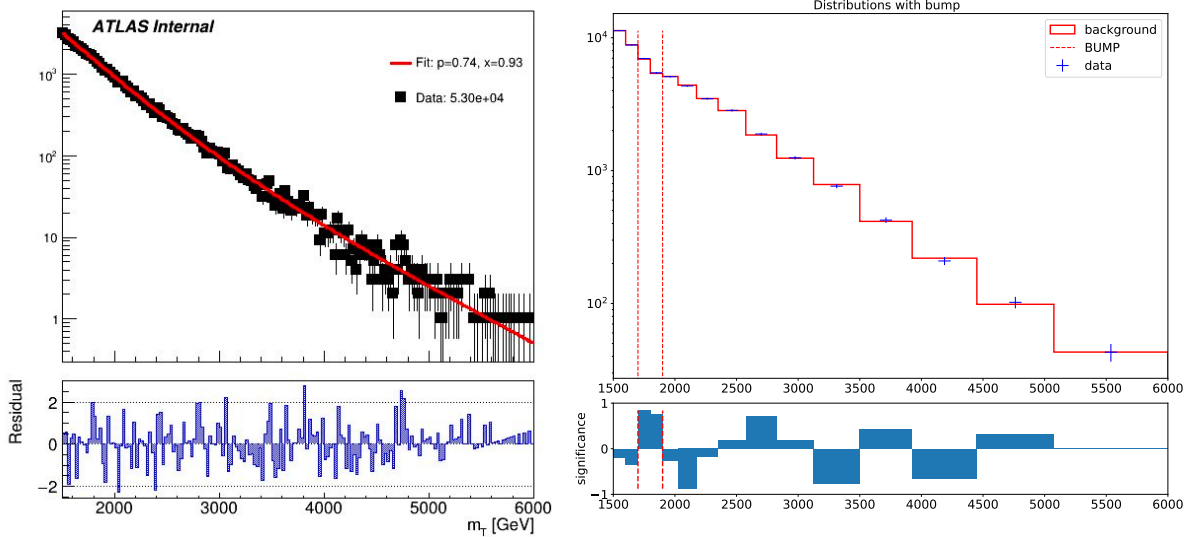


Figure 9.8:  $m_T$  in the unblinded ANTELOPE SR with a background-only fit (p-value = 0.74), left. BumpHunter test selecting the most significant data excess with a p-value of 0.8098, right.

2071  
2072 Because there is no specific signal interpretation for the Discovery region and both the poly-  
2073 nomial fit and BH analysis are entirely data driven, there are no systematics to consider in the  
2074 interpretation of the BH result.

2075

## Conclusion or Epilogue

2076        Use this page for your epilogue or conclusion if applicable; please use only one of the titles  
2077      for this page. Otherwise, you may delete it. Use this page for your epilogue or conclusion if  
2078      applicable; please use only one of the titles for this page. Otherwise, you may delete it. Use this  
2079      page for your epilogue or conclusion if applicable; please use only one of the titles for this page.  
2080      Otherwise, you may delete it. Use this page for your epilogue or conclusion if applicable; please  
2081      use only one of the titles for this page. Otherwise, you may delete it. Use this page for your  
2082      epilogue or conclusion if applicable; please use only one of the titles for this page. Otherwise,  
2083      you may delete it. Use this page for your epilogue or conclusion if applicable; please use only one  
2084      of the titles for this page. Otherwise, you may delete it. Use this page for your epilogue or  
2085      conclusion if applicable; please use only one of the titles for this page. Otherwise, you may delete  
2086      it. Use this page for your epilogue or conclusion if applicable; please use only one of the titles for  
2087      this page. Otherwise, you may delete it. Use this page for your epilogue or conclusion if  
2088      applicable; please use only one of the titles for this page. Otherwise, you may delete it. Use this  
2089      page for your epilogue or conclusion if applicable; please use only one of the titles for this page.  
2090      Otherwise, you may delete it. Use this page for your epilogue or conclusion if applicable; please  
2091      use only one of the titles for this page. Otherwise, you may delete it. Use this page for your  
2092      epilogue or conclusion if applicable; please use only one of the titles for this page. Otherwise,  
2093      you may delete it. Use this page for your epilogue or conclusion if applicable; please use only one  
2094      of the titles for this page. Otherwise, you may delete it. Use this page for your epilogue or  
2095      conclusion if applicable; please use only one of the titles for this page. Otherwise, you may delete

2096 it. Use this page for your epilogue or conclusion if applicable; please use only one of the titles for  
2097 this page. Otherwise, you may delete it. Use this page for your epilogue or conclusion if  
2098 applicable; please use only one of the titles for this page. Otherwise, you may delete it. Use this  
2099 page for your epilogue or conclusion if applicable; please use only one of the titles for this page.  
2100 Otherwise, you may delete it. Use this page for your epilogue or conclusion if applicable; please  
2101 use only one of the titles for this page. Otherwise, you may delete it. Use this page for your  
2102 epilogue or conclusion if applicable; please use only one of the titles for this page. Otherwise,  
2103 you may delete it. Use this page for your epilogue or conclusion if applicable; please use only one  
2104 of the titles for this page. Otherwise, you may delete it. Use this page for your epilogue or  
2105 conclusion if applicable; please use only one of the titles for this page. Otherwise, you may delete  
2106 it. Use this page for your epilogue or conclusion if applicable; please use only one of the titles for  
2107 this page. Otherwise, you may delete it. Use this page for your epilogue or conclusion if  
2108 applicable; please use only one of the titles for this page. Otherwise, you may delete it. Use this  
2109 page for your epilogue or conclusion if applicable; please use only one of the titles for this page.  
2110 Otherwise, you may delete it. Use this page for your epilogue or conclusion if applicable; please  
2111 use only one of the titles for this page. Otherwise, you may delete it. Use this page for your  
2112 epilogue or conclusion if applicable; please use only one of the titles for this page. Otherwise,  
2113 you may delete it. Use this page for your epilogue or conclusion if applicable; please use only one  
2114 of the titles for this page. Otherwise, you may delete it. Use this page for your epilogue or  
2115 conclusion if applicable; please use only one of the titles for this page. Otherwise, you may delete  
2116 it. Use this page for your epilogue or conclusion if applicable; please use only one of the titles for  
2117 this page. Otherwise, you may delete it. Use this page for your epilogue or conclusion if  
2118 applicable; please use only one of the titles for this page. Otherwise, you may delete it. Use this  
2119 page for your epilogue or conclusion if applicable; please use only one of the titles for this page.  
2120 Otherwise, you may delete it. Use this page for your epilogue or conclusion if applicable; please  
2121 use only one of the titles for this page. Otherwise, you may delete it. Use this page for your  
2122 epilogue or conclusion if applicable; please use only one of the titles for this page. Otherwise,

2123 you may delete it. Use this page for your epilogue or conclusion if applicable; please use only one  
2124 of the titles for this page. Otherwise, you may delete it. Use this page for your epilogue or  
2125 conclusion if applicable; please use only one of the titles for this page. Otherwise, you may delete  
2126 it. Use this page for your epilogue or conclusion if applicable; please use only one of the titles for  
2127 this page. Otherwise, you may delete it. Use this page for your epilogue or conclusion if  
2128 applicable; please use only one of the titles for this page. Otherwise, you may delete it. Use this  
2129 page for your epilogue or conclusion if applicable; please use only one of the titles for this page.  
2130 Otherwise, you may delete it. Use this page for your epilogue or conclusion if applicable; please  
2131 use only one of the titles for this page. Otherwise, you may delete it. Use this page for your  
2132 epilogue or conclusion if applicable; please use only one of the titles for this page. Otherwise,  
2133 you may delete it. Use this page for your epilogue or conclusion if applicable; please use only one  
2134 of the titles for this page. Otherwise, you may delete it. Use this page for your epilogue or  
2135 conclusion if applicable; please use only one of the titles for this page. Otherwise, you may delete  
2136 it. Use this page for your epilogue or conclusion if applicable; please use only one of the titles for  
2137 this page. Otherwise, you may delete it. Use this page for your epilogue or conclusion if  
2138 applicable; please use only one of the titles for this page. Otherwise, you may delete it. Use this  
2139 page for your epilogue or conclusion if applicable; please use only one of the titles for this page.  
2140 Otherwise, you may delete it. Use this page for your epilogue or conclusion if applicable; please  
2141 use only one of the titles for this page. Otherwise, you may delete it. Use this page for your  
2142 epilogue or conclusion if applicable; please use only one of the titles for this page. Otherwise,  
2143 you may delete it. Use this page for your epilogue or conclusion if applicable; please use only one  
2144 of the titles for this page. Otherwise, you may delete it. Use this page for your epilogue or  
2145 conclusion if applicable; please use only one of the titles for this page. Otherwise, you may delete  
2146 it. Use this page for your epilogue or conclusion if applicable; please use only one of the titles for  
2147 this page. Otherwise, you may delete it. Use this page for your epilogue or conclusion if  
2148 applicable; please use only one of the titles for this page. Otherwise, you may delete it. Use this  
2149 page for your epilogue or conclusion if applicable; please use only one of the titles for this page.

2150 Otherwise, you may delete it. Use this page for your epilogue or conclusion if applicable; please  
2151 use only one of the titles for this page. Otherwise, you may delete it. Use this page for your  
2152 epilogue or conclusion if applicable; please use only one of the titles for this page. Otherwise,  
2153 you may delete it. Use this page for your epilogue or conclusion if applicable; please use only one  
2154 of the titles for this page. Otherwise, you may delete it. Use this page for your epilogue or  
2155 conclusion if applicable; please use only one of the titles for this page. Otherwise, you may delete  
2156 it. Use this page for your epilogue or conclusion if applicable; please use only one of the titles for  
2157 this page. Otherwise, you may delete it. Use this page for your epilogue or conclusion if  
2158 applicable; please use only one of the titles for this page. Otherwise, you may delete it. Use this  
2159 page for your epilogue or conclusion if applicable; please use only one of the titles for this page.  
2160 Otherwise, you may delete it. Use this page for your epilogue or conclusion if applicable; please  
2161 use only one of the titles for this page. Otherwise, you may delete it. Use this page for your  
2162 epilogue or conclusion if applicable; please use only one of the titles for this page. Otherwise,  
2163 you may delete it. Use this page for your epilogue or conclusion if applicable; please use only one  
2164 of the titles for this page. Otherwise, you may delete it. Use this page for your epilogue or  
2165 conclusion if applicable; please use only one of the titles for this page. Otherwise, you may delete  
2166 it. Use this page for your epilogue or conclusion if applicable; please use only one of the titles for  
2167 this page. Otherwise, you may delete it. Use this page for your epilogue or conclusion if  
2168 applicable; please use only one of the titles for this page. Otherwise, you may delete it. Use this  
2169 page for your epilogue or conclusion if applicable; please use only one of the titles for this page.  
2170 Otherwise, you may delete it. Use this page for your epilogue or conclusion if applicable; please  
2171 use only one of the titles for this page. Otherwise, you may delete it. Use this page for your  
2172 epilogue or conclusion if applicable; please use only one of the titles for this page. Otherwise,  
2173 you may delete it. Use this page for your epilogue or conclusion if applicable; please use only one  
2174 of the titles for this page. Otherwise, you may delete it. Use this page for your epilogue or  
2175 conclusion if applicable; please use only one of the titles for this page. Otherwise, you may delete  
2176 it.

## References

- 2178 [1] Jens Erler and Paul Langacker. “Electroweak model and constraints on new physics”. In:  
2179 (July 2004). arXiv: hep-ph/0407097.
- 2180 [2] David J Griffiths. *Introduction to elementary particles; 2nd rev. version*. Physics textbook.  
2181 New York, NY: Wiley, 2008.
- 2182 [3] M. Tanabashi et al. “Review of Particle Physics”. In: *Phys. Rev. D* 98 (3 2018), pp. 847–851.
- 2183 [4] E. Noether. “Invariante Variationsprobleme”. In: *Nachr. d. König. Gesellsch. d. Wiss. zu  
2184 Göttingen, Math-phys. Klasse, Seite 235-157* (1918). eprint: www.physics.ucla.edu/  
2185 \~\cwp/articles/noether.trans/german/emmy235.html.
- 2186 [5] J. H. Christenson et al. “Evidence for the  $2\pi$  Decay of the  $K_2^0$  Meson”. In: *Phys. Rev. Lett.*  
2187 13 (1964), pp. 138–140.
- 2188 [6] Michael Gronau. “CP Violation in B Meson Decays”. In: *Nuclear Physics B - Proceedings  
2189 Supplements* 142 (May 2005), 263–270.
- 2190 [7] J. E. Augustin et al. “Discovery of a Narrow Resonance in  $e^+e^-$  Annihilation”. In: *Phys.  
2191 Rev. Lett.* 33 (1974), pp. 1406–1408.
- 2192 [8] J. J. Aubert et al. “Experimental Observation of a Heavy Particle  $J$ ”. In: *Phys. Rev. Lett.* 33  
2193 (1974), pp. 1404–1406.
- 2194 [9] Martin L. Perl et al. “Evidence for Anomalous Lepton Production in e+ - e- Annihilation”.  
2195 In: *Phys. Rev. Lett.* 35 (1975), pp. 1489–1492.
- 2196 [10] S. W. Herb et al. “Observation of a Dimuon Resonance at 9.5-GeV in 400-GeV Proton-  
2197 Nucleus Collisions”. In: *Phys. Rev. Lett.* 39 (1977), pp. 252–255.
- 2198 [11] F. Abe et al. “Observation of top quark production in  $\bar{p}p$  collisions”. In: *Phys. Rev. Lett.* 74  
2199 (1995), pp. 2626–2631. arXiv: hep-ex/9503002.
- 2200 [12] S. Abachi et al. “Observation of the top quark”. In: *Phys. Rev. Lett.* 74 (1995), pp. 2632–  
2201 2637. arXiv: hep-ex/9503003.
- 2202 [13] K. Kodama et al. “Observation of tau neutrino interactions”. In: *Phys. Lett. B* 504 (2001),  
2203 pp. 218–224. arXiv: hep-ex/0012035.

- 2204 [14] G. Arnison et al. “Experimental Observation of Lepton Pairs of Invariant Mass Around 95-  
 2205 GeV/c\*\*2 at the CERN SPS Collider”. In: *Phys. Lett. B* 126 (1983), pp. 398–410.
- 2206 [15] P. Bagnaia et al. “Evidence for  $Z^0 \rightarrow e^+e^-$  at the CERN  $\bar{p}p$  Collider”. In: *Phys. Lett. B* 129  
 2207 (1983), pp. 130–140.
- 2208 [16] Serguei Chatrchyan et al. “Observation of a New Boson at a Mass of 125 GeV with the  
 2209 CMS Experiment at the LHC”. In: *Phys. Lett. B* 716 (2012), pp. 30–61. arXiv: 1207.7235  
 2210 [hep-ex].
- 2211 [17] Georges Aad et al. “Observation of a new particle in the search for the Standard Model  
 2212 Higgs boson with the ATLAS detector at the LHC”. In: *Phys. Lett. B* 716 (2012), pp. 1–29.  
 2213 arXiv: 1207.7214 [hep-ex].
- 2214 [18] K. G. Begeman, A. H. Broeils, and R. H. Sanders. “Extended rotation curves of spiral galaxies:  
 2215 Dark haloes and modified dynamics”. In: *Mon. Not. Roy. Astron. Soc.* 249 (1991), p. 523.
- 2216 [19] Y. Ashie et al. “Evidence for an oscillatory signature in atmospheric neutrino oscillation”.  
 2217 In: *Phys. Rev. Lett.* 93 (2004), p. 101801. arXiv: hep-ex/0404034.
- 2218 [20] C. Abel et al. “Measurement of the Permanent Electric Dipole Moment of the Neutron”. In:  
 2219 *Phys. Rev. Lett.* 124.8 (2020), p. 081803. arXiv: 2001.11966 [hep-ex].
- 2220 [21] Guillaume Albouy et al. “Theory, phenomenology, and experimental avenues for dark showers:  
 2221 a Snowmass 2021 report”. In: *The European Physical Journal C* 82.12 (Dec. 2022).
- 2222 [22] Timothy Cohen et al. “LHC searches for dark sector showers”. In: *Journal of High Energy  
 2223 Physics* 2017.11 (Nov. 2017).
- 2224 [23] Lyndon Evans and Philip Bryant. “LHC Machine”. In: *Journal of Instrumentation* 3.08  
 2225 (2008), S08001.
- 2226 [24] “The ATLAS Experiment at the CERN Large Hadron Collider”. In: *JINST* 3 (2008). Also  
 2227 published by CERN Geneva in 2010, S08003.
- 2228 [25] “The CMS experiment at the CERN LHC”. In: *Journal of Instrumentation* 3.08 (2008),  
 2229 S08004.
- 2230 [26] “The ALICE experiment at the CERN LHC”. In: *Journal of Instrumentation* 3.08 (2008),  
 2231 S08002.
- 2232 [27] “The LHCb Detector at the LHC”. In: *Journal of Instrumentation* 3.08 (2008), S08005.
- 2233 [28] Ana Lopes and Melissa Loyse Perrey. *FAQ-LHC The guide*. 2022.

- 2234 [29] Esma Mobs. “The CERN accelerator complex in 2019. Complexe des accélérateurs du  
2235 CERN en 2019”. In: (2019). General Photo.
- 2236 [30] *Pulling together: Super Conducting electromagnets*. <https://home.cern/science/engineering/pulling-together-superconducting-electromagnets>.  
2237 Accessed: 2024-01-05.
- 2238
- 2239 [31] *The High-Luminosity LHC*. <https://voisins.web.cern.ch/en/high-luminosity-lhc-hl-lhc>. Accessed: 2024-01-05.
- 2240
- 2241 [32] Aad G., et al. (ATLAS Collaboration and CMS Collaboration). “Combined Measurement of  
2242 the Higgs Boson Mass in pp Collisions at  $\sqrt{s} = 7$  and 8 TeV with the ATLAS and CMS  
2243 Experiments”. In: *Phys. Rev. Lett.* 114 (19 2015), p. 191803.
- 2244 [33] O. Aberle et al. *High-Luminosity Large Hadron Collider (HL-LHC): Technical design re-*  
2245 *port*. CERN Yellow Reports: Monographs. Geneva: CERN, 2020.
- 2246 [34] The ATLAS Collaboration. “The ATLAS Experiment at the CERN Large Hadron Collider”.  
2247 In: *Journal of Instrumentation* 3.08 (2008), S08003.
- 2248 [35] G Aad, B Abbott, and ATLAS Collaboration. “Performance of the reconstruction of large  
2249 impact parameter tracks in the inner detector of ATLAS”. In: *Eur. Phys. J. C Part. Fields*  
2250 83.11 (Nov. 2023).
- 2251 [36] Joao Pequenao. *Computer Generated image of the ATLAS calorimeter*. 2008.
- 2252 [37] *ATLAS liquid-argon calorimeter: Technical Design Report*. Technical design report. AT-  
2253 LAS. Geneva: CERN, 1996.
- 2254 [38] H A Gordon. “Liquid argon calorimetry for the SSC”. In: () .
- 2255 [39] Henric Wilkens and (on behalf of the ATLAS LArg Collaboration). “The ATLAS Liquid  
2256 Argon calorimeter: An overview”. In: *Journal of Physics: Conference Series* 160.1 (2009),  
2257 p. 012043.
- 2258 [40] *Technical Design Report for the Phase-II Upgrade of the ATLAS Tile Calorimeter*. Tech.  
2259 rep. Geneva: CERN, 2017.
- 2260 [41] “Technical Design Report for the Phase-II Upgrade of the ATLAS Muon Spectrometer”. In:  
2261 () .
- 2262 [42] L Pontecorvo. “The ATLAS Muon Spectrometer”. In: (2004). revised version number 1  
2263 submitted on 2003-07-27 16:31:16.

- 2264 [43] *ATLAS magnet system: Technical Design Report, 1*. Technical design report. ATLAS. Geneva:  
 2265 CERN, 1997.
- 2266 [44] 2024.
- 2267 [45] Tommaso Colombo. “Data-flow Performance Optimisation on Unreliable Networks: the AT-  
 2268 LAS Data-Acquisition Case”. In: *Journal of Physics: Conference Series* 608 (May 2015),  
 2269 p. 012005.
- 2270 [46] Joao Pequenao. “Event Cross Section in a computer generated image of the ATLAS detec-  
 2271 tor.” 2008.
- 2272 [47] ATLAS Collaboration. “ATLAS Experiment Implements Heterogeneous Particle Recon-  
 2273 struction with Intel oneAPI Tools”. General Photo. 2023.
- 2274 [48] ATLAS Collaboration. “Electron and photon performance measurements with the ATLAS  
 2275 detector using the 2015–2017 LHC proton-proton collision data”. In: *Journal of Instrumen-*  
 2276 *tation* 14.12 (2019), P12006.
- 2277 [49] Chiara Deponte. “Studies on the properties of non-prompt photons at the ATLAS experi-  
 2278 ment”. Presented 16 Aug 2022. Technische Universitaet Dortmund (DE), 2022.
- 2279 [50] ATLAS Collaboration. “Muon reconstruction performance of the ATLAS detector in pro-  
 ton–proton collision data at  $\sqrt{s} = 13 \text{ TeV}$ ”. In: *The European Physical Journal C* 76.5 (2016).
- 2280 [51] Sebastien Rettie. *Muon identification and performance in the ATLAS experiment*. Tech. rep.  
 2281 Geneva: CERN, 2018.
- 2282 [52] B. R. Webber. *Fragmentation and Hadronization*. 1999. arXiv: hep-ph/9912292 [hep-ph].
- 2283 [53] Eric M. Metodiev. *The Fractal Lives of Jets* | Eric M. Metodiev — ericmetodiev.com. <https://www.ericmetodiev.com/post/jetformation/>. 2019, note = [Accessed 18-  
 2284 05-2024],
- 2285 [54] Steven Schramm. *ATLAS Jet Reconstruction, Calibration, and Tagging of Lorentz-boosted  
 Objects*. Tech. rep. Geneva: CERN, 2017.
- 2286 [55] ATLAS Collaboration. “Topological cell clustering in the ATLAS calorimeters and its per-  
 2287 formance in LHC Run 1”. In: *The European Physical Journal C* 77.7 (July 2017).
- 2288 [56] ATLAS Collaboration. “Jet reconstruction and performance using particle flow with the  
 2289 ATLAS Detector”. In: *The European Physical Journal C* 77.7 (July 2017).

- 2292 [57] Matteo Cacciari, Gavin P Salam, and Gregory Soyez. “The anti-ktjet clustering algorithm”.  
2293 In: *Journal of High Energy Physics* 2008.04 (Apr. 2008), 063–063.
- 2294 [58] Matteo Cacciari, Gavin P. Salam, and Gregory Soyez. “FastJet user manual: (for version  
2295 3.0.2)”. In: *The European Physical Journal C* 72.3 (Mar. 2012).
- 2296 [59] Stephen D. Ellis and Davison E. Soper. “Successive combination jet algorithm for hadron  
2297 collisions”. In: *Physical Review D* 48.7 (Oct. 1993), 3160–3166.
- 2298 [60] M. Wobisch and T. Wengler. *Hadronization Corrections to Jet Cross Sections in Deep-*  
2299 *Inelastic Scattering*. 1999. arXiv: hep-ph/9907280 [hep-ph].
- 2300 [61] Gavin P Salam and Gr  gory Soyez. “A practical seedless infrared-safe cone jet algorithm”.  
2301 In: *Journal of High Energy Physics* 2007.05 (May 2007), 086–086.
- 2302 [62] Gavin P. Salam. “Towards jetography”. In: *The European Physical Journal C* 67.3–4 (May  
2303 2010), 637–686.
- 2304 [63] *A Monte Carlo study of track association to jets for b-tagging*. Tech. rep. Geneva: CERN,  
2305 2021.
- 2306 [64] *Flavor Tagging with Track Jets in Boosted Topologies with the ATLAS Detector*. Tech. rep.  
2307 All figures including auxiliary figures are available at <https://atlas.web.cern.ch/Atlas/GROUPS/PHYSICS/P>  
2308 PHYS-PUB-2014-013. Geneva: CERN, 2014.
- 2309 [65] ATLAS Collaboration. “Performance of missing transverse momentum reconstruction with  
2310 the ATLAS detector using proton-proton collisions at  $\sqrt{s} = 13$  TeV”. In: *Eur. Phys. J. C*  
2311 78.11 (2018), p. 903. arXiv: 1802.08168.
- 2312 [66] ATLAS Collaboration. *Public atlas luminosity results for run-2 of the LHC*. 2024.
- 2313 [67] GEANT4 Collaboration, S. Agostinelli, et al. “GEANT4 – a simulation toolkit”. In: *Nucl.*  
2314 *Instrum. Meth. A* 506 (2003), p. 250.
- 2315 [68] Christian Bierlich et al. *A comprehensive guide to the physics and usage of PYTHIA 8.3*.  
2316 2022. arXiv: 2203.11601 [hep-ph].
- 2317 [69] Michelangelo L. Mangano, Mauro Moretti, and Roberto Pittau. “Multijet matrix elements  
2318 and shower evolution in hadronic collisions: -jets as a case study”. In: *Nuclear Physics B*  
2319 632.1–3 (June 2002), 343–362.
- 2320 [70] The CMS Collaboration. “Search for resonant production of strongly coupled dark matter  
2321 in proton-proton collisions at 13 TeV”. In: *Journal of High Energy Physics* 2022.6 (June  
2322 2022).

- 2323 [71] The ATLAS Collaboration. “Search for non-resonant production of semi-visible jets using  
2324 Run 2 data in ATLAS”. In: *Physics Letters B* 848 (Jan. 2024), p. 138324.
- 2325 [72] J. Alwall et al. “The automated computation of tree-level and next-to-leading order differ-  
2326 ential cross sections, and their matching to parton shower simulations”. In: *JHEP* 07 (2014),  
2327 p. 079. arXiv: 1405.0301 [hep-ph].
- 2328 [73] Jon Butterworth et al. “PDF4LHC recommendations for LHC Run II”. In: *J. Phys. G* 43  
2329 (2016), p. 023001. arXiv: 1510.03865 [hep-ph].
- 2330 [74] Peter Skands, Stefano Carrazza, and Juan Rojo. “Tuning PYTHIA 8.1: the Monash 2013  
2331 Tune”. In: *Eur. Phys. J. C* 74.8 (2014), p. 3024. arXiv: 1404.5630 [hep-ph].
- 2332 [75] Yann LeCun, Yoshua Bengio, and Geoffrey Hinton. “Deep learning”. In: *nature* 521.7553  
2333 (2015), p. 436.
- 2334 [76] Jonathan Johnson. *What’s a deep neural network? Deep Nets explained*. 2020.
- 2335 [77] .
- 2336 [78] Dor Bank, Noam Koenigstein, and Raja Giryes. *Autoencoders*. 2021. arXiv: 2003.05991  
2337 [cs.LG].
- 2338 [79] A. Kahn et al. “Anomalous jet identification via sequence modeling”. In: *Journal of Instru-  
2339 mentation* 16.08 (Aug. 2021), P08012.
- 2340 [80] Patrick T. Komiske, Eric M. Metodiev, and Jesse Thaler. “Energy flow networks: deep sets  
2341 for particle jets”. In: *Journal of High Energy Physics* 2019.1 (2019).
- 2342 [81] F. Pedregosa et al. “Scikit-learn: Machine Learning in Python”. In: *Journal of Machine  
2343 Learning Research* 12 (2011), pp. 2825–2830.
- 2344 [82] Diederik P. Kingma and Jimmy Ba. *Adam: A Method for Stochastic Optimization*. 2017.  
2345 arXiv: 1412.6980 [cs.LG].
- 2346 [83] Diederik P Kingma and Max Welling. *Auto-Encoding Variational Bayes*. 2022. arXiv: 1312.  
2347 6114 [stat.ML].
- 2348 [84] Georges Aad et al. “Anomaly detection search for new resonances decaying into a Higgs  
2349 boson and a generic new particle  $X$  in hadronic final states using  $\sqrt{s} = 13$  TeV  $pp$  collisions  
2350 with the ATLAS detector”. In: *Phys. Rev. D* 108 (2023), p. 052009. arXiv: 2306.03637  
2351 [hep-ex].

- 2352 [85] *Selection of jets produced in 13TeV proton-proton collisions with the ATLAS detector*. Tech.  
 2353 rep. All figures including auxiliary figures are available at <https://atlas.web.cern.ch/Atlas/GROUPS/PHYSIC>  
 2354 CONF-2015-029. Geneva: CERN, 2015.
- 2355 [86] Georgios Choudalakis. *On hypothesis testing, trials factor, hypertests and the BumpHunter*.  
 2356 2011. arXiv: 1101.0390.
- 2357 [87] Peter Loch. “Jet measurements in ATLAS”. In: *J. Phys. Conf. Ser.* 323 (2011). Ed. by Gior-  
 2358 gio Bellettini, p. 012002.
- 2359 [88] The ATLAS Collaboration. “Search for diboson resonances in hadronic final states in 139  
 2360 fb-1 of  $pp$  collisions at  $\sqrt{s} = 13$  TeV with the ATLAS detector”. In: *Journal of High Energy*  
 2361 *Physics* 2019.9 (Sept. 2019).
- 2362 [89] *Recommendations for the Modeling of Smooth Backgrounds*. Tech. rep. Geneva: CERN,  
 2363 2020.
- 2364 [90] Glen Cowan et al. “Asymptotic formulae for likelihood-based tests of new physics”. In: *The*  
 2365 *European Physical Journal C* 71.2 (Feb. 2011).
- 2366 [91] Ryan Edgar et al. *Functional Decomposition: A new method for search and limit setting*.  
 2367 2018. arXiv: 1805.04536 [physics.data-an].
- [92] “Dijet Resonance Search with Weak Supervision Using  
 $\sqrt{s} = 13$   
 2368  $pp$  Collisions in the ATLAS Detector”. In: *Physical Review Letters* 125.13 (Sept. 2020).
- 2369 [93] The ATLAS Collaboration. “Jet energy scale and resolution measured in proton–proton col-  
 2370 lisions at  
 $\sqrt{s} = 13$   
 2371 TeV with the ATLAS detector”. In: *The European Physical Journal C* 81.8 (Aug. 2021).
- [94] The ATLAS Collaboration. “Luminosity determination in pp collisions at  
 $\sqrt{s} = 13$   
 2370 TeV using the ATLAS detector at the LHC”. In: *The European Physical Journal C* 83.10  
 2371 (Oct. 2023).
- 2372 [95] S. Mrenna and P. Skands. “Automated parton-shower variations in pythia 8”. In: *Physical*  
 2373 *Review D* 94.7 (Oct. 2016).

- 2374 [96] *ATLAS Pythia 8 tunes to 7 TeV data*. Tech. rep. All figures including auxiliary figures are  
2375 available at <https://atlas.web.cern.ch/Atlas/GROUPS/PHYSICS/PUBNOTES/ATL-PHYS->  
2376 PUB-2014-021. Geneva: CERN, 2014.
- 2377 [97] A L Read. “Presentation of search results: the CLs technique”. In: *Journal of Physics G: Nuclear and Particle Physics* 28.10 (2002), p. 2693.  
2378
- 2379 [98] *Procedure for the LHC Higgs boson search combination in Summer 2011*. Tech. rep. Geneva:  
2380 CERN, 2011.

## Appendix A: Trigger Studies

2383 Both the lowest unprescaled  $E_T^{\text{miss}}$  and single small-R jet triggers were considered for this  
 2384 analysis. The  $E_T^{\text{miss}}$  trigger is observed to have higher efficiency for low mass, high  $R_{\text{inv}}$  points,  
 2385 while the single small-R trigger favors high mass, low  $R_{\text{inv}}$  points. Figure A.1 shows the yields  
 2386 and signal efficiencies across the grid for both these strategies.

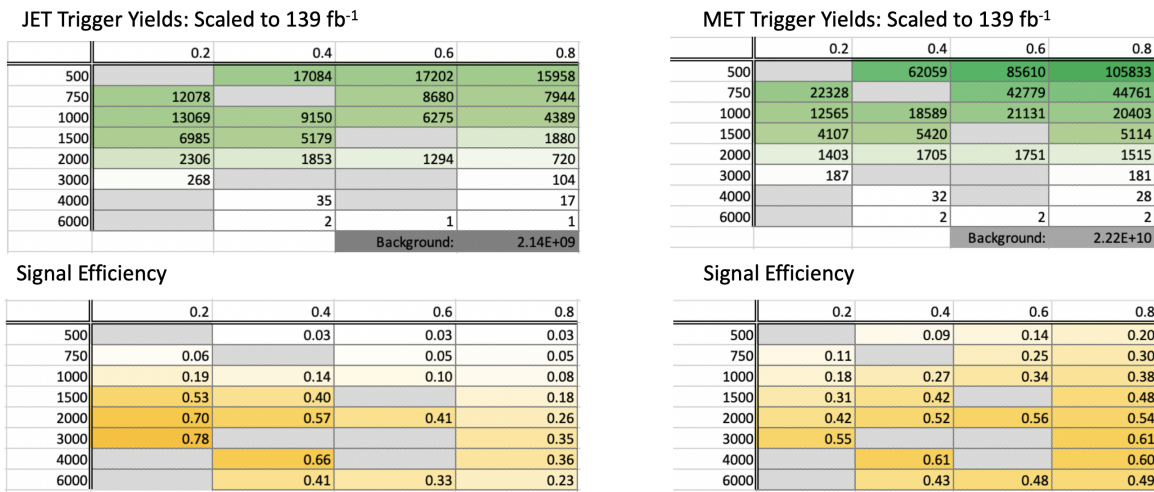


Figure A.1: Trigger yield and efficiency for both the MET trigger and small-R jet trigger approach. Each entry represent a signal point, labelled by the  $Z'$  mass and the  $R_{\text{inv}}$  fraction.

2387 The cross section is higher for the lower  $Z'$  mass signal points. As a result, our sensitivity  
 2388 to these points and ability to set limits on them is already naturally enhanced. Figure A.2 shows  
 2389 the factor of improvement in the inclusive  $S/\sqrt{B}$  using each trigger strategy. A cross-check was  
 2390 also done calculating  $S/\sqrt{B}$  in windows around the mT mass. The results of this cross-check  
 2391 confirmed the results shown in Figure A.2.

2392 Figure A.3 shows the ratio of  $S/\sqrt{B}$  across the signal grid for the jet trigger compared to the  
 2393  $E_T^{\text{miss}}$  trigger.

2394 This plot makes clear that the  $E_T^{\text{miss}}$  trigger favors the low mass, high  $R_{\text{inv}}$  signal points, while

$(\text{JET Trigger } S/\sqrt{B}) / (\text{Untriggered } S/\sqrt{B})$				
	0.2	0.4	0.6	0.8
500		1.26	1.43	1.53
750	2.99		2.52	2.68
1000	9.24	6.74	5.03	4.07
1500	26.45	20.15		8.83
2000	34.66	28.24	20.57	12.85
3000	39.05			17.35
4000		32.94		17.96
6000		20.57	16.55	11.53

$(\text{MET Trigger } S/\sqrt{B}) / (\text{Untriggered } S/\sqrt{B})$				
	0.2	0.4	0.6	0.8
500		1.43	2.21	3.15
750	1.72		3.86	4.69
1000	2.76	4.26	5.26	5.89
1500	4.83	6.56		7.47
2000	6.55	8.08	8.65	8.40
3000	8.46			9.38
4000		9.51		9.32
6000		6.68	7.43	7.59

Figure A.2: The factor of improvement in  $S/\sqrt{B}$  for each trigger method compared to the untriggered case.

	0.2	0.4	0.6	0.8
500		0.89	0.65	0.49
750	1.74		0.65	0.57
1000	3.35	1.58	0.96	0.69
1500	5.47	3.07		1.18
2000	5.29	3.49	2.38	1.53
3000	4.62			1.85
4000		3.46		1.93
6000		3.08	2.23	1.52

Figure A.3: The ratio of  $S/\sqrt{B}$  of jet trigger over  $E_T^{\text{miss}}$  trigger selection.

2395 the single jet trigger favors the high mass, low  $R_{inv}$  signal points. A number of considerations led  
2396 us to selecting the single jet trigger. First, Figure A.2 illustrates that the sensitivity enhancement is  
2397 greater for signals favored by the jet trigger than signals favored by the  $E_T^{\text{miss}}$  trigger. This indicates  
2398 we have more to gain from focusing on the region of our signal grid where the jet trigger is most  
2399 efficient. We combined this with the observation that the jet trigger is beneficial for high mass  
2400 points where the cross-section is lower and we need to maximize sensitivity to hope to set limits  
2401 on these points.

2402 Second, there are a number of analysis variables at our disposal which are more discriminant for  
2403 high  $R_{inv}$  signals than for low  $R_{inv}$  signals. A collection of these variables are shown in Figure A.4.  
2404 Given that we had multiple avenues available to enhance sensitivity to low  $R_{inv}$  signals through  
2405 analysis strategy cuts, we opted for a trigger strategy that benefitted the low  $R_{inv}$  signal points.  
2406 Additionally, we know  $E_T^{\text{miss}}$  is highly correlated with these discriminant analysis variables, and a  
2407  $E_T^{\text{miss}}$  trigger would reduce the effectiveness of these variables. Not implementing the  $E_T^{\text{miss}}$  trigger  
2408 allows us to explore other ways of leveraging  $E_T^{\text{miss}}$  in the analysis using a cut that is more finely  
2409 tuned to the specifics of the signal model than the  $E_T^{\text{miss}}$  trigger is.

2410 Third, we know that fitting the high  $R_{inv}$  mass points would be challenging given their very  
2411 broad shapes in the key analysis variable  $m_T$ . Given the analysis decision to do a search for  
2412 resonant features in  $m_T$ , we chose to design a search that emphasized maximizing sensitivity  
2413 to the signal points that we were mostly to appear as a resonant feature in  $m_T$ . The shape of  
2414  $m_T$  and our reduced ability to set limits on high  $R_{inv}$  points is demonstrated in the body of this  
2415 note. Another search strategy may be more optimal for setting limits on high  $R_{inv}$  semi-visible jet  
2416 signals, but it is currently outside the scope of this analysis.

2417 A jet or  $E_T^{\text{miss}}$  trigger was also considered, but abandoned due to concerns about sculpting  
2418 features in the smoothly falling  $E_T^{\text{miss}}$  or leading jet  $p_T$  distributions, as shown in Figure A.5.

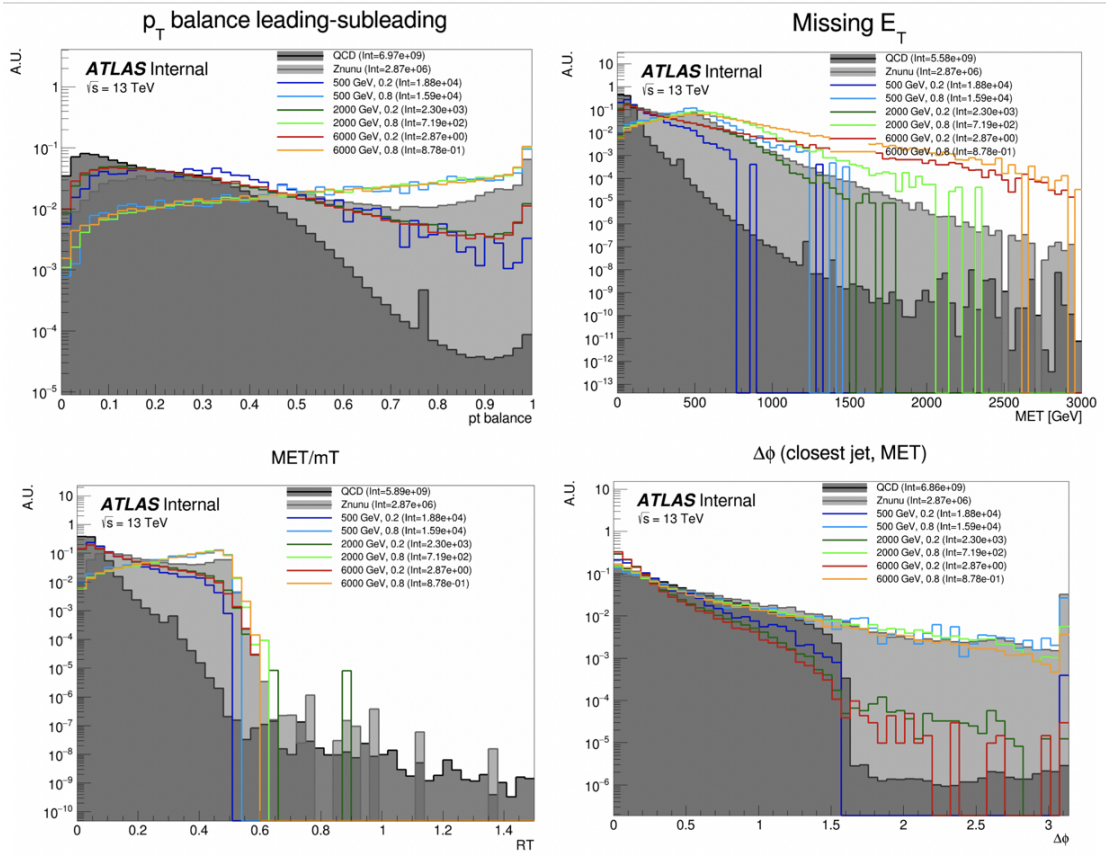


Figure A.4: Analysis variables where high  $R_{inv}$  signals a clearly distinct from background and low  $R_{inv}$  variables. On the contrary, leading jet  $p_T$  is one of the only variables where low  $R_{inv}$  signals are distinct from background.

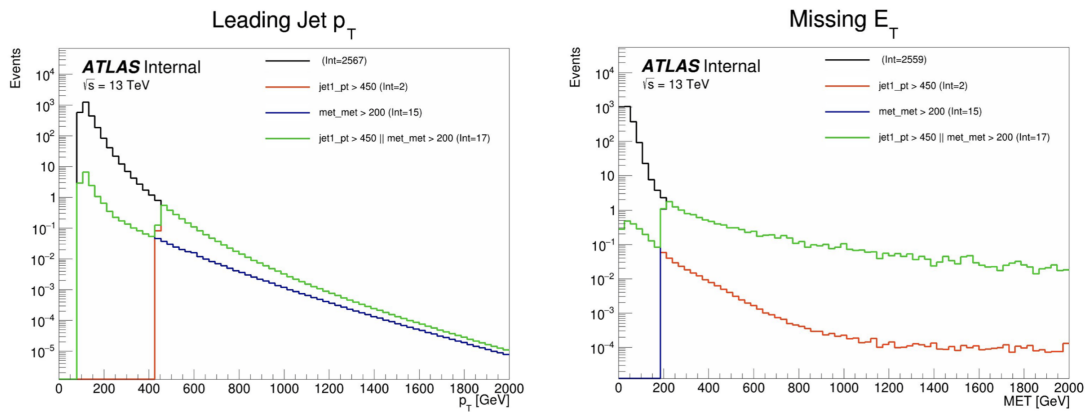


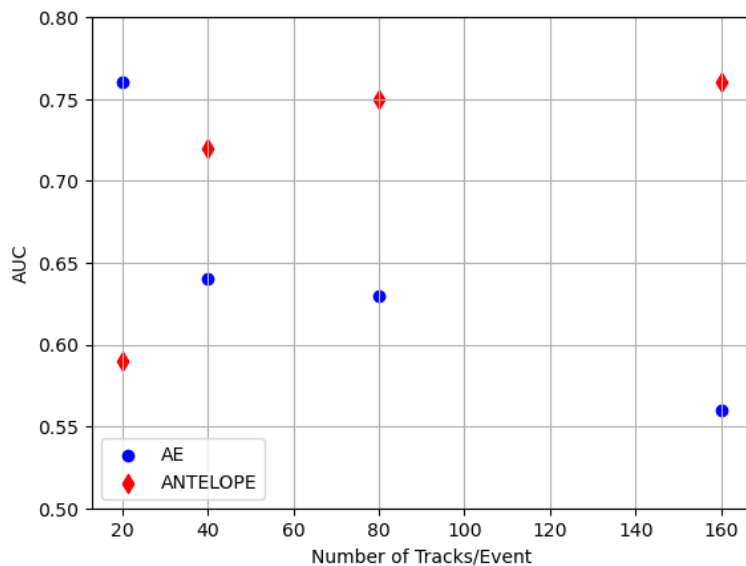
Figure A.5: OR of jet and  $E_T^{\text{miss}}$  triggers.

## Appendix B: Machine Learning Approaches

### 2421 B.1 Unsupervised: AE vs. ANTELOPE

2422 To understand the benefits of the semi-supervised ANTELOPE approach, we study the AN-  
 2423 TELOPE in comparison to a traditional anomaly detection architecture like an autoencoder. The  
 2424 autoencoder cannot accommodate variable length or permutation invariant inputs.

2425 Figure B.1 shows the AUC determined by each of these two tools as a function of number  
 2426 of tracks. The trend is that the AE suffers when more information is given, due to the presence  
 2427 of 0-padding. In contrast, the ANTELOPE architecture performs better with more information,  
 motivating the use of high dimensional input modelin with this method.

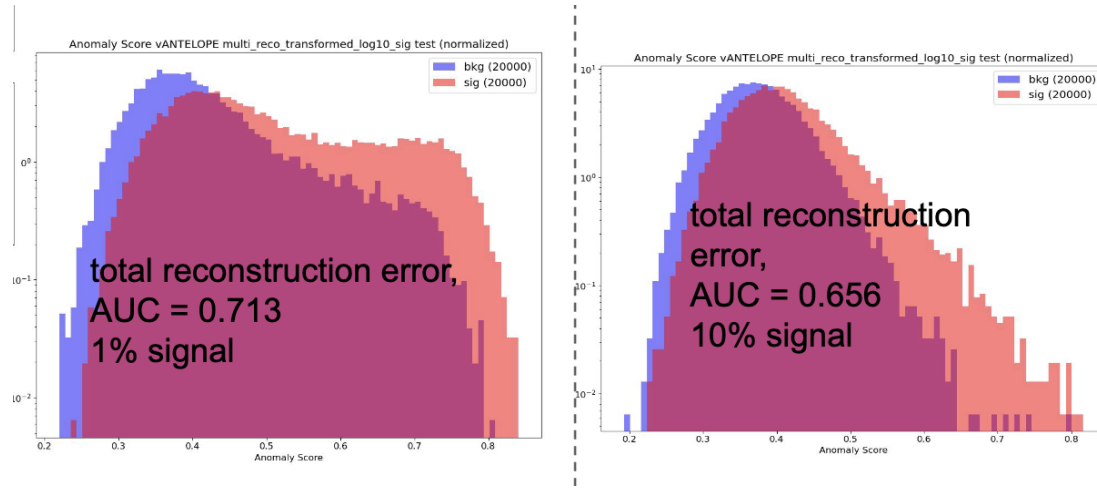


- Confirms that AE is negatively sensitive to zero padding while ANTELOPE sees a performance improvement as it sees more “information”

2428  
Figure B.1

2429    **B.1.1 Signal Contamination**

2430    To understand the effect of signal contamination in training on the ANTELOPE score, we inject  
2431    a percent of signal events into the data used to train the ANTELOPE autoencoder stage and look  
2432    at the AUC on signals. Figure B.2 shows no variation in AUC with 1% contamination in training  
data, but a few % drop going up to 10%.



2433    Figure B.2

2434    **B.2 PFN Optimality Checks**

2435    Studies were done to ensure the relatively optimality of the single PFN model, trained over  
2436    combined signals, across the grid. As the grid spans signals with a large range of  $E_T^{\text{miss}}$ , their vary-  
2437    ing input features and background composition may be conducive to separate PFN models trained  
2438    on high and low  $E_T^{\text{miss}}$  signal points to better capture the signal-background differences. Figure B.3  
2439    shows a comparison of the signal-inclusive PFN model performance and the performance of mod-  
2440    els separated into high and low  $R_{\text{inv}}$  signals in training. The most notable impact is found for the  
2441    low  $R_{\text{inv}}$  and high mass points, indicating that the signal-inclusive PFN is learning morning about  
2442    the distinction between high- $E_T^{\text{miss}}$  signals and backgrounds. However, these high mass points are  
2443    also the most challenging to find due to their very wide resonance on top of  $m_T$ , and in the final  
2444    projected sensitivity in the  $m_T$  window the differences are < 10% across the grid. To maintain a

2445 harmonized strategy with the ANTELOPE region we keep the inclusive PFN model as the final  
 2446 version.

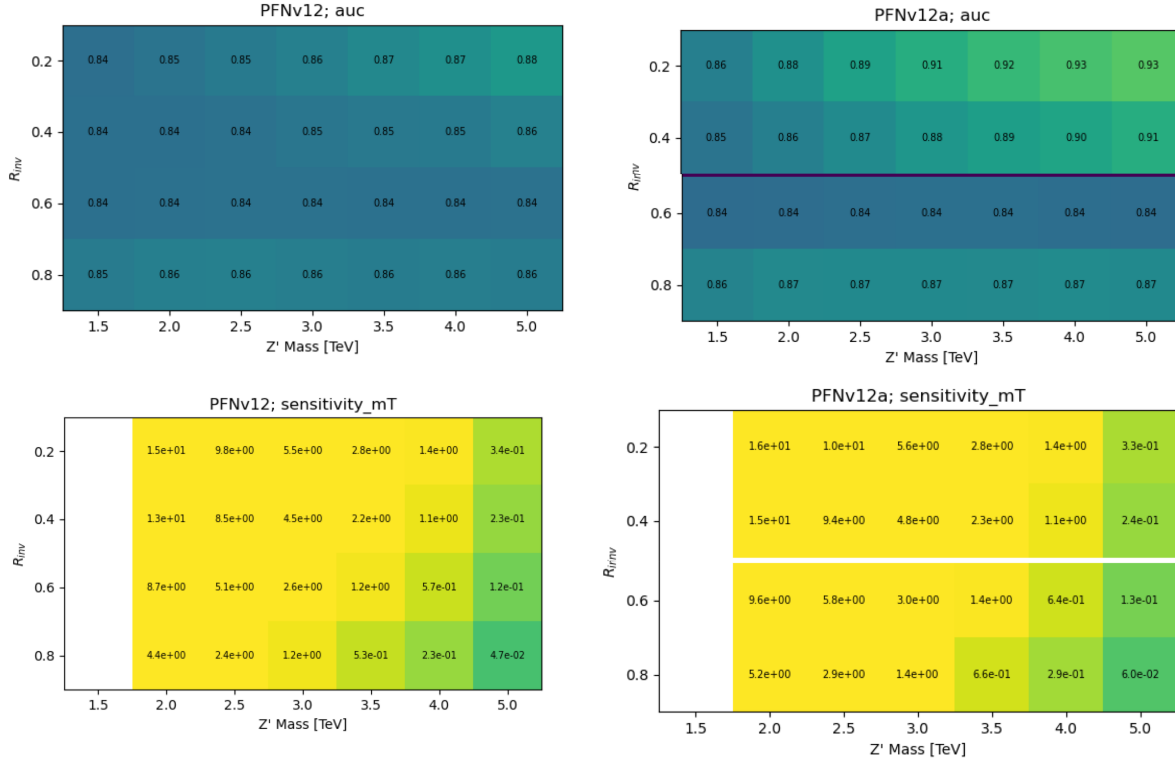


Figure B.3: Comparison of PFN AUC (top) and sensitivity in the  $m_T$  mass window (bottom) for a single PFN model (left) vs. two models trained on  $R_{inv} < 0.5$  and  $> 0.5$  separately (right).

2447 Grid scans for optimality were also performed on the number of training epochs, number of  
 2448 training events, batch size, learning rate, number of neurons, and dimension of the  $\Phi$  space. The  
 2449 results of these scans are summarized in the tables in Figure B.4. The selected or default parameters  
 2450 were found to be optimal, or close enough to optimal to justify not increasing the training time or  
 2451 complexity of the network for negligible increases in performance.

### 2452 B.3 Single Jet vs Jet System ML Approach

2453 The analysis considered both a single jet and jet system ML approach. A jet system approach,  
 2454 where the leading two jets and their orientation with respect to each other was selected for a variety  
 2455 of reasons. The jet system approach captures the MET information which is crucial to identifying

	<b>default</b> s_events=500096 b_events=501396	s_events:49135 b_events: 48220 *	s_events:246205 b_events:245136
AUC	.905	.874	.892

	<b>default</b>	n_neuro n 40	n_neuro n 150	phi_dim 32	phi_dim 128	learning _rate 0.0005	learning _rate 0.002	nepochs 50	nepochs 200*
AUC	.905	.898	.906	.902	.906	.898	.905	.893	.909

	<b>default</b>	batchsize_pfn 250	batchsize_pfn 1000
AUC	.905	.903	.902

Figure B.4: Scans done to check for optimality of PFN training parameters.

2456 SVJs. In the topology where the dark quarks come from a heavy Z' decay and are back to back,  
 2457 the measurable MET will have to be aligned with one or the other.

2458 Additionally, the performance of both a supervised PFN approach and an unsupervised AE ap-  
 2459 proach was studied in the case of a single jet tagger. While the PFN approach was still performant  
 2460 on a single jet case, the unsupervised approach was significantly improved by using both jets. This  
 2461 is shown in Figure B.5.

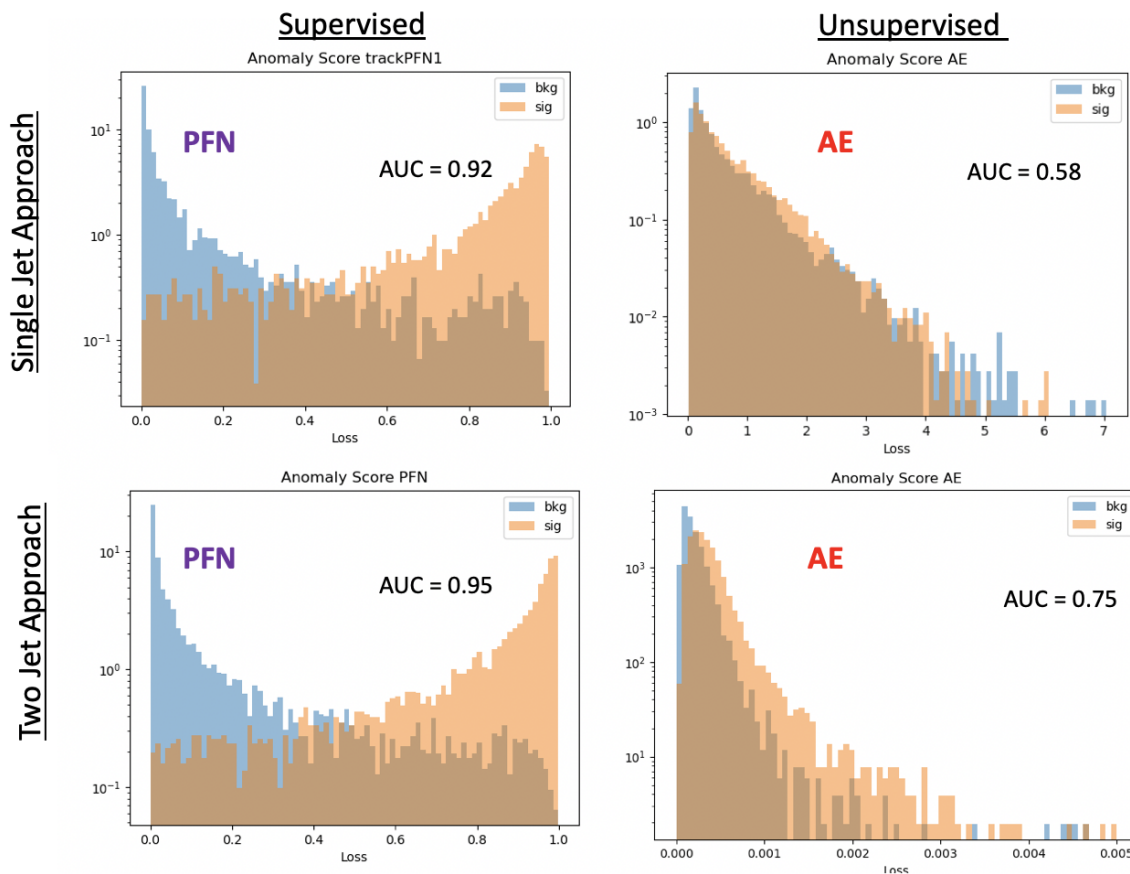


Figure B.5:  $\phi$  Performance comparison between single jet and jet system ML approach

#### 2462 B.4 PFN Training Composition

2463 The overall sensitivity and stability across the signal grid is observed to benefit by training the  
 2464 ML tool to reject only the dominant background, QCD. This is evidenced by the PFN response  
 2465 plots shown in Section 7.2 and the following AUC and sensitivity comparison plots in Figure B.6.

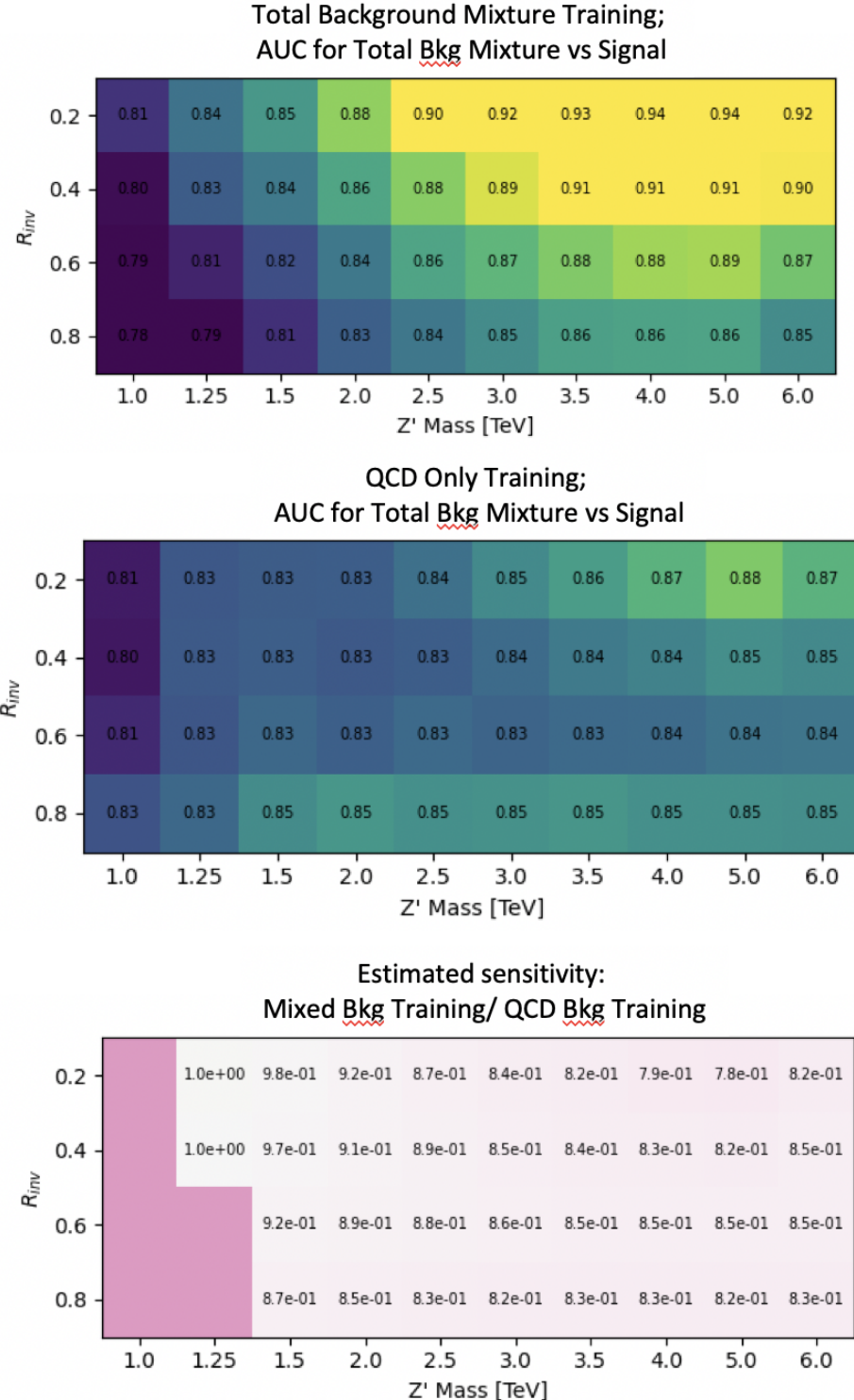


Figure B.6:  $\phi$  Comparison in the AUC score across the grid for the mixed background strategy vs the QCD only strategy. The bottom table highlights that the QCD only strategy gives superior sensitivity across the signal grid.

2466 **B.5  $E_T^{\text{miss}}$  and  $E_T^{\text{miss}}\phi$  Shapes**

2467 The Tight cleaning working point was found to be necessary due to the nature of our signal  
 2468 being  $E_T^{\text{miss}}$  and hadronic activity that are closely aligned, presenting a signature that is very af-  
 2469 fected by beam-induced background (BIB). As per the cleaning recommendations, any event with  
 2470 a jet that fails Tight criteria is rejected. Figure B.7 shows the effect of Tight cleaning on the shape  
 of  $E_T^{\text{miss}}$  in data, fixing a feature present in Loose cleaning only.

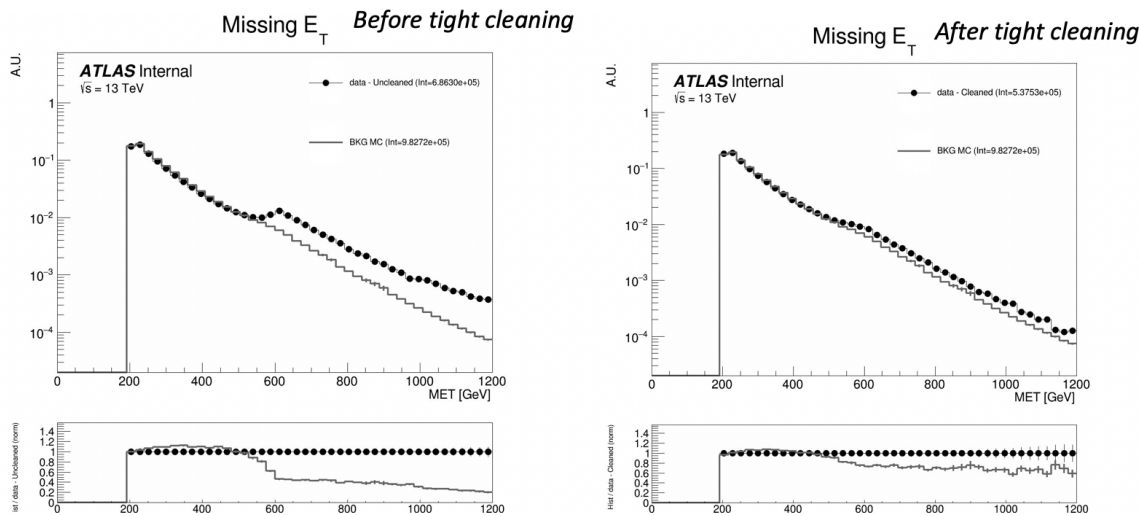


Figure B.7:  $E_T^{\text{miss}}$  in data before and after Tight event cleaning is applied.

2471  
 2472 Figure B.8 further illustrates the correlation between the excess events and the leading jet  $p_T$ ,  
 2473 and illustrates the impact of the tight cleaning in reducing this feature.

2474 Figure B.9 illustrates the 2D  $\eta$  vs  $\phi$  distribution of the leading and subleading jets before and  
 2475 after tight cleaning. No major spikes or hot areas are observed. One bright spot in the subleading  
 2476 jet map at  $\eta \approx 0$  and  $\phi \approx -1.0$  was studies and found to have no impact on the  $E_T^{\text{miss}}$  shape, indicating  
 2477 a likely missed spot in the Tile cleaning which does not affect  $E_T^{\text{miss}}$ .

2478 **B.5.1 NCB Preselection**

2479 A final preselection was derived to entirely remove the presence of non-collision background,  
 2480 particularly noted through its impact on the  $E_T^{\text{miss}}$  shape. Cuts are added on the subleading jet

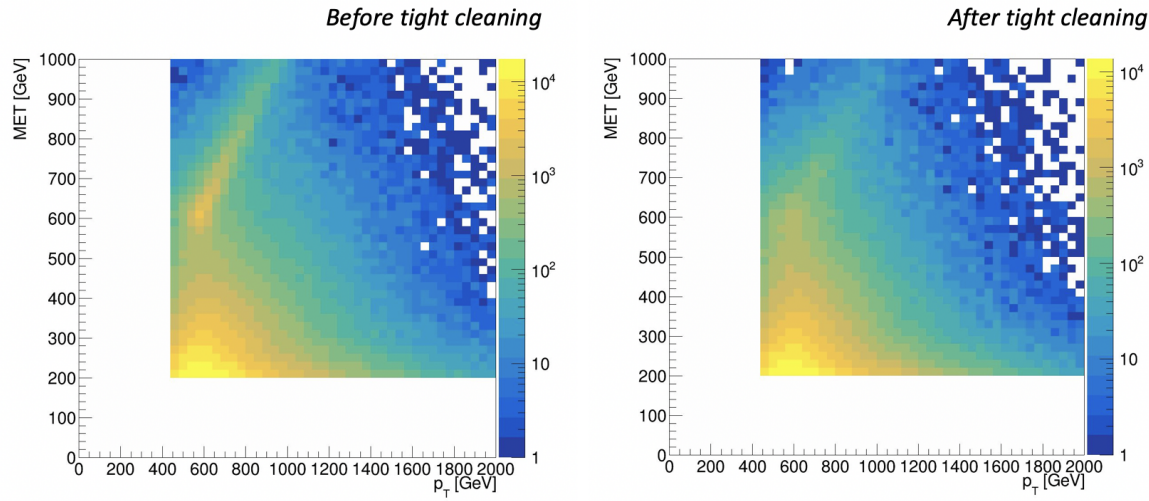


Figure B.8:  $E_T^{\text{miss}}$  vs jet1  $p_T$  in data before and after Tight event cleaning is applied.

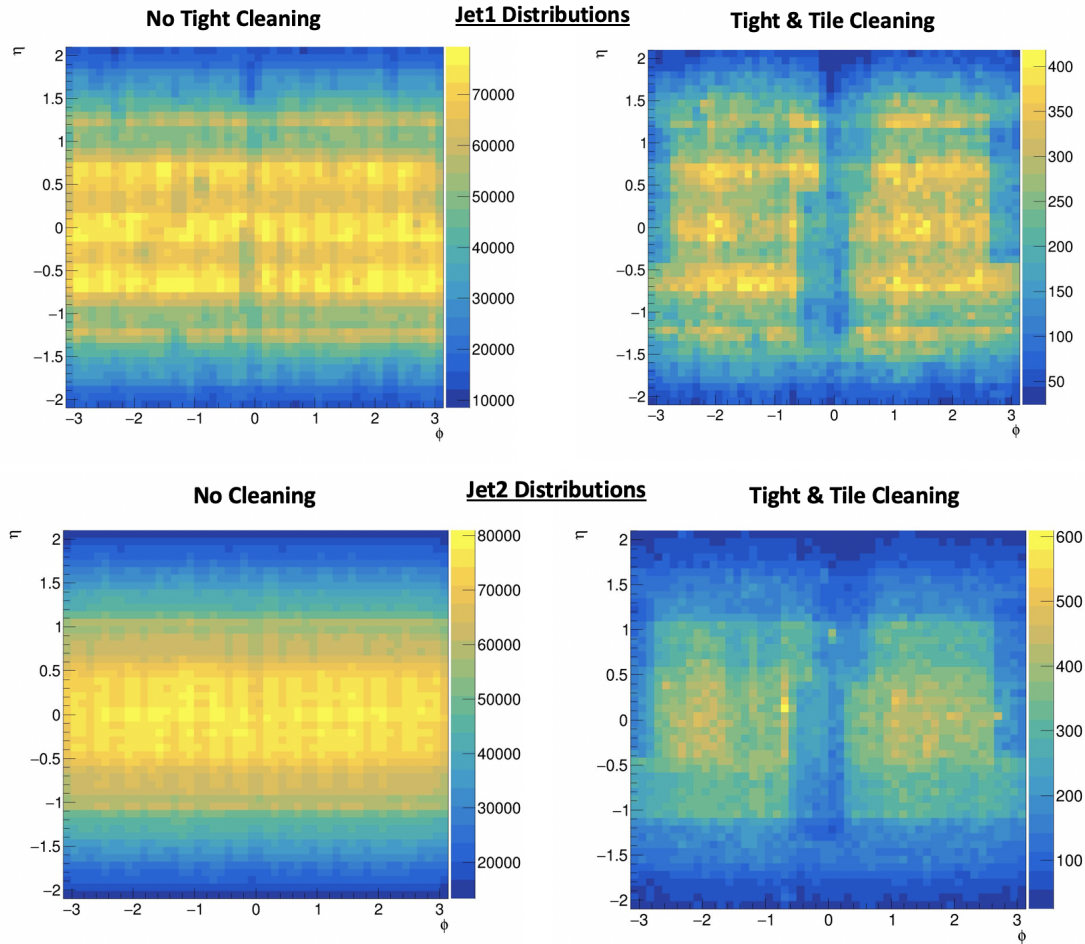


Figure B.9:  $\eta$  vs  $\phi$  for leading and subleading jets, before and after the application of tight cleaning.

2481  $p_T > 150$  GeV and  $\Delta\Phi(j1,j2) > 0.8$ . Figure B.10 shows the impact of these cuts to create a fully  
 2482 smoothly falling  $E_T^{\text{miss}}$  distribution. Figure B.11 shows the impact on the data yields in the CR and  
 2483 VR and several signals in the SR; the greatest inefficiencies are found for the signal points that are  
 2484 not sensitive in the analysis anyway. The reduction in background ultimately means that no impact  
 is noticed on the limits.

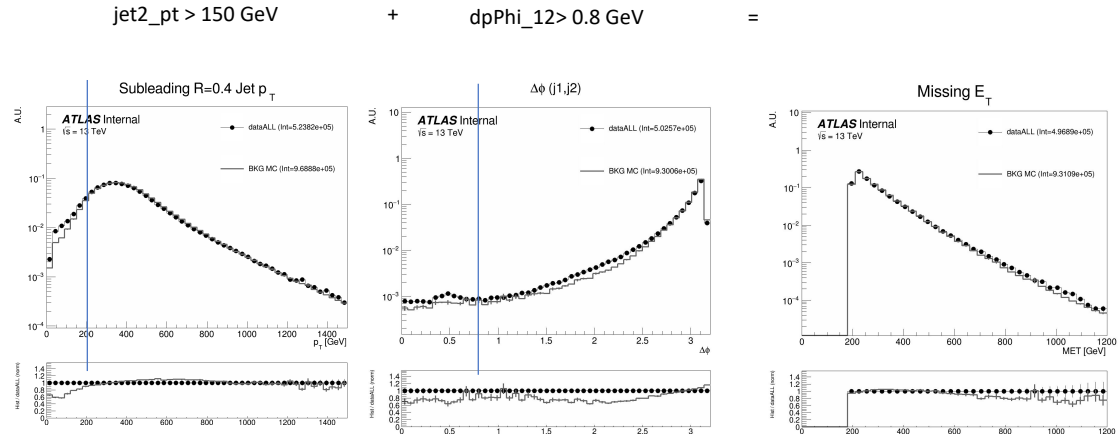


Figure B.10: Added NCB preselection and impact on  $E_T^{\text{miss}}$  shape.

2485  
 2486 Figure B.12 shows the impact of these cuts on the 2D  $E_T^{\text{miss}}$  vs jet1  $p_T$  distribution, where the  
 2487 feature is also observed to be smoothed.

2488 This strategy was discussed and signed off by the Jet/ $E_T^{\text{miss}}$  CP group<sup>1</sup>.

### 2489 B.5.2 TileCal Correction

2490 The  $E_T^{\text{miss}}\phi$  distribution was fixed through the implementation of an offline TileCal correction  
 2491 tool, which removes certain lumiblocks of certain runs based on poor functioning in TileCal mod-  
 2492 ules. Figure B.13 shows the  $E_T^{\text{miss}}\phi$  distribution in data across runs, before and after the application  
 2493 of the tool, showing the ability of the tool to remove spikes due to instrumental problems.

---

<sup>1</sup><https://indico.cern.ch/event/1413217/>

Region	Before Extra Cleaning Cuts	After Extra Cleaning Cuts	Efficiency
Data - CR	108957	107435	0.99
Data - VR	116917	116008	0.99
2500, 0.2 - SR	1921	1709	0.89
2500, 0.4 - SR	1819	1424	0.78
2500, 0.6 - SR	1150	735	0.64
2500, 0.8 - SR	543	251	0.46
5000, 0.2 - SR	21.5	20.3	0.94
5000, 0.4 - SR	22.3	19.4	0.87
5000, 0.6 - SR	16.0	11.6	0.73
5000, 0.8 - SR	8.1	4.1	0.51

Figure B.11: NCB preselection impact on data and signal yields.

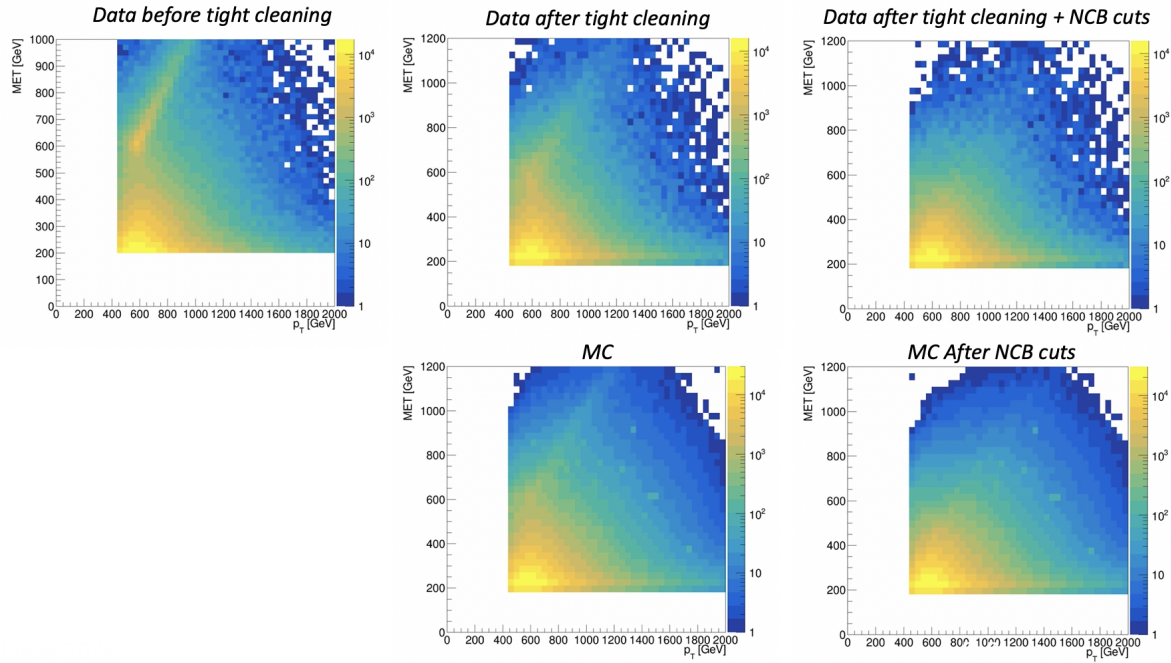


Figure B.12: Impact of tight cleaning and non-collision background preselection.

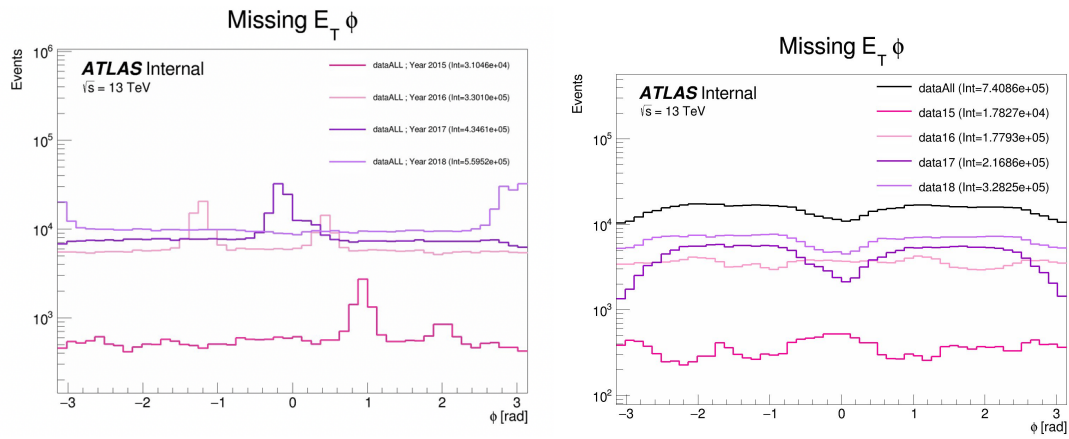


Figure B.13:  $E_T^{\text{miss}}\phi$  in data, before (left) and after (right) application of the TileCal correction tool.

2494

2495

## Appendix C: Truth Studies

### 2496 C.1 Jet dR Matching

2497 Figure C.1 demonstrates that the leading and subleading jet are overwhelmingly the most likely  
2498 jets to be matched to a dark quark.

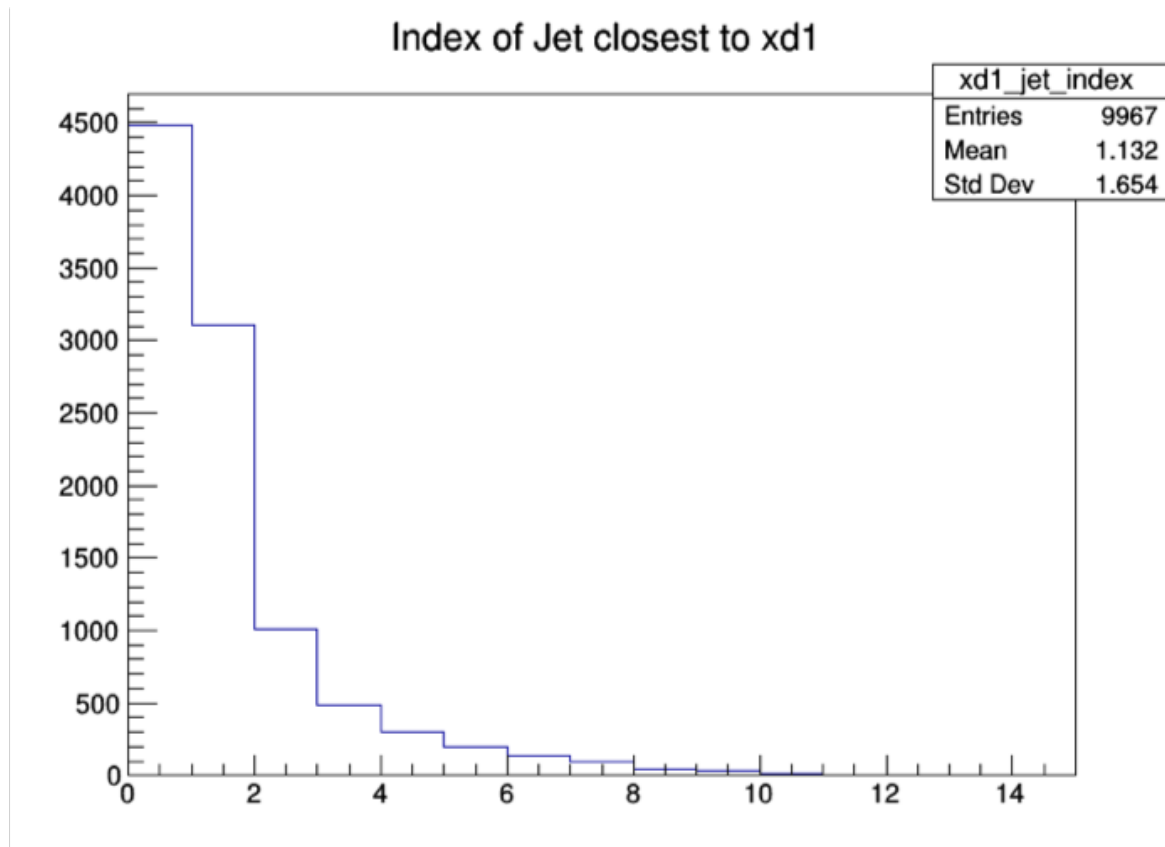


Figure C.1: Index of jets truth matched (by requirement of  $\Delta R < 0.4$ ) with dark quark.

2499 Other matching strategies were explored, such as choosing the jet most aligned with  $E_T^{\text{miss}}(\min$   
2500  $\Delta\phi(j, E_T^{\text{miss}}))$  and the jet most anti-aligned with  $E_T^{\text{miss}}(\max \Delta\phi(j, E_T^{\text{miss}}))$ . However, in most cases  
2501 these two measurements correspond to the subleading and leading jets respectively. Additionally,  
2502 as shown in Figure C.2 the leading/subleading strategy generally results in more matched jets than

2503 the  $E_T^{\text{miss}}$  aligned and  $E_T^{\text{miss}}$  anti-aligned strategy. Therefore the leading and subleading jets were  
 2504 chosen for consideration in this analysis.

<b>Signal (<math>M_{Z'}</math>, <math>r_{\text{inv}}</math>)</b>	<b>% Leading Jets <math>dR</math> Matched</b>	<b>% MET anti- aligned Jets <math>dR</math> matched</b>	<b>% Subleading Jets <math>dR</math> Matched</b>	<b>% MET aligned jets <math>dR</math> matched</b>
750 GeV, 0.2	<b>0.432883</b>	0.3567	<b>0.3777</b>	0.3504
750 GeV, 0.8	<b>0.187819</b>	0.1589	<b>0.1826</b>	0.1803
3500 GeV, 0.2	<b>0.692931</b>	0.5408	<b>0.5097</b>	0.4144
3500 GeV, 0.8	<b>0.344057</b>	0.2927	<b>0.2634</b>	0.2585
6000 GeV, 0.2	<b>0.647237</b>	0.5047	<b>0.4975</b>	0.3919
6000 GeV, 0.8	<b>0.345542</b>	0.2882	<b>0.2517</b>	0.249

Figure C.2: Percent of jets with  $\Delta R(j, E_T^{\text{miss}}) < 0.4$  comparing two jet identification strategies. Leading and subleading jets are seen to be the better metric for identifying jets associated with the dark quark decay.

## Appendix D: BumpHunter

### 2507 D.1 Signal Mass Resolution $m_T$ Binning

2508 In the discovery region, a binning for  $m_T$  is determined that is based on the expected signal  
 2509 width. This is done to improve the BumpHunter performance. The signal mass resolution for a  
 2510 given point is determined with a double-sided Crystal Ball fit to the mass. These fits are performed  
 2511 across  $Z'$  mass, and a linear fit to these values is performed to determine the optimal bin width  
 2512 across  $m_T$ .

2513 The x-axis value used is a data-driven way to determine the appropriate value of  $m_T$  for a given  
 2514 signal, given that the considerable  $E_T^{\text{miss}}$  from the dark particles means that the truth  $Z'$  mass does  
 2515 not well approximate the peak  $m_T$  value. The  $E_T^{\text{miss}}$  in the final state is generally an underestimate  
 2516 of the amount of energy that could be attributed to dark hadrons, as any dark hadrons that are  
 2517 back-to-back in the transverse plane will cancel out and not register as  $E_T^{\text{miss}}$ . Therefore  $m_T$  is  
 2518 always an underestimate of the  $Z'$  mass, so the truth  $Z'$  mass can be used as an upper bound. An  
 2519 integral is then performed backwards from that value until 60% of the total signal yield is included.  
 2520 This window is referred to as the 60% mass window; the mean of this window then provides an  
 2521 approximate localization of the signal mass peak in  $m_T$ . Figure D.1 shows some examples of this  
 2522 algorithm on several signal points of varying  $R_{\text{inv}}$  and mass.

2523 Figure D.2 shows the result of this linear fit for the four  $R_{\text{inv}}$  values considered in the signal  
 2524 grid. As expected, the resolution is considerably different for low and high  $R_{\text{inv}}$  points.

2525 A single  $m_T$  binning for the final SR plotting and BumpHunting is determined by selecting a  
 2526 harmonized binning at low  $m_T$ , and moving to wider bins at high  $m_T$ . As for higher  $R_{\text{inv}}$  signal  
 2527 points the mass resolution linear fit gives negative results, we require each bin to have a width of  
 2528 at least 100 GeV. Figure D.3 shows the resulting bins for each  $R_{\text{inv}}$  category that comes from the

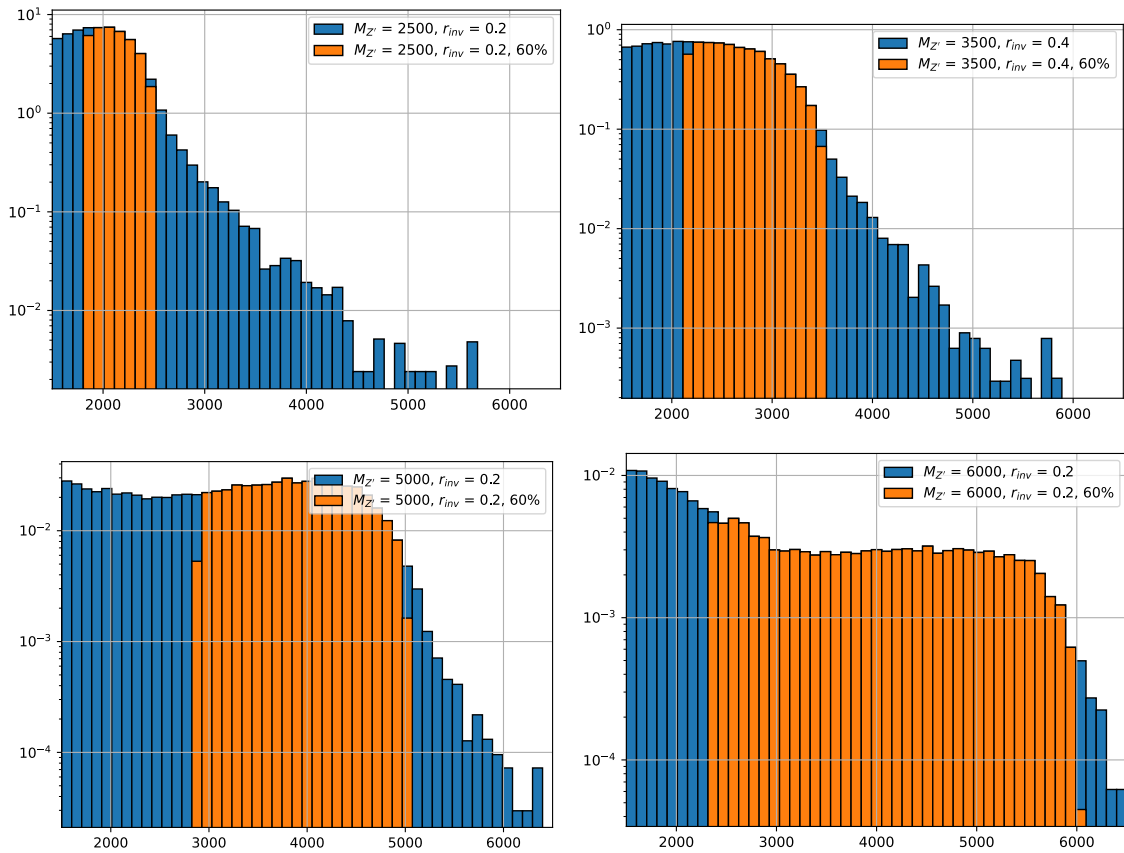


Figure D.1: Example determinations of the 60% mass window means for several signal points.

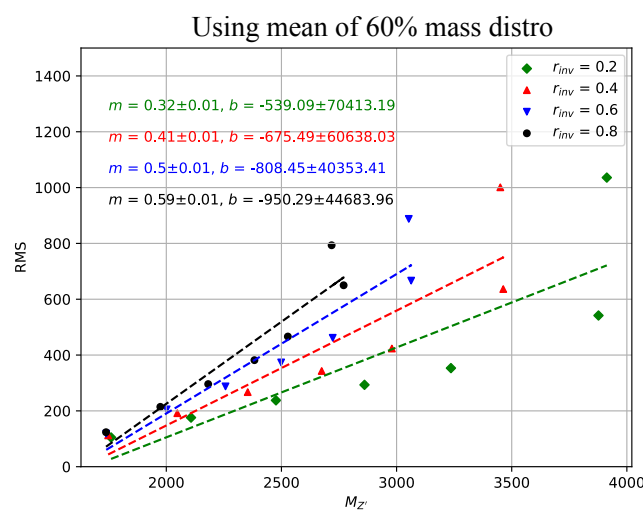


Figure D.2: Signal mass resolution for  $m_T$  binning for the signal grid in ( $R_{inv}$ , mass) space.

mass resolution fits, with the addition of the minimum 100 GeV bin width requirement.

$r_{inv} = 0.2 \rightarrow [1500, 1600, 1700, 1800, 1904, 2029, 2177, 2356, 2569, 2824, 3128, 3493, 3929, 4451, 5075, 5822, 6715]$

$r_{inv} = 0.4 \rightarrow [1500, 1600, 1700, 1800, 1910, 2053, 2238, 2477, 2787, 3187, 3704, 4374, 5240, 6361]$

$r_{inv} = 0.6 \rightarrow [1500, 1600, 1700, 1800, 1919, 2087, 2321, 2650, 3110, 3755, 4659, 5925, 7698]$

$r_{inv} = 0.8 \rightarrow [1500, 1600, 1700, 1800, 1927, 2117, 2400, 2823, 3455, 4400, 5811, 7918]$

Figure D.3:  $m_T$  bins based on the signal mass resolution and the minimum 100 GeV width requirement, for each  $R_{inv}$  signal category.

2529

2530        In order to have a final  $m_T$  binning that is not highly model-dependent, we consolidate these  
2531        four different bins into a single binning which is provided below:

2532        **[1500, 1600, 1700, 1800, 1900, 2025, 2175, 2350, 2575, 2825, 3125, 3500, 3925, 4450, 5075,  
2533        6000]**